TOOL WEAR MECHANISM OF DIFFICULT-TO-CUT MATERIALS

By

Dinh Son Nguyen

A DISSERTATION

Submitted to
Michigan State University
in partial fulfillment of the requirements
for the degree of

Mechanical Engineering – Doctor of Philosophy

2020

ABSTRACT

TOOL WEAR MECHANISM OF DIFFICULT-TO-CUT MATERIALS

By

Dinh Son Nguyen

Titanium alloys (Ti), Cast Graphite Iron (CGI), Carbon Fiber Reinforced Plastics (CFRP) and CFRP/Ti Stack are difficult-to-cuts materials which have been extensively used and attracted attention in aerospace, automobile, chemistry, biomedicine, sport and other industrials. These materials have distinguished properties, i.e. Ti is a light-weight metal (4.3 g/cm^3 in density) which has a low thermal conductivity, 6.7 W/m.K (50.8 W/m.K for steel), CGI has superior physical and mechanical properties compared to gray cast iron which is commonly used in the automotive industry, CFRP and CFRP/Ti are light-weight materials with high corrosion resistance, and better mechanical properties. However, the common drawback of these materials is their poor machinability.

Firstly, with titanium alloy Ti64, the flank wear mechanism was investigated by examining the microstructural impact on flank wear attained. By machining four bars with distinct microstructures including elongated, mill-annealed, solution treated & annealed and fully-lamellar microstructures, the root causes of flank wear are determined to be the hard α-phase and the lamellar colonies. The hard α-phase are not supported by the surrounded phases whereas the lamellar structure offers constraints with its microstructures. For crater wear, it supposed that there are 2 main wear mechanisms happened at the same time, they are dissolution and diffusion. With Titanium machining, the diffusion rate is smaller dissolution, so diffusion mechanism is dominant in crater wear. Secondly, to investigate the cause of poor machinability of CGI, the straight turning experiments were performed with both FGI and CGI with various cBN inserts in dry condition at

high cutting speeds (mostly >400m/min). The poor machinability of CGI with cBN tool is explained by lack of Al2O3 formation layer in rake face when cut in high speed (600 and 800 m/min). The unusual phenomenon in flank wear improvement when cut CGI at high speed seems to be high cutting temperature generated less brittle CGI. Thirdly, with CFRP and CFRP/stack, the dominate wear mode in machining CFRP and CFRP/Ti stack are combination of flank wear and edge rounding and the main wear mechanism is the abrasive.

Finally, two methods to improve the machinability were applied in machining these difficult-to-cut materials: the super-hard ceramics coating tools and minimum quantity lubrication (MQL). The number of coating materials: BAM, AlTiN, ZrN, (AlCrSi/Ti)N and uncoated carbide are examined in drilling and turning processed with Ti64 and CFRP/Ti stack. The nanocomposite (AlCrSi/Ti)N with alternating layers show significant improvement. With the MQL method, the wear evaluation of dry, minimum quantity lubrication (MQL) and MQL with nanofluid in turning the most common titanium (Ti) alloy, Ti-6Al-4V, in a solution treated and aged (STA) microstructure are investigated. In particular, the nanofluid evaluated here is vegetable (rapeseed) oil mixed with small concentrations of exfoliated graphite nanoplatelets (xGnP). This work focuses on turning process which imposes a challenging condition to apply oil droplets directly onto the tribological surfaces of a cutting tool due to the uninterrupted engagement between tool and work material. The preliminary experimental result shows that MQL and in particular MQL with the nanofluid improve the machinability of Ti alloys even for turning process. However, to attain the best performance, the MQL conditions such as nozzle orientation and the concentration of xGnP must be optimized.

This dissertation is dedicated to:
my father, Chinh V.Nguyen, my mother, Chinh T.Nguyen; my brother, Thai V.Nguyen;
my wife, Diep Tran; my children, Nam Nguyen, Chi Nguyen and Ha Nguyen.
Thank you for always believing in me.

ACKNOWLEDGEMENTS

I would like to gratefully and sincerely thanks my advisor Professor Patrick Kwon for his support, patience, and excellent guidance throughout my PhD study.

I would also like to thank Professor Thomas Bieler, Professor Brian Feeny and Professor Yang Gou who served as my committee members, giving me many insightful comments and suggestions that improved the contents of this dissertation. I want to thank Professor Dave Kim at Washington State University for allowing me to work with his team and for his guidance in publishing paperwork.

My appreciation especially goes to Professor Thomas Bieler for providing equipment for my experiment and his guidance in data analysis. Also, I would like to thank him and his student, Di Kang, for helping me to perform the EBSD experiments. My sincere thanks also goes to Professor Yang Gou for allowing me to work with his team and using his equipment.

I would like to thanks to Mr.Lars Hauhold at Fraunhofer CCL, USA for his generous help in doing experiments and making equipment available for my use. I want to thank to thank Brian Hoefler at Sandvik Coromant, Mr. Rich Maton at Sumitomo Electric Carbide for providing tools for experiments and Mr.Craig Gunn for editing my paperwork.

I thank my lab mates: Trung Nguyen, Sirisak ToopTong, Do Truong, Tyler Bauder, Juan Sandoval, Ryan Khawarizmi, Amr Saleh, Jisheng Chen and Bibek Poudel for their guidance and assistance with the experiments in my years of my PhD program.

Lastly, I wish to thanks my parents, Chinh V.Nguyen and Chinh T.Nguyen; my brother, Thai V.Nguyen; my wife, Diep Tran; and my three little children Nam, Chi and Ha for supporting and inspiring me.

TABLE OF CONTENTS

LIST OF TABLES

LIST OF FIGURES

CHAPTER 1: DIFFICULT-TO-CUT MATERIALS

1. Titanium Alloys[†]

Titanium (Ti) and its alloys are extensively used because of their high strength-to-weight ratio, high operating temperature, and fracture and corrosion resistance. Ti alloys are considered light metal alloys along with aluminum (Al) and magnesium (Mg) with its density at 4.3 g/cm^3[1, 2], which is higher than Al and Mg but only about 60% of the density of steel (7.83 g/cm^3). Ti alloys have tensile strengths equivalent to ferrous alloys [3, 1]. Another advantage of Ti alloys are their capability to withstand high temperatures. For example, the parts made of aluminum alloys can operate up about 130°C [5, 6] compared to Ti alloys which can operate well above 300°C [4]. Some commercial alloys can work well under operating temperature as high as 595°C [3, 4]. Because of these excellent characteristics, Ti alloys are essential in medical, food and chemical applications [5, 6, 7]. Like other metallic alloys, Ti alloys are castable, forgeable, and weldable with many conventional techniques. However, the high cost of Ti alloys, about four times of that of stainless steel, is the main obstacle to the use of Ti alloys in many other applications [3]. In addition, the machinability of Ti alloys is very poor in spite of the extensive research work since the 1960s. The most common Ti alloy, Ti-6Al-4V (open abbreviated as Ti64) has a low thermal conductivity of 6.7 W/m-K (compared to 50 W/m-K for 1045 steel). The hardness of Ti64 varies from 30-36 GPa [3, 8].

Ti alloys consist of two main crystal structures, hexagonal close packed (HCP or α) and body-centered cubic (BCC or β) structures. Their volume fraction and morphology depend on the

---

[†] This part was published at "Nguyen, D., Kang, D., Bieler, T., Park, K. and Kwon, P., 2017. Microstructural impact on flank wear during turning of various Ti-6Al-4V alloys. Wear, 384, pp.72-83".

alloying elements and heat treatment. The hexagonal α-phase has distinctive anisotropic mechanical properties. Ti alloys are classified into four groups, commercially pure (CP) alpha, near alpha, alpha-beta and metastable beta. CP Ti has excellent corrosion resistance, but it has a low strength and a limited working temperature only up to 300°C. Alpha and near-alpha alloys such as Ti-5Al-2.5Sn and Ti-8Al-1Mo-1V contain alpha-stabilizing elements (Al) with small amounts of beta-stabilizing elements (Mo, V), which enable them to operate up to 520°C. They have a good weldability but poor forgeability compared to alpha-beta alloys. Ti-6Al-4V (Ti64) is the most common Ti alloy and belongs to the alpha-beta group with 5.5-6.75% Al, and 3.5-4.5% V. With appropriate heat treatments, they are used in high-strength applications, and have application temperatures up to 400°C. Another common alpha-beta alloy is Ti-4Al-2Sn-4Mo-0.5Si. Meta-stable beta alloys have high fractions of beta stablizers present and have a high hardenbility and forgeability. [3, 6].

The microstructures of Ti alloys can be various combinations of α and β-phases, which can be formed by alloying with other elements and heat treatment. In addition to the α- and β-grains, the lamellar microconstitutent is very common, which can have a basket-weave structure with alternating layers of α and β phases [1, 9]. Ti64 can have various distinct microstructures, fully-equiaxed, mill-annealed, solution treated and aged (STA) or lamellar (also referred to as fully lamellar), can be obtained by adjusting the thermo-mechanical processing: [3, 10]. The STA microstructure can be obtained by the following process: homogenization above the β-transus of 1000^0C followed by hot deformation with a solution anneal at about 960^0C followed by a quench that precedes aging at 500^0C [11]. The heat process with mill-annealed condition is similar to the heat treatment process for STA but without recrystallization. The difference between fully equiaxed and STA microstructures is the recrystallization temperature or cooling rate [8]. To form

the fully lamellar microstructure, the heat treatment starts with homogenization above β-transus temperature followed by slow cooling. As the material gradually cools below the beta transus, the alpha phase nucleates in numerous parallel plates on particular planes in the beta phase, resulting in distinct but irregularly shaped colonies of the lamellar microstructure; each colony has the same alpha orientation and beta orientation. The lamellar spacing is larger with slower cooling rates. As colonies can nucleate on six different planes of the beta phase, multiple colonies nucleate in different parts of a prior beta grain with different lamellar orientations. Within a prior beta grain, several different colonies form that have different alpha orientations, which gives a basket weave appearance, but the remaining minority beta phase in each of these colonies has the same orientation.

The β transus temperature of Ti64 is about 950°C. Below this temperature, the combination of alpha phase (HCP) and beta phase (BCC) coexists while above this temperature the microstructure will turn completely into the beta phase. However, depending on the heat treatment (the quench temperature and cooling rate), the resulting microstructures and properties can be quite different, (1) full-equiaxed microstructure with good corrosion resistant and ductility, (2) mill-annealed microstructure with good ductility, (3) bimodal microstructure with equiaxed alpha and lamellar alpha + beta with higher strength and higher operating temperatures, and (4) fully lamellar microstructure with improved toughness as shown in Figure 1.1. [3, 8]

Ti alloys are known to have poor machinabilities due to several characteristics. For example, the low modulus of Ti alloys makes the machining process prone to instability. The low thermal conductivity elevates the temperature at the cutting zone. Dearnley et al. [13] estimated the cutting temperature on the rake face to reach 900°C when turning Ti64 at 75 m/min, 0.25 mm/rev in 10 seconds with cemented carbides tools. Because the cutting temperature is high with an extremely

small heat-affected zone, tool wear is very high, which concentrates around the cutting tip and chipping becomes prevalent [6]. Due to the high chemical reactivity of Ti, most available cutting tools form an adhesion layer that causes attrition wear on the tool.
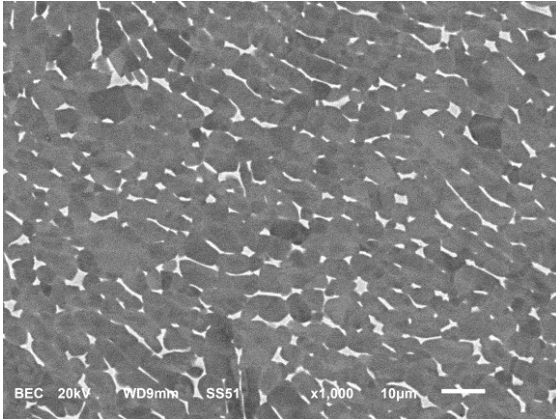
(a) Elongated (ELO)
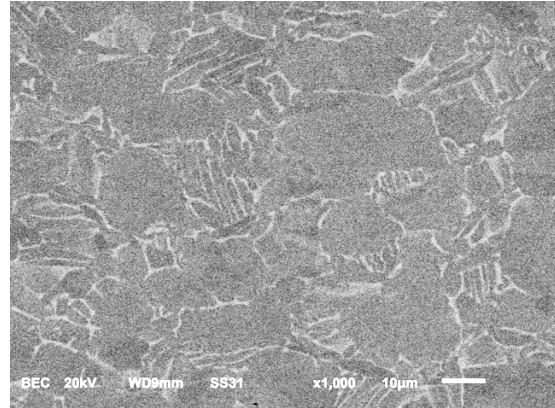
(b) Mill-Anneal (MIL)
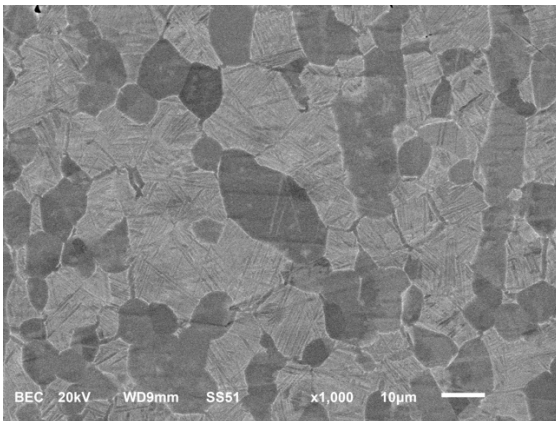
(c) Solution Treated & Aged (STA)
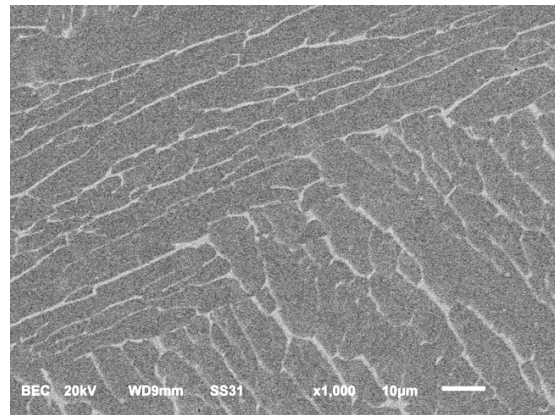
(d) Lamellar (LAM)

Figure 1.1. Microstructural images of four Ti64 grades [12].

Numerous works have reported the machinabilities of various Ti alloys with a wide range of microstructures. Arrazola et al. [14] carried out turning experiments up to the cutting speed of 100 m/min. to compare the machinabilities of Ti555.3 (solution-treated and aged (STA)) and Ti64 (quenched and annealed) with uncoated cemented carbide tools. The microstructure of Ti64 had 80% of alpha phase and 20% lamellar phase while Ti555.3 has 20% of alpha phase and 80%

lamellar phase. The flank wear results showed that the machinability of Ti555.3 was extremely poor compared to that of Ti64. Navneet et al. [15] conducted an orthogonal dry machining experiment where they measured the cutting temperature with an infrared camera on mill-annealed Ti64 and three Ti54M bars with three distinct microstructures, mill-annealed, STA and lamellar. The cutting temperature reached 1000°C when cutting at 80m/min. The cutting temperatures were reported to be similar among the bars while the cutting temperatures were found to be very sensitive to the feed rate. Armendia et al. [16] reported that the machinability of Ti54M was better than Ti64 when machining with uncoated carbide tools. Both work materials in the experiment had similar mechanical properties even though they had different heat treatment conditions. The Ti64 microstructure had coarse α-Ti laths with lamellar spacing of 20 microns whereas Ti54M had a finer microstructure with the average grain size of 10 microns. The Ti64 also had a higher fraction of equiaxed α-grains than Ti54M. They concluded that the machinability of Ti54M was approximately 10-15% better than Ti64 at their maximum cutting speeds (90 m/min for Ti54M and 80 m/min for Ti64). The cutting and feed forces were measured with a piezoelectric sensor, and both forces were about 100 N/mm^2 lower for Ti54M than those of Ti64. Kosaka et al. [17] have also studied the drilling machinability of three Ti alloys, Ti5Al4V-low Mo/Fe, Ti5Al4V-high Mo/Fe and Ti64 mill-annealed. Based on the microstructure images (and the Al content), the amount of primary α-phase in Ti64 was higher than the other two, and the size of primary α-grains of Ti5Al4V-high Mo/Fe was larger than Ti5Al4V-high Mo/Fe. The results showed that Ti64 was more difficult to machine than the other two. Comparing between Ti64 and Ti54M, Ti64 had more lamellar structure and poorer machinability than Ti54M.

Attanaiso et al. [18] studied Ti64 with four microstructures: full equiaxed, mill-annealed, bi-modal and fully lamellar by micro-milling with a cutting speed of 15.7 m/min and feed rate of 0.5

and 1.5 micron/tooth. The bi-modal has the highest hardness at 411± 15 Hv and the lamellar structure had the lowest micro-hardness at 356 ± 45 Hv whereas the hardness of lamellar structures measured with the nanoindentation is much smaller than equiaxed α grains. The cutting force was the lowest with the lamellar microstructure at feed rate of 1.5 micro/tooth. Gelfi et al. [19] reported the cutting forces when machining Ti64 with varying characteristics of the lamellar phase. The different lamellar structures were generated by heating up to 1020°C, 1050°C and 1080°C followed by either furnace or air cooling. The microstructure obtained by cooling in furnace is coarser in colony size and finer in lamellae width than cooling in air. The hardness was increased by cooling in air. However, the cutting force is lower with air cooling than the cutting force of furnace-cooled. The cutting force reduces significantly as the lamellar colony becomes coarser and the width of each lamella becomes finer. Dearnley et al. [13] carried out machining in commercially pure Ti64 with uncoated carbide tools at a cutting speed 60 m/min. With a feed rate of 0.35mm/rev and cutting time of 1 min, the maximum flank wear was 120 microns. Birmingham et al. [20] reported on flank wear of turning the lamellar Ti64 with carbide inserts at cutting speed of 125 m/min. The microstructure was lamellar with α-lath thickness of 5 micron and lamellar grain size of approximate 1 mm. The flank wear measured was about 600 microns with a feed rate of 0.15 mm/rev and a cutting time of 110 seconds.

Many works focused on measuring cutting temperature experimentally. Narutaki et al. [21] measured the cutting temperature using the thermocouple technique. The cutting temperature reached up to 727°C at 60 m/min and about 1077°C at 200 m/min when cutting Ti64 and Ti5Al2.5Sn with carbide tools. Kitagawa et al. [22] carried out milling and turning experiments with Inconel 718 and Ti6Al6V2Sn to measure the cutting temperature with the thermocouple mounted into the through-hole of the inserts. The cutting temperature when turning Ti6Al6V2Sn

($\alpha+\beta$ Ti alloy) at the cutting speed up 200 m/min with K-10 carbide inserts was 1050°C. Zoya et al. [23] studied $\alpha+\beta$ Ti alloys with 4.5%Al and 4.5%Mn with a lamellar microstructure. Turning experiments with cBN tools were conducted at the cutting speeds of 185, 220 and 280 m/min. The cutting temperatures measured with a non-contact-type IR pyrometer and were reported to range between 500°C and 1000°C depending on the cutting speed.

2. Cast Graphite Iron (CGI)[†]

Cast irons constitute 70% of the total material casted, of which flake graphite iron (FGI) or gray cast iron has been dominantly used by the automotive industry for engine blocks. In recent years, another family of cast iron, compacted graphite iron (CGI), has gained more attention as it has been adopted by many automotive companies. Implementation of CGI in a production line has risen as reported by SinterCast, Sweden, who supplies CGIs for the engine components of commercial and passenger vehicles throughout Europe, Asia and Americas. The rise in demand for CGI is due to its superior mechanical properties and strength-to-weight ratio. In addition, the tensile strength and fatigue strength of CGI are nearly doubled of those of FGI and the elastic modulus is about 35% higher than that of FGI [23].

Cast irons are classified into three categories based on the graphite morphology. FGI has randomly oriented flakes of graphite which can act as a stress riser as illustrated in Figure 1.2(a). While CGI has vermicular or 'cloud' graphite morphology which are randomly oriented but shorter and thicker with rounded edges as showed in Figure 1.2(b). The vermicular graphite adheres strongly to the iron matrix, which improve fracture toughness. Nodular graphite iron (NGI), whose

---

[†] This part was summitted at "Dinh Nguyen, Srisak Tooptong, Kyung-Hee Park, Patrick Kwon, 2019. Layer Formations when Turning FGI and CGI Bars and Their Impact in Machinability. International Manufacturing Science and Engineering Journal. American Society of Mechanical Engineers. (summited Oct 25th 2019, under reviewing)"

graphite has the form of nodules or spheroids in the iron matrix presented in Figure 1.2(c), promotes high mechanical and physical properties and exhibits the highest ductility among the three cast irons. The matrix of cast irons consists of ferrite and pearlite phases (the lamella structure of ferrite and cementite (Fe_3C) considered as a hard and abrasive phase). According to Dawson [24], the hardness and tensile strength of CGI is directly proportional to the pearlite content in the matrix structure.
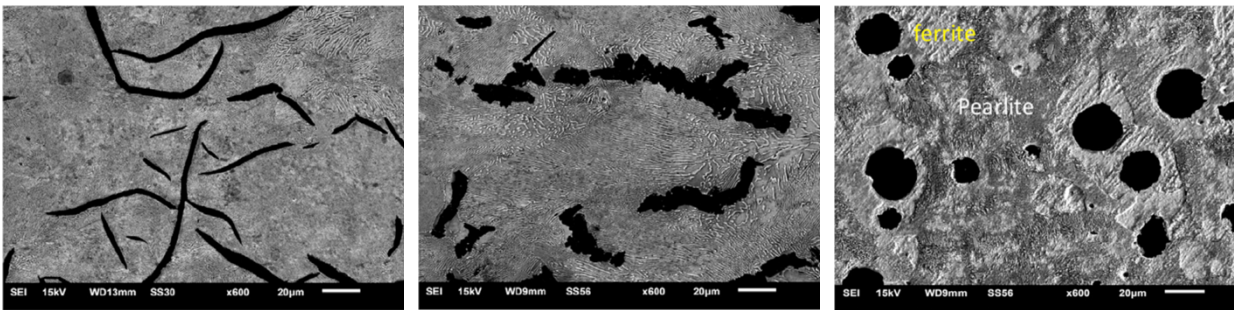
(a) FGI   (b) CGI   (c) NGI

Figure 1.2. The microstructures of FGI and CGI [25].

Basically, the machinability of a cast iron depends on many factors: the shape of graphite or 'nodularity,' the pearlite content and non-metallic inclusions such as oxides or sulfides in their microstructure [23, 24]. The three cast irons provide a whole spectrum of graphite shapes. This study focuses on the root cause for the poor machinability of CGI in comparison to FGI. In general, Souza et al. [26] claimed that FGI offers the best machinability following by CGI and NGI. The main difference in machinability between CGI and FGI is the difference in ductility. When cutting CGI and FGI, the cutting temperature is expected to be higher for CGI [27] as the work material and chip will undergo more plastic deformation to generate the chip compared to FGI [27]. In addition, manganese sulfides (MnS) inclusions present in the FGI microstructure is deposited onto the tool surface when cutting FGI. The presence of MnS layer has been identified as the primary

reason for the excellent machinability of FGI at high cutting speed [28]. It was claimed that MnS layer works not only as a barrier against diffusion and oxidation but also as a lubricant to reduce friction between cutting tool and FGI [28]. The CGI, however, does not have such inclusions, because magnesium (Mg) must be added to form the vermicular graphite. The small fraction of sulfur in CGI reacts more readily with Mg to form MgS in CGI instead of MnS [29].

Silva et al. [30] compared the machinabilities of CGI and FGI during high speed milling process and the result showed that flank wear was about 100% higher for CGI than FGI with the cutting speed of 600 m/min. Abele et al. [31] reported that the difference of the cutting tool life between CGI and FGI could be 10-20 times when the experiment was performed under high speed continuous cutting process. Nayyar et al. [32] conducted the machining experiments to study the effect of the microstructural variations on machinability in terms of tool life and cutting forces. Various kinds of CGI with differences in microstructures and FGI were machined with coated carbide tools at the cutting speed of 300 m/min both in dry and wet conditions. The results showed that the tool life when turning FGI was almost 17 times than that of CGI. Gastel et al. [28] claimed that the absence of MnS layer when boring CGI with cBN tools at the cutting speeds over 400 m/min resulting in a substantially shorter tool life compared to FGI. Tasdelen et al. [27] conducted milling experiments with carbide and cBN tools and concluded that FGI had a better machinability compared to CGI with both tools. When milling CGI with cBN inserts at the cutting speed of 700 m/min, high diffusion wear occurred leading to a significantly shorter tool life compared to milling FGI at the cutting speed of 900 m/min. The MnS layer did not form during CGI milling but a thin layer of MnS adhered on the cBN insert when milling FGI. Mocellin et al. [33] conducted drilling tests using uncoated and TiAlN coated carbide drills on CGIs with various nodularities and pearlite contents using FGI as a reference material. The CGI with high pearlite content had low

machinability and CGI 450 grade with 84% pearlite has a reasonable machinability compared to FGI. Heck et al. [34] improved the productivity in straight turning of CGI by cutting at a high cutting speed, using a multi tooling concept with interrupted cut or machining with low cutting speed and high feed rate. In a high production environment, however, machining under high cutting speeds is recommended. The cutting tool capable of cutting such materials are needed. Polycrystalline cubic boron nitride (pcBN or cBN) is the ultra-hard materials with its superior hardness, second to polycrystalline diamond (PCD) [35]. However, cBN is the best choice in machining FGIs at high cutting speeds because PCD is thermodynamically unstable against iron.

The cutting temperature plays a major role in tool life, tool wear and surface quality. In high cutting speed operation, the work material experiences high plastic deformation, high strain rate leading to the high cutting temperature on the cutting tool. Many research efforts have been made to study the temperature and its distribution on the tool surface. Malakizadi et al. [36] reported that the cutting temperature of FGI turning with cBN tool at the cutting speed of 480 m/min reached 900°C based on the result from finite element simulation using the Deform 3D program. Souza et al. [26] measured the cutting temperature with an infrared pyrometer to be around 700 °C when turning FGI at the cutting speed of 450 m/min. Fiorini et al. [37] reported that the cutting temperature of 800 °C was possible when turning FGI at 250m/min with cBN tool. Ming et al. [38] conducted the CGI milling at the cutting speed of 400 m/min and claimed that the cutting temperature was predicted to be about 700 °C using FEM simulation, while Ljustina et al. [39] reported the cutting temperature to be above 1000 °C when turning CGI at the cutting speed of 350 m/min and measured the cutting temperature with an infrared camera along with FEM simulation. Obviously, the increase in the cutting speed leads to the increase in cutting temperature [26, 40-44].

The cBN inserts can be obtained by either sintering individual cBN crystals together or bonding with ceramic and/or a metallic binder phase made with the catalysts or in solvents [45]. The cBN tools are typically characterized by the gain size, the cBN content and the type of binder phase. Harris et al. [46] showed that the cBN tools with the same binder material that have the smaller gain size has higher hardness compared to the larger gain size and content. Despite of their superior mechanical strength, the wear mechanism is the important study to find the optimal cutting tool for a given work material and achieve the better machining process. The fundamental wear mechanisms proposed for gradual tool wear are abrasion, adhesion, dissolution, diffusion and chemical reaction [47]. A combination of these wear mechanisms is involved during the machining process. Crater and flank wear are the most notable wear modes in metal cutting where the abrasion dominate on the flank face and the combination of abrasion and dissolution/diffusion dominate on the rake face as reported by Wong et al. [48]. The tool life of cBN tool is mainly limited by flank wear and edge chipping [49]. Konig et al. [50] reported that the predominant wear pattern of a cBN tool in machining of hardened FGI is microchipping. Hodgson and Trendler [51] indicated wear notching on turning high-speed steel M2 with a sharp edge cBN tool. In the turning experiments with AISI 52100 steel, the interactions between the binder phase in cBN tools and the workmaterial produce highly adherent layers. The failure at the interface between cBN grains and the binder led to pluck out of cBN gains [52]. Suh [53] mentioned that the diffusion/dissolution mechanism occurs when turning steel with cBN tool. Kramer [54] concluded that machining superalloys with cBN tools at high cutting speed raises the cutting temperature beyond 1200 ºC where the chemical stability and the diffusivity control the wear rate. Bhaumik et al. [55] concluded that the wear patterns on cBN tool are crater wear, flank wear, notching, microchipping and dissolution/diffusion wear at high cutting temperature.

The impact of oxidation (chemical reaction) is rarely reported in the literature. As shown by Liu et al. [56], the oxidation existed during the rubbing test of FGI and CGI. Tennehouse and Runkel [57] conducted turning experiments of FGI with carbide tools and reported that the reduction of O_2 content results in the less notch wear on cemented carbide tools. The oxidation is only active in high speed machining of alloyed steel with cBN tools. Flank wear was more intense when machining in argon compared to air. The formation of Al_2O_3 and TiN were found on the rake face of cBN insert when turning Alloy 718 due to the presence of Al and Ti in Alloy 718 which can give rise to the mechanically and chemically stable of Al_2O_3 [58]. Rowe and Smart [59] reported that the presence of oxygen led to the oxidation on the rake surface and prevented the insert from the adhesion of workmaterial and the build-up layer on the tool nose. Liu et al. [60] conducted milling of pearlitic FGI with cBN tools and reported that the FGI with an Al additive enhanced the machinability of cBN tools with the TiC binder. Al in the alloy forms the oxide film on the cutting tool and the presence of Al_2O_3 reduced the tool wear. Klimenko et al. [61] noticed a loose adhesion layer consisting of workmaterial and oxygen from the atmosphere mainly on the rake and flank faces.

3. Carbon Fiber Reinforce Plastics[†]

Carbon fiber reinforced plastic (CFRP) is known to have many positive characteristics such as high specific strength, excellent corrosion resistance, low thermal expansion, and low density. Due to these unique qualities, CFRP composites are becoming increasingly popular and their applications are reaching beyond the aerospace industry. Despite their many promising outlooks,

---

[†] This part was summitted at "Dinh Nguyen, Ryan Khawarizmi, Mohammad Sayem Bin Abdullah, Dave Kim, P. Kwon, 2019. The Effect of Fiber Orientation on Tool Wear in Edge-Trimming of Carbon Fiber Reinforced Plastics (CFRP) Laminates. Wear. (summited Oct 22nd 2019, under reviewing)"

CFRP composites have poor machinability due to the abrasive action by the reinforcing carbon fibers on the edge of the cutting tool when being machined [62, 63]. In the machining process, cutting tool must cut the carbon fibers effectively while minimizing surface, or subsurface, damage on the machined CFRP without causing extensive wear on the cutting tools.

Edge-trimming, commonly referred to as a planning or shaping process, is one of the most common machining processes for CFRP and has been studied extensively. Most of these studies have investigated the chip formation mechanisms in machining CFRP composites as a function of fiber orientation. Koplev [64] has carried out quick-stop edge-trimming experiments on CFRP for 0° and 90° ply angle laminates. The trimming process yielded distinct chips dependent on the fiber orientation; the 0° plies generated a continuous chip while the 90° plies produced a more irregular chip formation. Additionally, the quick-stop experiment showed that cutting 90° plies resulted in the notches along the fiber direction and a high number of broken fibers perpendicular to the cutting direction. In constrast, cutting the 0° plies created crack and delamination in front of the cutting edge.

Wang et al. [65] conducted edge-trimming experiments on unidirectional laminates in various fiber orientations to identify three dominating chip formation mechanisms. These include: (1) fracture along the fiber-matrix interface when cutting the laminate in the 0° orientation, (2) fracture perpendicular to the fiber axis when cutting laminates with a fiber orientation between 30° and 75°, and (3) the interlaminate shear fracture and fracture perpendicular to the fiber axis when cutting laminates with the fiber orientation of 90° and higher. Pwu et al. [66] conducted the planning process to cut unidirectional CFRP with 90° ply angle (or 90° plies). The fibers experienced considerable bending moments by the cutting force of the tool pushing on the fibers/matrix and eventually fracturing these fibers. Zhang et al. [67] machined unidirectional

13

CFRP with the ply angles of 0, 30, 60, 90, 120, and 150°. For the ply angles up to 90°, three deformation zones were identified as the chipping zone in generating chip, the pressing zone pressing down the CFRP below the cutting edge, and the bouncing zone reacting (bouncing) back to the flank surface. With the orientation greater than 90°, the deformation mechanisms were categorized into fiber bending, fiber-matrix debonding, and fiber buckling for carbon fibers.

Despite numerous works dealing with chip formation, the tool wear mechanisms when machining CFRP have not yet been fully established. It is now known that the wear mode when cutting CFRP differs greatly from the typical wear modes identified in cutting metallic alloys, flank and crater wear. Faraz et al. [68] defined cutting edge rounding (CER) as the main wear mode when machining CFRP. Maegawa et al. [69] studied the effect of fiber orientation by finding the relationship between tool wear and surface roughness by conducting down-milling experiments of 0°, 90°, and 0°/90° laminates at a cutting speed of 30 m/min, feed rate of 0.05 mm/rev, and depth of cut of 2 mm using uncoated carbide and polycrystalline diamond (PCD) tools. Various wear parameters were defined and one of these parameters defined as the tool-edge height was determined to correlate closely to the quality of surface finish. Heinrichs et al. [70] also studied tool wear by turning CFRP orthogonally to assess the influence of fiber orientation on tool wear and cutting forces. The CFRP with unidirectional fiber orientations of 0°, 30°, 60°, 90°, and 150° were cut with uncoated carbide inserts. The tools used to machine the ply angles of 30°, 60°, and 90° showed significantly more flank wear than any other orientation. This behavior is claimed to come from more intense spring-back on the laminates, particularly from the carbon fibers loading in the direction of the cutting force [67,71]

Edge-trimming and milling processes of CFRP have been investigated with various types of cutting tools and various machining conditions. Khairussima et al. [72–74] studied the tool wear

of carbide end mills in edge-trimming and milling of CFRP in the presence of coolant and dry cutting conditions to find the effects of these processes on surface roughness. Sheikh-Ahmad and Sridhar [75] carried out edge-trimming experiments on 45°/135° CFRP with uncoated and diamond coated carbide end-mills. At the low feed rate, the diamond coated end-mill is much better in terms of tool wear and surface finish. However, at high feed rates, the advantage of the diamond coating disappeared due to chipping and delamination. Janardhan et al. [76] studied the effects of various cutting conditions on unique tool wear and surface damage on the machined surface with the solid carbide diamond interlocking router tools in edge-trimming multidirectional CFRP. Han et al. [77] and Buse et al. [78] investigated deterioration of uncoated and titanium diboride (TiB2) coated carbide tools in machining multidirectional CFRP. They concluded that different orientations of carbon fibers may yield distinct flank wear due to the difference in chip formation mechanisms caused by these orientations. Inoue and Hagino [79, 80] studies the effect of helix angle and fiber orientation in end-milling of 0, 90, 45, 135° plies. Prakash et al. [81] also found the dependency of flank wear on fiber orientation, reporting that the greatest flank wear on the uncoated tool was found during the edge-trimming of 90° plies followed by 45° and 0° plies. Hosokawa et al. [82] reported the largest flank wear land in 45 and 90° plies, much more than 0 and -45°plies, in milling CFRP. On the other hand, Voss et al. [83, 84] claimed maximum wear occurring in 30° and 60° during orthogonal turning of 0, 30, 60, 90, 120, and 150° plies as these CFRP samples required higher cutting force upon investigation.

As evident from preliminary research, many works have focused on chip formation and some have indicated the impact of chip formations and fiber orientation on tool wear. To the authors' best knowledge, there has yet to be a major study focusing on the impact of fiber orientation and its corresponding wear mechanisms during edge-trimming. In addition, despite of the distinct wear

mode of edge rounding for CFRP, flank wear has been used to quantitatively describe the extent of tool wear when cutting CFRP. This study is mainly motivated by the need for the fundamental tool wear mechanisms with respect to the fiber orientation by conducting edge-trimming experiments of CFRP using micro-grain tungsten carbide endmills. Moreover, the quality of the machined CFRP surface is studied to correlate the distinct tool wear mechanisms on each fiber orientation or ply.

4. CFRP/Ti stack[†]

The carbon fiber reinforced plastics (CFRP) composite/titanium alloy (Ti) stacks have been popularized mainly by the aerospace industry as they typically show better mechanical performance than their homogenous counterparts such as titanium and aluminum alloys. Among the numerous machining processes, the most frequent and important process for the stack materials is drilling before the aircraft final assembly. In particular, the one-shot drilling method where various materials in the stack are drilled simultaneously with the same tool has received much attention due to the reduced workload, the simplified tooling infrastructure, and the better alignments for assembly. However, drilling CFRP/Ti stacks by a one-shot method is very challenging due to the extremely distinct machinability of each constituent layer. The method is especially susceptible to excessive tool wear and poor hole quality [85-89].

One common consideration for choosing a drill tool for the stack is to select a tool material suitable for drilling at least one constituent material layer. An issue, however, is that one tool material usually only performs well for one material layer of the stack but not for the other. For

---

[†] This part was published at "Dinh Nguyen, Vadim Voznyuk, Mohammad Sayem Bin Abdullah, Dave Kim, Patrick Kwon, 2018. Tool wear of superhard ceramic coated tools in drilling of CFRP/Ti stacks., 2018, Proceedings of the 2019 ASME Manufacturing Science and Engineering Conference."

example, diamond-coated drills, despite performing extremely well for CFRP, do not work at all for the CFRP/Ti stack material system because of the extremely poor performance of diamond-coated drills when drilling Ti layer [88, 90-92]. This is mainly due to the distinct mechanical properties and machinabilities. In addition, because of the distinct machining conditions of the two materials, it is expected each material layer must be cut in its distinct machining parameters. Because of these juxtaposed mechanical characteristics, CFRP [93-97] and Ti [98-101] have been extensively studied to understand the machinability of each material over the past decade. Besides, the development of superhard ceramic coatings, defined by hardness values ranging from 40 to 80 GPa, has received much attention in the last two decades for their high oxidation resistance, high thermal conductivity, and chemical stability [102]. Therefore, superhard-coated tools have been applied to the machining process of carbon fiber reinforced plastics (CFRP) composite/titanium alloy (Ti) stacks [103-106].

Chip formation in CFRP drilling is mainly due to the fracture of fibers, which results in a substantially lower cutting force and minimal heat generation compared to metal machining. From a tool wear perspective, only the abrasion action when cutting carbon fibers is critical and neither edge chipping nor temperature-driven diffusion/dissolution wear is relevant in cutting the CFRP layer. Additionally, the stagnation zone ahead of the cutting edge prevalent in metal machining does not occur, which is known to protect the cutting edge. Therefore, the cutting edge is venerable to the abrasive action in machining CFRP. These differences cause rapid blunting of the cutting edge, known as 'edge rounding wear' [94, 95]. Diamond based tools such as diamond-coated and polycrystalline diamond (PCD) tools have shown a significant reduction in edge rounding wear [90, 107]. While promising, the major disadvantage with these tool materials is the high cost which is prohibitive to many manufacturers [108-110]. A cost-effective tool material for CFRP

machining is still of critical concern for the industry. Ti presents itself as one of the most difficult-to-machine metals because Ti has low thermal conductivity [101], and is the strong affinities to all tool materials. These causes the tool wear issues like: extensive tool wear, tool failure [111-112] and adhesion (or attrition) wear [99].

The chip formation process is very complicated in drilling Ti. Also, ample coolant is necessary because of the high cutting temperatures in drilling. The tool life in Ti drilling under moderated speed has been shown to be limited by severe chipping and premature failure. Many attempts have been made to increase the tool life in Ti drilling [113]. Li et al. [114] compared the tool life in Ti drilling with and without a supply of cutting fluid using drills with through-coolant holes. The resulting tool life was 10 times greater compared to dry drilling. That shows that supplying cutting fluid is important for achieving suitable tool life for drilling Ti. Sharif and Rahim [99] studied the Ti drilling with uncoated and TiAlN-coated carbide drills at different cutting speeds and with a supply of water-soluble coolant. The uncoated carbide drills catastrophically failed after only a few holes while the TiAlN-coated carbide drill had managed 25 holes at the lowest cutting speeds (25m/min). This improvement comes from the TiAlN-coating, which substantially reduces Ti adhesion. Therefore, the coating could protect the tool from chipping or premature tool failure until the coating gradually wears off. Okamura et al. [115] studied vibration assisted drilling of Ti, which was shown to reduce chipping and the wear rate compared to conventional drilling. The researchers suggested that a reduction in drilling temperature from the applied vibrations resulted in better tool performance. Pecat & Brinksmeier further applied the vibration-assisted drilling approach to CFRP/Ti stack systems [116]. Despite the extensive research works in the past, the tool life for drilling Ti has not been improved significantly. The coated tools have not made any significant improvement in the machinability of Ti alloys [117].

Drilling the CFRP/Ti stack is typified by rapid tool wear with disparate wear mechanisms by each material layer. Therefore, an ideal tool must perform reasonably well at feasible conditions in the performance spectrum for both materials, which significantly limits the range of the available tool materials applicable to the stack. Therefore, major improvements need to be made to improve the wear resistance. At present, many studies have been conducted on the stack drilling and mainly focus on searching for the best combination of cutting tool substrate and superhard coating for a specific combination of stack materials [92, 103-106]. However, no single coating has risen to the top for the machining application for stack materials due to the deficiency in our fundamental understanding of the interactions between the cutting tool and stack materials.

CHAPTER 2: TOOL WEAR OF TITANIUM ALLOYS WITH VARIOUS MICROSTRUCTURE[†]

1. Work materials and microstructures

The microstructures attainable with Ti64 can range from mostly alpha phase to completely lamellar phase (thin beta lamellae between laths of alpha in colonies with the same crystal orientations making a basket-weave like pattern). This chapter assesses the effect of each phase and its size, shape and spatial arrangement on machining of Ti alloys. From this work, rationale for recommending the optimal microstructure to attain the best machinability in Ti64 (as well as other Ti alloys containing these two phases) will be proposed, so that expensive machining experiments are not required for each microstructure of each Ti alloy.

These two phases are identified to be the important factors in machining. Our previous work [12, 118] showed that the root cause of flank wear when turning the elongated (ELO) microstructure (Figure 2.1(a)) was identified as the hard orientation of the anisotropic α-crystals or cluster (as a group of neighboring α-crystals in a similar orientation denoted as 'hard alpha') which must be defined in relation to the cutting direction. However, as evident in Birmingham et al. [20], Ti64 with the fully lamellar phase had even poorer machinability. Thus, to understand the machinability of each kind of microstructures of Ti64 alloys; Elongated (ELO), Mill-anneal (MIL), Solution Treated and Aged (STA) and Lamellar (LAM), which provide a wide range of microstructures that vary the content and arrangement of the alpha and lamellar microstructural microconstitutents, were investigated to establish relationships between microstructure and

---

[†] This chapter was published at "Nguyen, D., Kang, D., Bieler, T., Park, K. and Kwon, P., 2017. Microstructural impact on flank wear during turning of various Ti-6Al-4V alloys. Wear, 384, pp.72-83."

machinability. The ELO microstructure results from unidirectional working of the equiaxed microstructure.
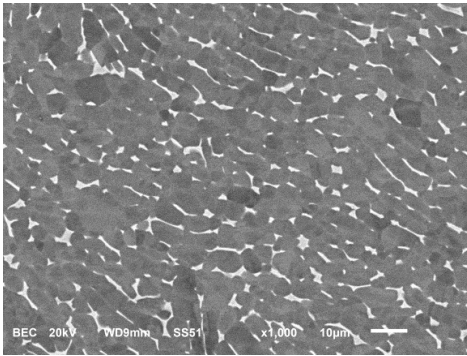
(a) Elongated (ELO)
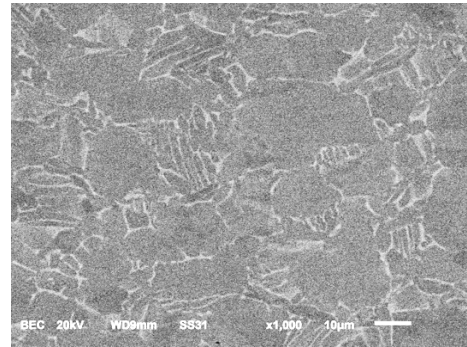
(b) Mill-Anneal (MIL)
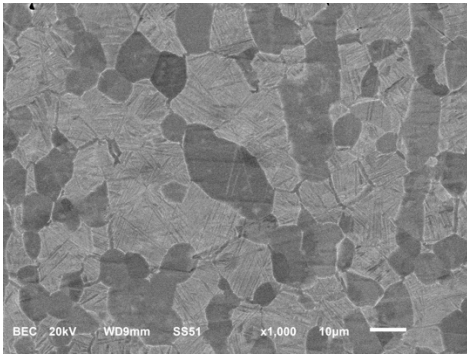
(c) Solution Treated & Aged (STA)
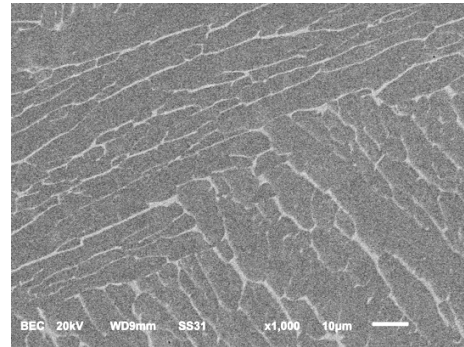
(d) Lamellar (LAM)

Figure 2.1. Microstructural images of Four Ti64 bars used in the machining study

The microstructure of each grade was examined with Scanning Electron Microscopy (SEM) as shown in Figure 2.1 (20 keV, 9 mm working distance, 1000x magnification in backscattered electron imaging mode using a Jeol 6610LV SEM). The backscattered electron yield at the detector is stronger from the beta phase, which appears as a lighter or white shade, which allows detection of the β-grains and the beta phase in lamellae and colonies. More importantly for the α-phases, the orientation of the α-grains was measured with Electron-Backscattered Diffraction (EBSD) scans with a MIRA SEM (Tescan, Orsay Holding, Kohoutovice, Czech Republic) with an Ametek (TSL)

orientation imaging microscopy system. EBSD scans were obtained on an area of 800x800 μm

with 2 μm step size to detect the crystal orientation of the α-grains.

(a) Cutout Sample

(b) α-crystal orientation affecting flank wear

(c) Molding with all three faces
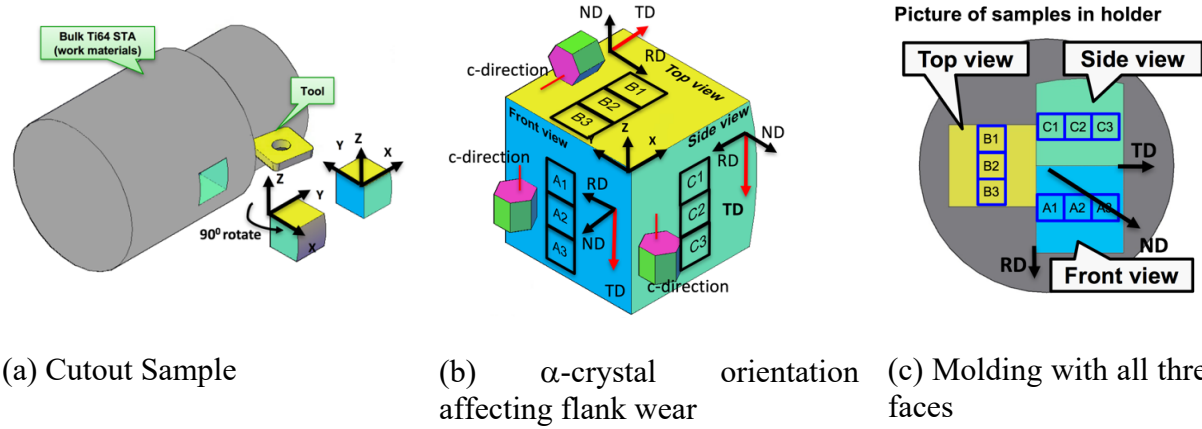
Figure 2.2. Microstructure images of Ti64 Bars

The crystal orientations were measured on the interior part of the bar as described in Figure

2.2 in order to avoid the microstructures affected by the surface of the rolling process and other

surface abnormalities. For each bar, the microstructures, both α-cluster and lamella colony

characteristics were identified and examined to estimate the arrangement and sizes of hard alpha

and lamellar colonies. Thus, before performing turning experiments, a piece of each bar was cut

out from the round bar as shown in Figure 2.2(a). Each sample was cut with wire electrical

discharge machine (EDM) to preserve their original microstructures and further polished to

remove any EDM surface artifacts. The microstructure on each face (Top, Front or Side) was

measured to identify the crystal orientations of α-grains and the size of the hard α-clusters as

shown in Figure 2.2(b). Because of the location of the cutout sample from each bar shown in Figure

2.2(a), the hard α-crystals on each face of the sample were defined as shown in Figure 2.2(b). To

optimize the preparation of the interior sample, the microstructures on all three faces were exposed

on the metallurgical mount as shown in Figure 2.2(c). Table 2.1 shows the average sizes of the α-

grains and lamellar colony sizes in each sample. The size of individual α-grain is smallest at 8.11µ in the ELO grade and largest at 15.3µ in the MIL sample.

Table 2.1. Average size for each constituent phase in four samples

Ti64	ELO	MILL	STA	LAM
Average Size of α-grains (µm)	8.11	15.3	10.2	-
Average size of lamellar colonies (µm)	-	22.0	19.7	743.1

2. Experiment procedure

2.1. Turning Experiments

Turning experiments were conducted with four Ti64 cylindrical bars whose overall dimensions are shown in Table 2.2. The straight turning process was carried out in a dry condition with Daewoo PUMA 300L CNC turning center (manufactured by Doosan Machine Tools, Seoul, South Korea). Each sample was turned at three distinct surface speeds of 61, 91 and 122 m/min. The depth of cut and feed rate were kept constant at 1.2 mm and 0.127 mm/rev, respectively [119, 120].
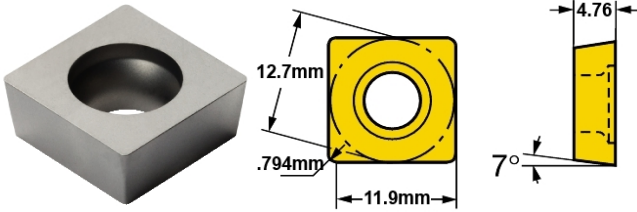
Table 2.2. Overall dimensions of Ti64 round bars

Sample	Diameter (cm)	Length (cm)
Elongated (ELO)	12.7	50.2
Mill-anneal (MIL)	12.7	35.6
Solution Treated & Annealed (STA)	12.7	64.8
Lamellar (LAM)	12.7	35.6

Uncoated carbide inserts, H13A grade with super fine grain size (the average grain size of 1 micron) and 6 weight % of cobalt, were supplied by Sandvik Coromant (Herbon, KY). The rake

and relief angles were 0º and 7º, respectively [121]. The geometry parameters are ANSI designation CNMA-432 without chip breaker and the thermal conductivity of the carbide is 65 W/m K, as shown in Table 2.3.

Table 2.3. Parameter summary for Uncoated carbide tool

Grade	H13A
Substrate	WC+6%Co
Thermal conductivity	65 W/m.K
Dimension	
Supplier	Sandvik Coromant

2.2. Flank wear measurement

After machining, 52% hydrofluoric acid (HF) was used to etch the adhesion layer deposited on the tools during cutting. The flank wear was measured using 3D laser scanning microscopy (VK-X100 manufactured by Keyence corporation, Osaka, Japan). The 3 dimensional (3D) geometry of the flank wear land was generated by capturing the reflection from the focal volume on the focal plane and the optical images. The turning process was interrupted after machining for a given time to retrieve the worn inserts and install a new insert before subsequent machining; hence flank wear was quantitatively determined as a function of time (or cutting length).

3. Results and Discussion

The α-grain in the microstructure is highly anisotropic, exhibiting strong anisotropic mechanical properties as Britton et al. [121] claimed the hardness and elastic modulus are substantially higher on the surface whose normal vector aligning with the c-direction of α-crystals (HCP) than any other surface. Specifically, it is about 20% higher in hardness (560 Hv compared to 459 Hv). The hardness as a function of the declination angle, defined by the deviation from the c-direction of HCP, does not change substantially between 0° and ±20° and, thus, the crystals with the declination angle of ±20° from the cutting direction are defined to be the hard alpha phase.
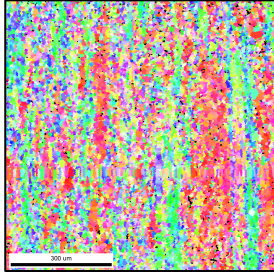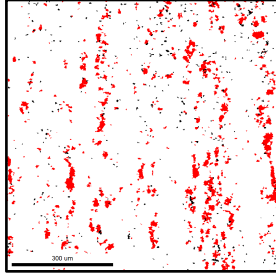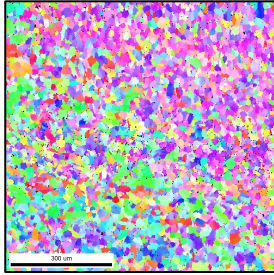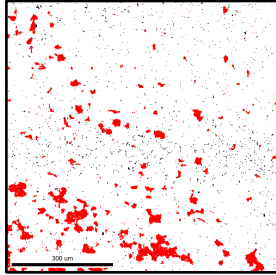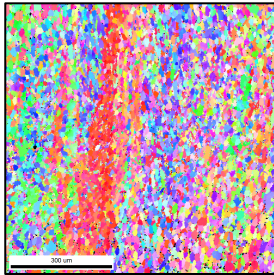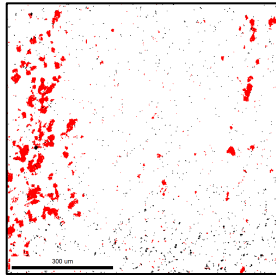
Grade	(a) OIM image	(b) Hard Alpha
ELO Front		
MIL Front		
STA Front		

Figure 2.3. Microstructural Orientation Analysis of ELO, MIL, STA and LAM Samples

The α-phase exists as individual crystals in a HCP crystalline structure while the lamellar microconstituent exists as colonies with alternating layers of thick alpha and thin beta phase. These crystals are randomly oriented throughout its microstructure. The orientation of each α-crystal in the microstructures was measured using the Orientation Imagine Microscopy™ (OIM). The OIM scans provide orientation maps of the α–grain orientations of three of the four Ti64 samples, ELO, STA and MIL samples. The LAM sample has very large α–colonies, such that no more than a few partial colonies are present in a similar sized OIM map. The images from OIM shown Figure 2.3(a) present partial crystal orientation information of of each grain, which is represented by different colors. The α-grains clearly exist as clusters where multiple neighboring grains have a similar crystal orientation. We hypothesize that flank wear is generated by the abrasive action by these 'hard' clusters [12, 118]. From the OIM images, the orientation and shape of hard clusters in relation to the cutting direction were extracted. For example, the red regions represent the α-clusters in the hard orientation in relation to the cutting direction. These hard regions are extracted from Figure 2.3(a) and presented in Figure 2.3(b). The average sizes of the hard clusters were analyzed using the Gauss filter [122] and the contours of hard clusters were generated for the ELO, MIL and STA samples on each of the three views (Side, Top and Side).

Table 2.4. Area Fraction of Each Phase Present in Each Grade

	ELO	MIL	STA	LAM
Alpha phase (SEM)	98.6%	99.2%	99.2%	99.6%
Hard Alpha	4.4%	3.83%	3.37%	0%
Beta phase (SEM)	1.4%	0.8%	0.8%	0.4%
Equiaxed alpha grains	98.6%	88.1%	42.9%	0%
Lamellar Colonies	0%	11.9%	57.1%	100%

Table 2.4 summarizes the area fractions of alpha and beta phases. Details of our estimation scheme will be presented in the next section. Both alpha and beta phases exist either as an individual phase or as parts of the lamellar microconstituent. The ELO sample does not have lamellar content while the LAM sample does not contain distinct alpha phase, despite the fact that all four samples have a similarly high content (around 99%) of alpha phase (this is an upper bound, as it is difficulty to capture the finest beta phase). All of the alpha phase resides as part of the lamellar constituent in the LAM sample while all of the beta phase resides as individual grains in the ELO sample. Only a small fraction of the alpha phase is hard and contributes to severe flank wear. Averages of the area fractions obtained from each face shown in Figure 2.2 are shown in Table 2.4.

Table 2.5. The Size of Hard α-Cluster

Ti64 grades		Average Hard α-Cluster Size (μm)			
		Min	Max	Ellipsoidal Approximation	
ELO	Top	95.98	188.2	Length	160.4
	Front	74.22	132.4	Width	79.0
	Side	83.68	100.7	Height	98.4
STA	Top	54.23	70.31	Length	85.7
	Front	61.75	77.76	Width	50.7
	Side	55.11	59.86	Height	59.5
MIL	Top	47.3	88.9	Length	74.0
	Front	63.49	82.49	Width	54.7
	Side	55.53	54.09	Height	60.8

Table 2.5 presents the estimated average size of hard alpha clusters on each of three faces for the ELO, STA, and MIL samples. Based on the microstructures on the three faces, the hard cluster size can be estimated in three directions representing length, width and height, which is presented as an ellipsoidal shape for α-clusters as shown in Figure 2.4. Please note that the ellipsoid does not represent the shape of hard entities which are traditionally perceived as the abrasives. It is the dimensional representation of the hard clusters with three characteristic dimensions, Length, Width and Height. The lamellar phase could not be represented as ellipsoidal shape as the microstructure of three faces could not be correlated. The LAM sample had the largest colony size of 743μm and the other two samples with lamellar colonies each had a similar lamellar colony size of around 20μm

(a) ELO   (b) MIL

(c) STA   (d) Ellipsoid Approximation
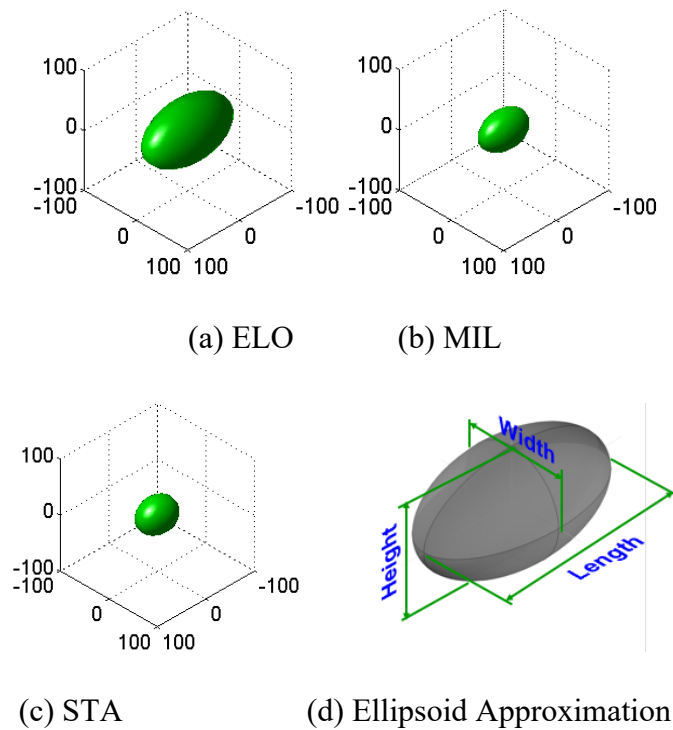
Figure 2.4. Average hard alpha cluster Approximated by an ellipsoid

3.1. Contents of Lamellar and Hard Alpha Phases in Each Sample
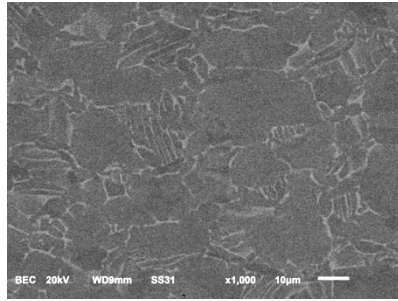
(a) SEM of the MIL sample
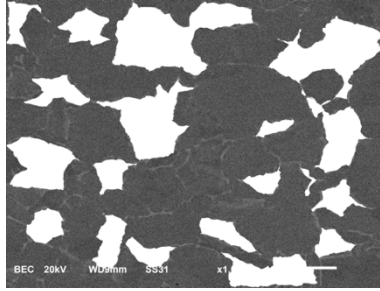
(b) Alpha Phase in MIL
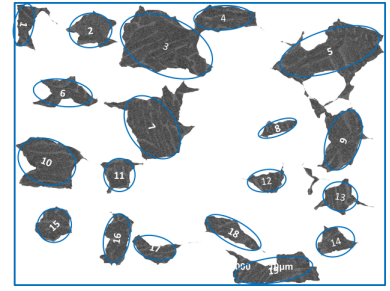
(c) Lamellar Phase in MIL
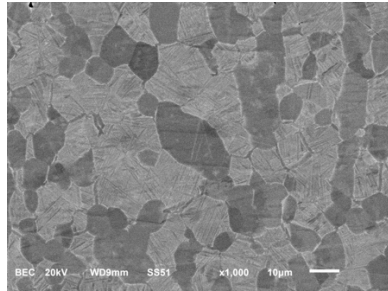
(c) SEM of the STA sample
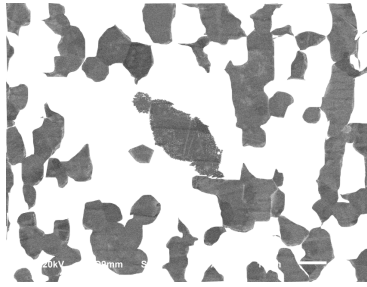
(d) Alpha Phase in STA
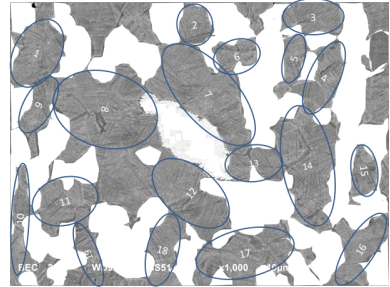
(e) Lamellar Phase in STA
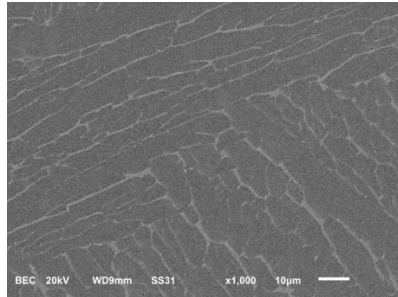
(f) SEM of the LAM sample
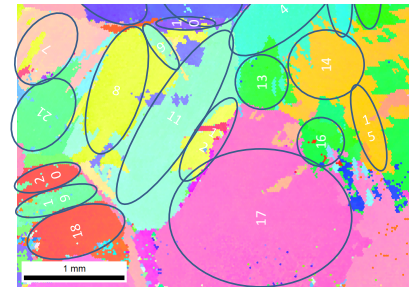
(g) Lamellar Phase of LAM

Figure 2.5. SEM Images and separation of α and lamellar phases in MIL and STA samples.

The BSE images were used to distinguish the lamellar regions from the α-phases. The α-phase is the uniformly dark phase while the β phases are bright, as shown in Figure 2.5(a and d) and Figure 2.1. Figure 2.5 shows the SEM images of the MIL and STA samples that contain 11.9% and 57.1%, lamellar structure, respectively. The lamellar content as well as alpha content is summarized for our four samples in Table 2.4. Some of the equiaxed alpha grains are in the hard orientation. The four samples have a wide range of lamellar content (between 0 and100%) but a

small range of the hard alpha phase (between 3.37 and 4.4%). The average lamellar size of MIL, STA and LAM samples was measured from SEM images as illustrated in Figure 2.5 and summarized in Table 2.1.

The microhardness was measured on each sample using a CM-800AT, Sun-Tec Microhardness testing system with the test load of 500 gf and 15 seccond of dwell time with 50x objective. The indentation matrix of 6 columns by 5 rows (total 30 indentations) was applied with the spacing of 250 microns at room temperature. Table 2.6 summarizes the hardness values of the four samples. Overall, the STA sample had the highest hardness at 331.9 Hv whereas LAM sample had the lowest hardness at 297.7 Hv. These values did not agree well with the hardness measured by Attanasio et al. [18] who reported substantially higher values. Their report indicated that the STA sample had the highest microhardness of 411 Hv whereas the LAM sample had the lowest value of 356 Hv. However, the hardness trends among the four samples are in agreement.

Table 2.6. Microhardness measured on Our Four Grades of Ti64

Ti64 grades	ELO	MIL	STA	LAM
Ave. hardness (HV)	320.4	308.0	331.9	297.7
Standard derivation	10.7	14.6	6.5	23.0

3.2. Flank wear

Among many machinability measurements such as the material removal rates, cycle time and tool wear, flank wear is the most commonly used method to quantify the machinability. Figure 2.6 presents the flank wear captured by 20x magnification after etching with HF solution after turning at each of the three cutting speeds, 61, 122 and 122m/min., with their respective cutting times. As the cutting speed increases, the flank wear increases for each sample. The main feature of flank wear in all four samples at the cutting speed of 61 m/min was that the scoring marks are not

pronounced until more than 330m were cut. The trends in flank wear at the low cutting speed were similar in all four samples of Ti64 as shown in Figure 2.6(a). The flank wear was slightly higher as the lamellar fraction increases. At the cutting speed of 91m/min, the scoring marks after cutting each sample show flank wear show clearly formed marks at the initial stages while the scoring marks are more apparent and wider in the later stages as shown in Figure 2.6(b). Based on the average flank wear, the flank wear increased considerably for all four samples compared to those from the low cutting speed. At the cutting speed of 122 m/min, the scoring marks were clearly formed at the beginning. The width of the scoring marks was much wider than those from the low and middle cutting speed. The flank wear increased significantly as the content of the lamellar phase increased, as evident with the STA and LAM samples. The flank wear of LAM increased substantially with cutting speed (note the different vertical scales in Figure 2.6).

3.3. The Scoring mark explanation

The correlation between the scoring marks and the hard -cluster size and/or the lamellar colonies depends on the sample. As presented in Figures 2.3 and 2.4 and Table 2.1, each sample has a characteristic size distributions of hard α-cluster and lamellar colonies, which correlate directly with flank wear. The hard α-clusters have dimensional characteristics represented by length, height and width as presented in Table 2.4. Based on the microstructures in our four samples and the cutting direction, the length of the hard α-clusters observable on the top and front views in Figure 2.2 should make the most dominant impact on the width of the scoring marks. The abrasive action will result in the scoring marks such that the width of scoring marks on the flank wear should be smaller or similar to the sizes of the hard cluster and/or the lamellar colonies of each sample. For example, the flank wear image after turning each sample is shown in Figure 2.7. With these images, the widths of the scoring marks are collected and analyzed for each sample.

The sizes of the hard alpha clusters for the three samples (except the lamellar sample) were measured, collected and analyzed from the OIM images shown in Figure 2.3 (a-c) while the average size of the lamellar colonies existing in the three samples (except for the elongated sample) was also measured from the SEM images shown in Figure 2.5(c) and (f).
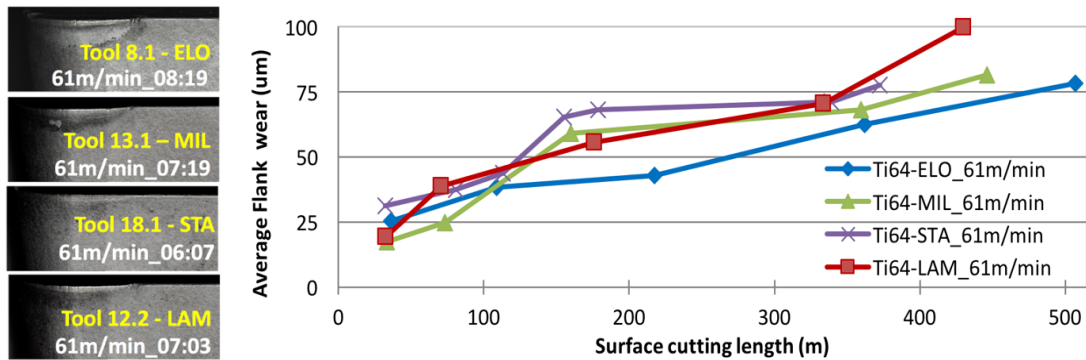
(a) Flank Wear after turning at 61 m/min.
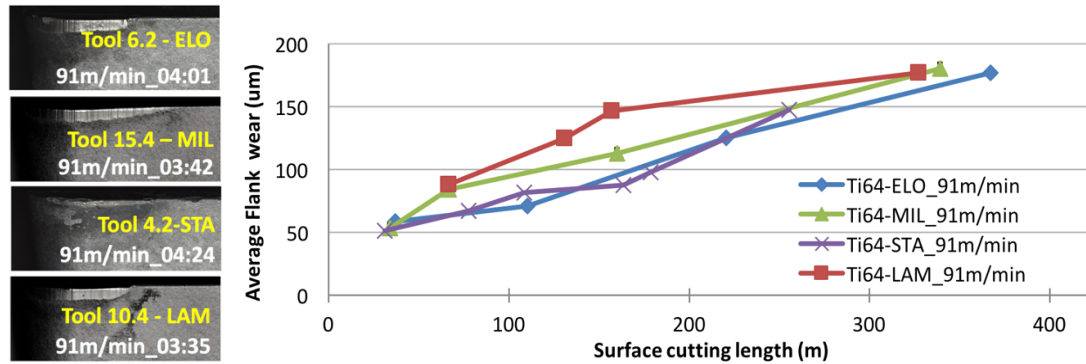
(b) Flank Wear after turning at 91 m/min.
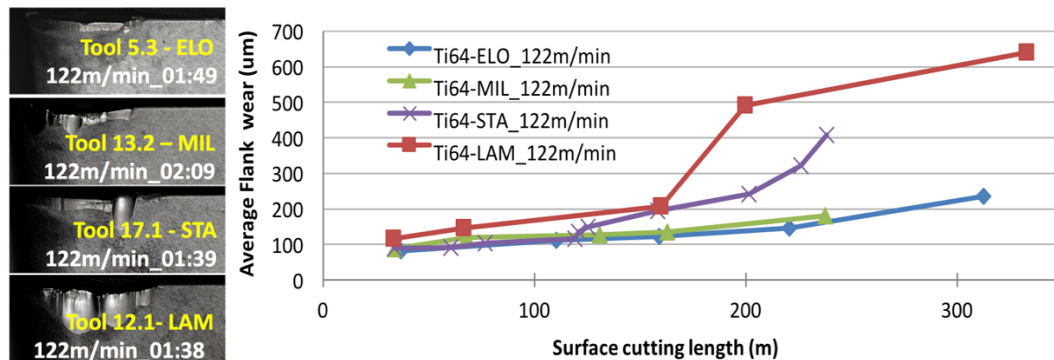
(c) Flank Wear after turning at 122 m/min.

Figure 2.6. Micrographs of Flank Wear Land and The Progress of Flank wear

32
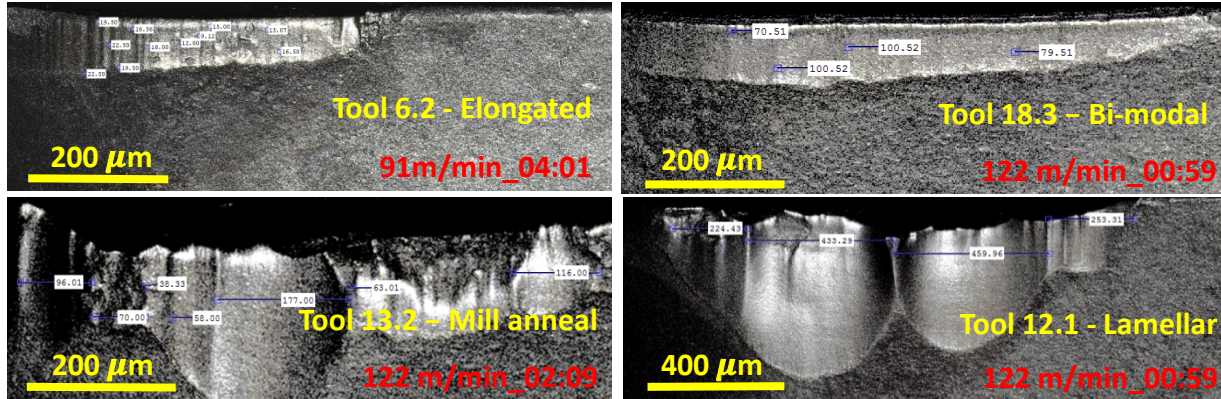
Figure 2.7. Measuring the width of each scoring mark on flank wear land after turning at the respective speed in four inserts

(a) The Width of Scoring Marks

(b) The Size of Hard α-clusters
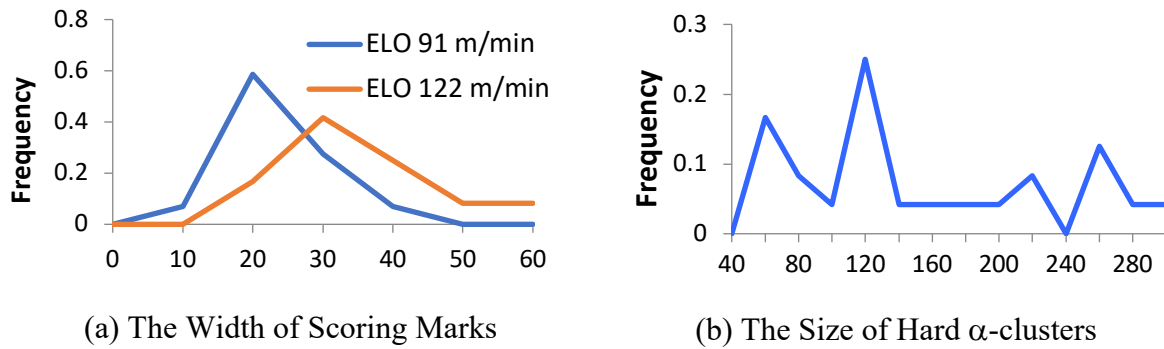
Figure 2.8. The histograms of scoring mark width and size of hard α-cluster of the ELO grade

Figures 2.8-11 illustrate the correlation between the scoring marks on the flank wear land and the characteristic sizes of two major microstructural entities, hard α-cluster and lamellar colony for each of the four samples. From the flank wear images, the width of each scoring mark on the flank wear land was recorded, collected and presented in the histograms. Figure 2.8(a) shows the histogram of the widths of the scoring marks on the flank wear lands resulting from cutting the ELO sample at 91 and 122 m/min. The scoring marks from 61m/min are not presented for any sample because the scoring marks were very narrow and shallow, and not clear enough to measure accurately. In addition, the scoring marks became wider as the cutting speed increased for all four samples, which is also related to the increase in the cutting force. The microstructure of the ELO

sample consists of (almost 99%) α-grains (see Table 2.4) of which only about 4.4% are the hard α-clusters causing flank wear. More than 50% of the scoring marks have a width of around 20 microns, which is similar to the size of the hard α-clusters that are mostly between 40 and 100 microns as shown in Figure 2.8. Appearently, without any other hard phases, the hard α-clusters are responsible for generating the scoring mark on the flank surface. There are some exceptionally large α-clusters around 200 microns which may have generated the scoring marks with the width as large as 50 microns at the cutting speed of 122m/min.
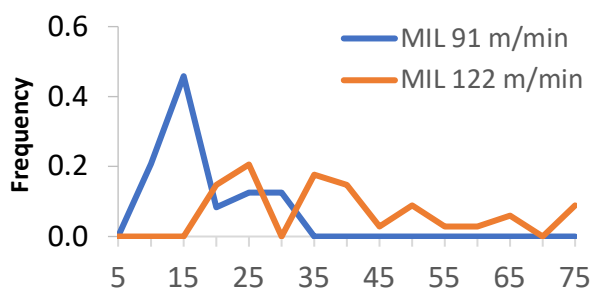
(a) The Width of Scoring Marks (μ)
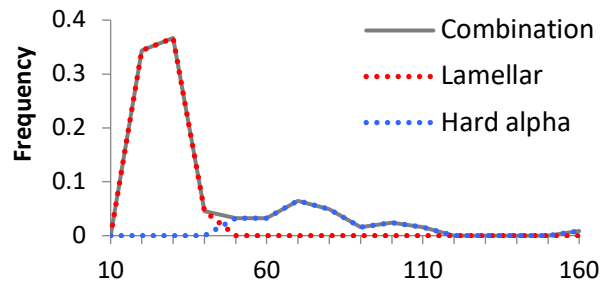
(b) The combination of hard α-clusters and lamellar colonies.

Figure 2.9. Histogram representations of the scoring mark, hard α-cluster and lamellar phases of the MIL grade
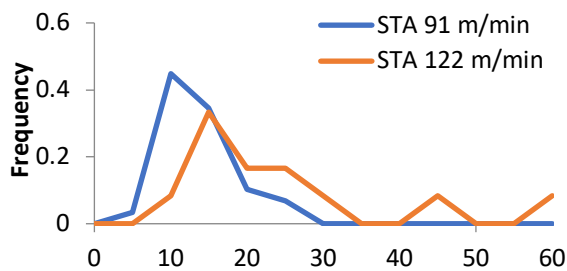
(a) The Width of Scoring Marks (μ)
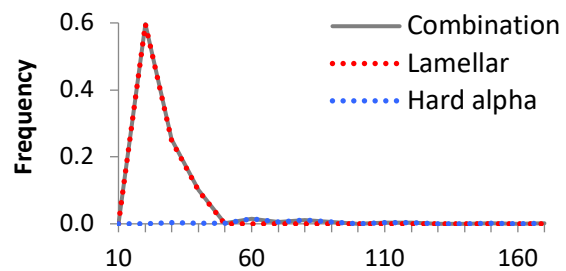
(b) The combination of hard α-clusters and lamellar structures.

Figure 2.10. Histogram representations of scoring mark width, hard α-cluster and lamellar colony sizes of the STA sample

For the MIL and STA samples, the scoring marks are also correlated with the abrasive actions by both the hard α-clusters and the lamellar colonies. As shown in Figure 2.9 (a), the scoring mark histogram shows a bimodal distribution in width at both cutting speeds contributed by the distinct size differential between lamellar colonies and hard α-clusters. The combined effect of the hard α-clusters (3.83%) whose average size ranges between 45 microns and 87 microns and the lamellar phase (11.9%) whose average size ranges between 20 and 40 microns, shown in Figure 2.10. For the STA sample, the scoring marks with about 10-15 microns at 91 m/min and about 20 microns at 122 m/min are correlated with the higher 57.1% lamellar fraction whose average sizes are about 20 microns, but 3.37% of the hard alpha clusters whose average size is approximately 60 microns, as shown in Figure 2.10. Because only 3.37% of the total phase is the hard α-cluster contributing to flank wear, the effect of hard α-cluster is minimal.

(a) Width of Scoring Marks   (b) Size of Lamellar Colonies
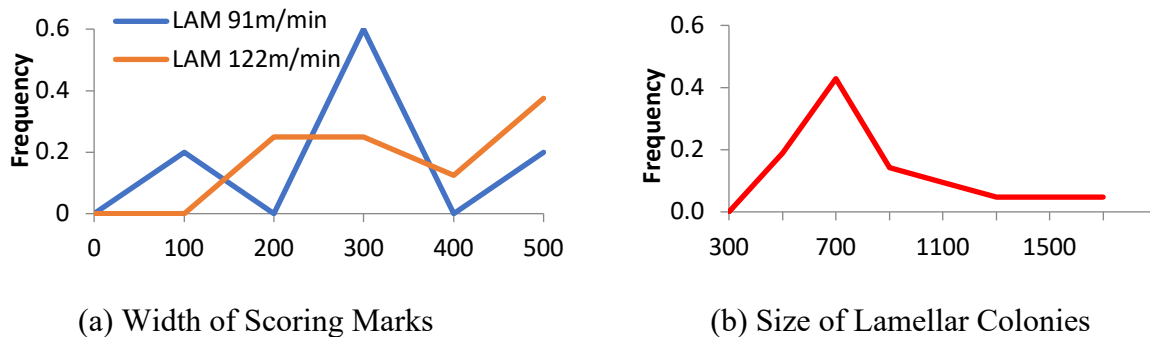
Figure 2.11. Histogram representations of scoring marks widths and lamellar colony sizes in the LAM grade

For the LAM sample, only the lamellar colonies can produce the scoring marks left on the flank surface. The lamellar colony size in the LAM sample is substantially larger than any other microstructural feature. The average of the lamellar colonies is estimated to be around 700 microns. The wide scoring marks whose average width was 300 microns (see Figure 2.7) were probably generated by these large lamellar colonies, shown in Figure 2.11. Table 2.7 presents the

summary of the width range of the scoring marks and the sizes of two main phases causing flank

wear and the correlation between the two is well documented throughout this study.

Table 2.7. Correlation between microstructural size and scoring mark.

Grades	Scoring mark width (micron)	Hard α-cluster size (micron)	Lamellar size (micron)
ELO	9.1 – 56	35 - 201	-
MIL	11.7 – 54	33 – 70.2	13.3 - 38
STA	5 – 55.5	17 - 105	12 - 31
LAM	96.1 – 433.3	-	363– 1601

3.4. Discussion on Flank Wear

Figure 2.12 represents the flank wear as a function of cutting speed for each sample. For the

ELO sample with only the hard α-clusters, flank wear increased modestly with cutting speed. With

11.9% of the lamellar content in the MIL samples, the flank wear was slightly higher than the ELO

sample. However, for the STA sample with 57.1% lamellar content, the flank wear behavior was

closer to the LAM sample which had the greatest amount of flank wear at the high cutting speed.

Flank wear at the low and medium cutting speeds (61 and 91m/min) slightly increased as the

lamellar content increases. However, flank wear was significantly increased at the high cutting

speed (122m/min) with the increase in the lamellar content. The content of the hard α-cluster

among three samples, ELO, MIL and STA, are similar at 4.4, 3.83 and 3.33%, respectively. Flank

wear can be converted to the flank wear rate by dividing by the cutting distance. Figure 2.13 shows

the relationships between flank wear rate and the lamellar content in terms of area fraction for four

samples. The important finding is that the effect of the hard α-clusters diminishes with increasing

cutting speed where as the effect of the lamellar colonies intensifies with the cutting speed.
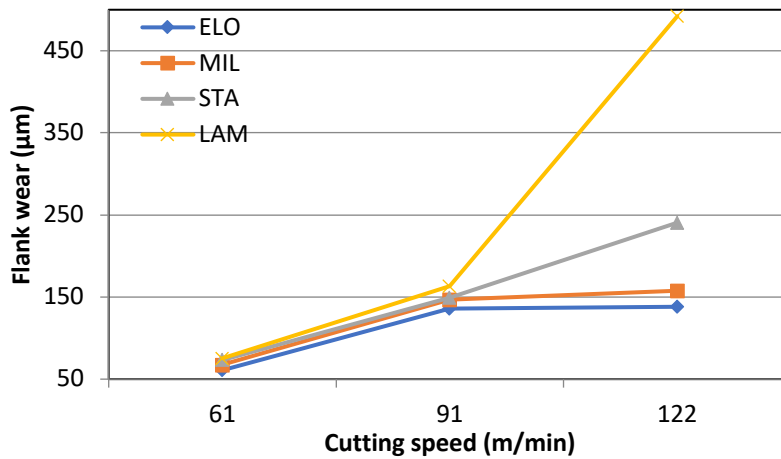
Figure 2.12. Flank Wear vs Cutting Speed
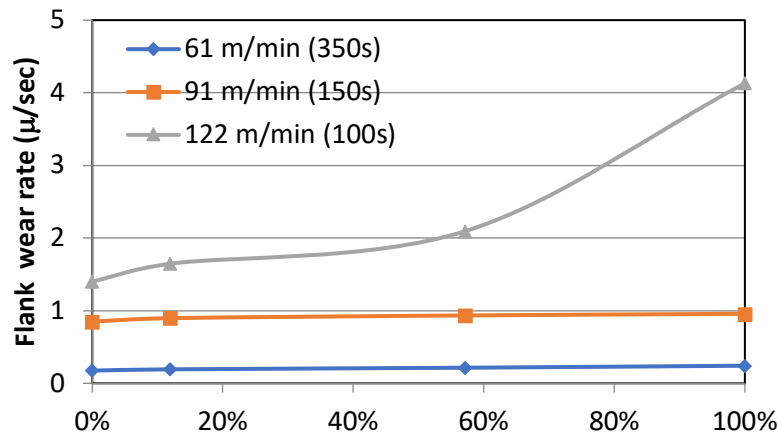
Figure 2.13. Flank wear rate vs Lamellar content

This can be explained by the microstructural difference between the α-clusters and the lamellar colonies. Kwon [123] and Wong et al. [118] reported the two distinct modes of flank wear depending on the constraint on the abrasive phases, 2-body and 3-body abrasion modes. These are two ideal extreme conditions representing practical abrasive conditions. In the 2-body abrasion mode, the 'hard' abrasive phases are constrained due to either the complex morphology or the relative large size while abrading the tool material. On the other hand, in 3-body abrasion mode,

the 'hard' abrasive phases are not constrained so that the relative motion (e.g.: roll) as third bodies exists between two tribologically interacting bodies. The two distinct modes directly impact how flank wear proliferates in machining. In 2-body abrasion, flank wear increases with the cutting speed while in 3-body abrasion flank wear decreases with cutting speed. The difference is demonstrated on Figure 2.14 where the flank wear is represented as a function of temperature (or cutting speed as in most cases the temperature will increase with the cutting speed). In machining Ti alloys, flank wear is expected to be that of 2-body abrasion but with slightly different ramification due to the difference in the microstructural difference between the hard α-clusters and the lamella colonies. The complex morphology of the lamellar colonies provides a high level of constraint during abrasive action, which is similar to the extreme case of the 3-body abrasion. The abrasion by the hard α-clusters surrounded by mostly other α-phases takes place as only 3-4%, in area fraction, are identified to be in the hard direction. The α-crystals surrounding the hard α-clusters do not provide a solid constraint for the hard α-clusters, which deviates from the strict condition of the 2-body abrasion. As the lamellar content increases gradually with MIL, STA and finally to LAM samples, the complex morphology constraint in the lamellar phase during machining especially at high cutting speeds, which make the abrasion to take place in the 2-body condition. Also the large size of colonies implies that a hard-oriented large colony could make a large gouge in the tool. Therefore, even though the lamellar phase is slightly softer than the α-phase as shown in Table 2.6, the lamella colonies were the more effectively abrasive.

The arguments made throughout this dissertation assume that the phase transformation occured at the flank face. On the crater surface, the temperature reached over 1000C even at 60m/min, which is high enough to transform the material to the beta phase. Also, high stress can also facilitate metastable transformation to the softer beta phase, which will revert to alpha when

the stress is removed, similar to what happens in dynamic transformation of austenite to ferrite (the softer phase) [124].
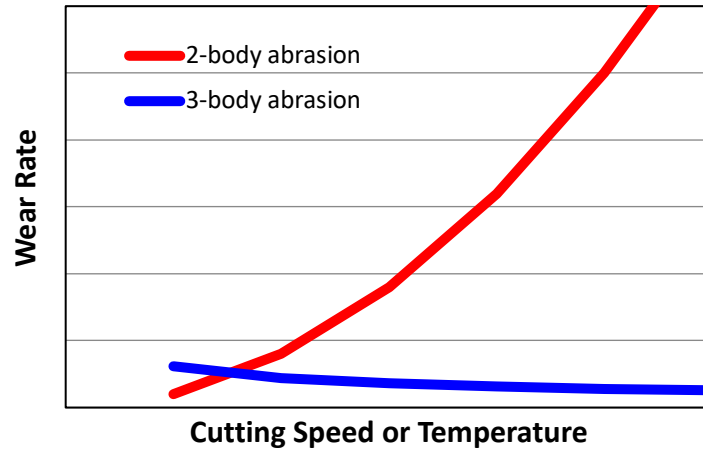
Figure 2.14. Difference in Wear Behavior with 2-body and 3-body Abrasion
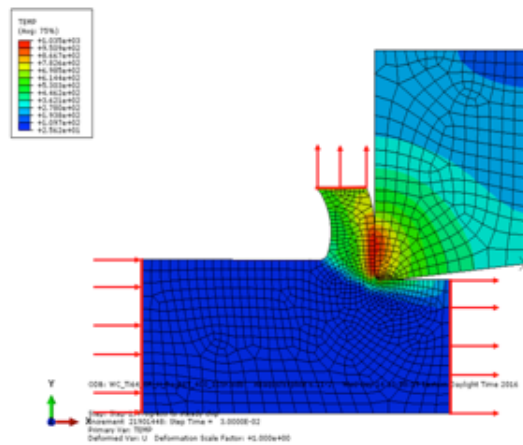
Figure 2.15. 2D schematical model and boundary conditions

To predict the cutting temperature at the flank surface, the Johnson-Cook (J-C) plasticity models has the following form.

$$Y = A\left(1 + \frac{B}{A}\varepsilon^n\right)\left(1 + C\ln\dot{\varepsilon}'\right)\left(1 - T^{''m}\right)$$

where Y is the flow stress, ε is the equivalent flow strain, $\dot{\varepsilon}$ is the non-dimensionalized strain rate and T' is the non-dimensionalized temperature, $T' = (T - T_r)/(T_m - T_r)$ with T_r and T_m are room temperature and melting temperature of Ti64, respectively. The parameters for the J-C models were obtained in the literature for the mill anealed and lamellar samples and shown in Table 2.8. The Arbitrary Lagrangian Eulerian boundaries were applied in Finited Element Analysis ABAQUS simulation and the element types for the explicit problems with thermal-diplacement elements [125]. The boudary conditions which the tools were fixed, the flow of work material move around the cutting edges were applied as can be seen in 2D-schematical (Figure 2.15). The friction coefficient of 0.6 between tungsten carbide tool and Ti64 work metrial was applied [126]. The ABQUS simulations were carried out to predict the flank temperature. The flank wear lands which were applied in the geometry models were 100 microns for mill anneal sample and 180 microns for lamellar sample. The temperature of the flank sides were generated by averaging the nodal temperatures on contact area between the tool and work materials through flank wear lands. The temperatures of elongated and bimodal were roughly estimated by interpolating from the temperature results of mill anneal and lamellar samples based on the phase contents. The flank temperature predicted by FEA simulation were shown in Table 2.9 for all four samples. Based on these results, the argument can be made that at least some transformation to beta phase is reasonable.

Table 2.8. Johnson-Cook plasticity models for the mill anneal and lamellar grades.

Grade	A (MPa)	B (MPa)	n	m	C	Ref
Mill anneal	782.7	498.4	0.28	1.0	0.028	Lee et al. [127]
Lamellar	831	858	0.302	0.72	0.015	Chen et al., [128]

Table 2.9. Flank Temperatures at each cutting speed on each grade

	ELO	MIL	STA	LAM
61m/min	520°C	545°C	620°C	780°C
91m/min	625°C	660°C	735°C	825°C
122m/min	715°C	765°C	795°C	830°C

4. Conclusion

Flank wear of four samples of Ti64 was examined. The root causes of the flank wear were determined to be the hard α-clusters and the lamellar colonies in their respective microstructures. The corresponding area fractions (or content) of the hard α-clusters and the lamellar colonies were obtained by examining the microstructures of four samples. The lamellar and alpha content and their respective sizes vary substantially among the four samples, and the relationship between flank wear and each of these features has been studied. At the low cutting speed (61m/min), the effect of 4% hard α-cluster and 100% lamellar phase are similar. As the cutting speed increased, the lamellar phase became the much more detrimental phase. At the high cutting speed (122m/min), the flank wear was about four times higher in the LAM sample compared to those from ELO and MIL samples. The differences in the flank wear behavior between the hard α-cluster and the lamellar content can be attributed to the microstructure constraints. The hard α-clusters are not supported by the surrounding phases while the complex alternating phases between alpha and beta offers constraints with its microstructures. This will support the tribological mechanism of 2-body abrasion that is consistent with the observed wear rates.

CHAPTER 3: LAYER FORMATION WHEN TURNING FGI AND CGI BARS AND THEIR IMPACT IN MACHINABILITY[†]

1. Work materials

The CGI tube provided by Sintercast AB (Katrineholm, Sweden) has a cylinder shape with outer and inner diameters of 145 mm and 98 mm, respectively, and the length of 204 mm and solid on one end to be mounted on the chuck. ISO 16112:2017 classifies CGI's to various grades by their tensile strength. The CGI (grade GJV-450) used in this study has the tensile strength of 450 MPa where its microstructure consists of vermicular graphite and fully pearlitic matrix. The FGI grade 2 obtained from Alro Steel Company (Lansing, MI, USA) has a solid cylinder with diameter of 152.4 mm and the length of 444.5 mm as presented in Table 3.1. According to ASTM 48, FGI grade G2 has a fully pearlitic microstructure except at the outer edges with some ferrite phase. The percentages of Mn and S in FGI is much higher than those of CGI while the amounts of other elements are extremely small as shown in Table 3.2. As stated, the main different between FGI and CGI in their microstructure is the morphologies of graphite phase. The graphite phase in CGI is quite different from that of FGI as SEM images with magnification of 500x as shown in Figure 3.1.

Figure 3.1. Microstructures of the FGI (left) and CGI (right) used in our experiment.

Table 3.1. Overall dimension of work materials

Work materials	Grade	Shape	Outside diameter (mm)	Inside diameter(mm)	Length (mm)	Supplier
FGI	G2	Solid bar	152.4	-	444.5	Alro Steel
CGI	GJV-450	Cylinder	145	98	204	Sintercast, Sweden

Table 3.2. Chemical element content of work materials

	%C	%Si	%Mn	%S	%Mg	%Cr	%Cu	%Sn	%P	%Ti
FGI	3.010	2.42	0.73	0.055	-	-	-	-	0.027	-
CGI	3.55	2.22	0.39	0.007	0.011	0.029	0.94	0.081	-	0.006
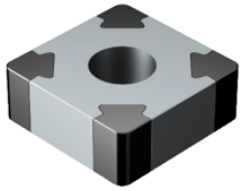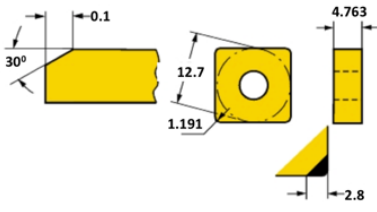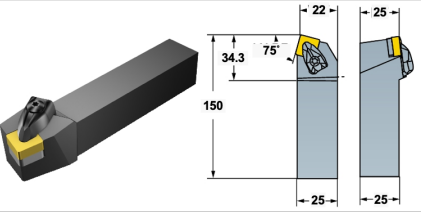
2. Experiments

2.1. Cubic Boron Nitride (cBN) Inserts

Table 3.3. Specification of three cBN inserts

Grade	Main constituent	Binder	Grain size (μm)	Supplier
CB7205	50% cBN	TiCN + Al2O3	1 & 3	Sandvik
BN250	55-60% cBN	TiN + Al2O3	1.05-1.15	Sumitomo
BN700	90-95% cBN	Co	2	Sumitomo

Table 3.4. Geometry of uncoated CBN inserts and tool holder

Insert - SNGA120412S01030A-7025	Tool holder - DSBNR 2525M 12
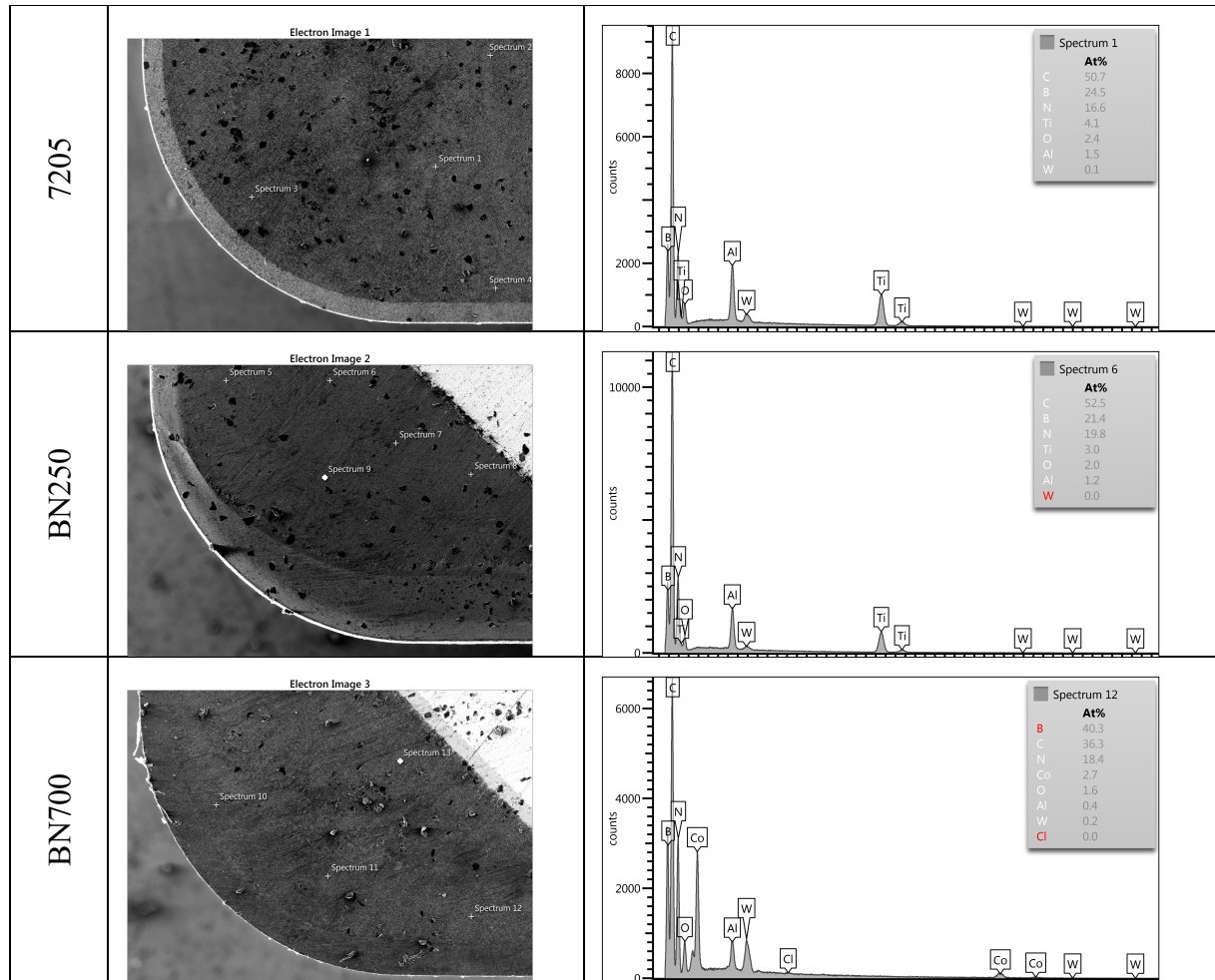
Figure 3.2. SEM/EDX data of the cBN inserts (a) 7205, (b) BN250 and (c) BN700

All the cBN tools used here have a square shape designed SNGA 120412 with flat face to be mounted on the tool holder DSBNR 2525M 12 with both rake and clearance angles of -6°. The inserts with no chip breaker is expected to provide the smoother variations of cutting temperature on the rake face. Three commercial grades of cBN inserts are 7025 grade with 50% cBN and the rest binder of TiCN and Al_2O_3, supplied by Sandvik Coromant (Herbron, KY), BN250 with 55-60% cBN and the rest binder phase of TiN and BN700 with the cBN content up to 90-95% and Co-based binder, the latter two supplied by Sumitomo Electric Carbide, Inc (New Berlin, WI). The details and geometries of cBN inserts and tool holder are given by the suppliers as shown in Tables

3 and 4, respectively. To verify the chemical composition of the cBN inserts, the SEM/EDX technique is used to identify the chemical elements in each insert. As shown in Figure 3.2, the SEM/EDX data showed some deviation from the chemical composition provided by the suppliers. The presence of Al and O indicated by SEM/EDX at the same locations indicates the presence of Al_2O_3 which is high dissolution-resistant for all three grades of cBN [129]. Figure 3.2 shows CB7205 with the most Al_2O_3 content, BN700 with the least Al_2O_3 content and BN 250 in between the two. Evident by the higher Al content compared to CB7205, BN 250 may have additional Al in the binder phase.

2.2. Experimental set-up

Continuous straight turning experiments on the FGI and CGI bars were carried out. The single-pass turning experiments were processed in Hass TL1 CNC lathe (Haas Automation, CA, U.S.A) at three distinct speeds, 400, 600 and 800 m/min, in dry condition. The depth of cut and the feed rate was kept consistently at 1.5 mm and 0.2 mm/rev, respectively, throughout the experiments.

2.3. Measurements

After each turning experiment, the inserts were etched with a 10% HCl solution to remove the adhesion layers, the crater wear is measured by using the Confocal Laser Scanning Microscope (Fluoview FV1000, Olympus, Center Valley, PA, USA) at 10x of magnification and 1 μm of step size. The 3D-crater profile is constructed using our Matlab program which employed the Wavelet filtering to eliminate the noise and artifacts inherent from the height encoded image obtained by the confocal microscopy [130, 131]. To measure the depth of the crater, the 2D profile was extracted at the deepest of the crater along the chip flow direction which is 75° from the cutting edge as shown in Figure 3.3. In addition, rake surface was investigated with Scanning Electron Microscope (SEM) (6610LV) with Energy Dispersive X-ray (EDX) to analyze the elemental

distribution on the flank and rake surfaces. The SEM/EDX was operated at 10keV, 10 mm working distance and 70x magnification.
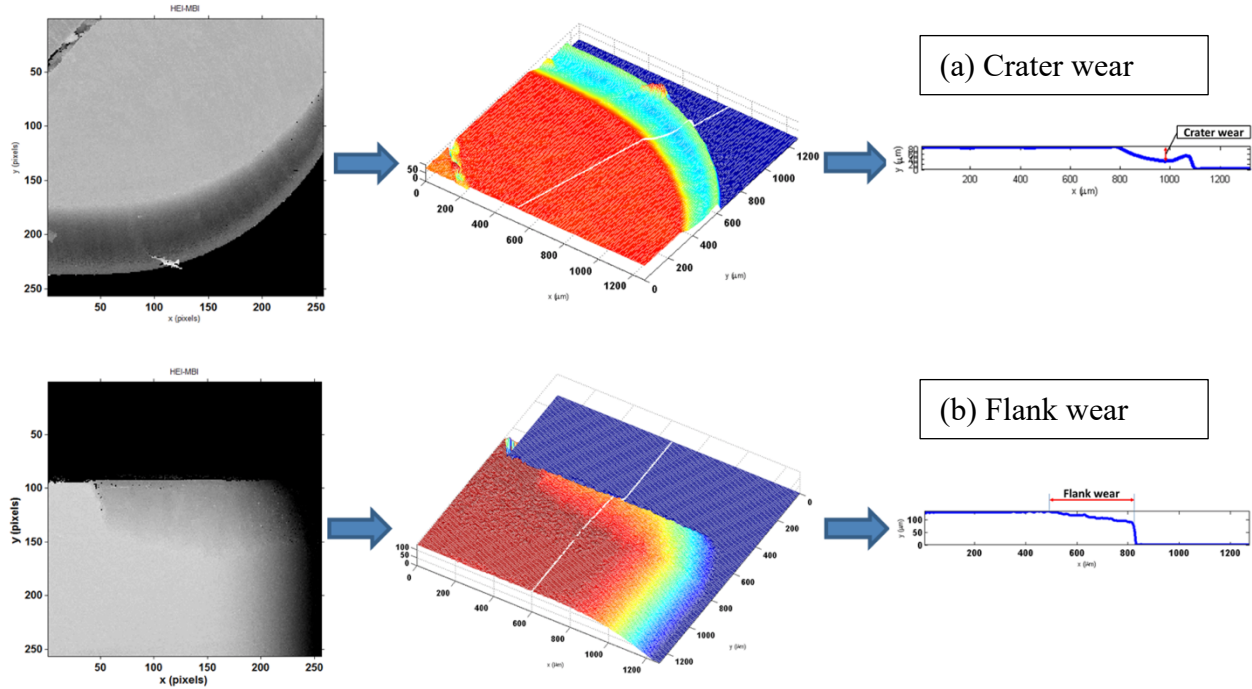
Figure 3.3. Crater (a) and Flank (b) wear measurements from HEI image obtained from CLSM

3. Results

3.1. Flank Wear

Flank wear data for FGI and CGI are collected and presented in Figure 3.4. The flank wear data for FGI are presented in solid lines while those for CGI are presented in dotted lines. The flank wear with CGI is much more extensive than that with FGI. In general, we expect that a higher the cutting speed means more flank wear, as the BN700 inserts showed. However, in turning FGI with CB7205 and BN250 inserts, both with significant Al_2O_3 content, the flank wear decreased with increasing in cutting speed. Few [132, 133] also observed such unusual behavior. The flank wear on BN250 was slightly higher when cutting FGI at 800 m/min and, substantially smaller than

those from the two slower speeds. A similar trend, not as distinct, on the flank wear when turning

CGIs can be observed with all three cBN inserts.
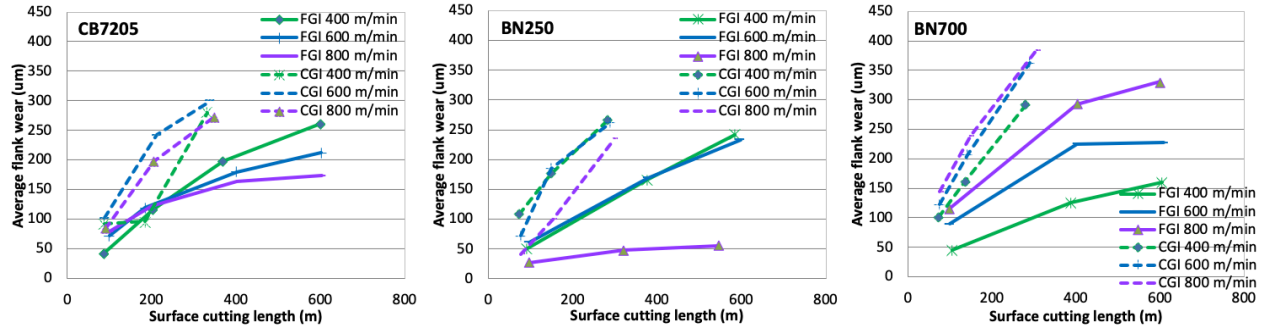
Figure 3.4. Comparison of flank wear after turning FGI and CGI with (a) CB7205, (b) BN250, (c) BN700 at 400, 600 and 800 m/min.
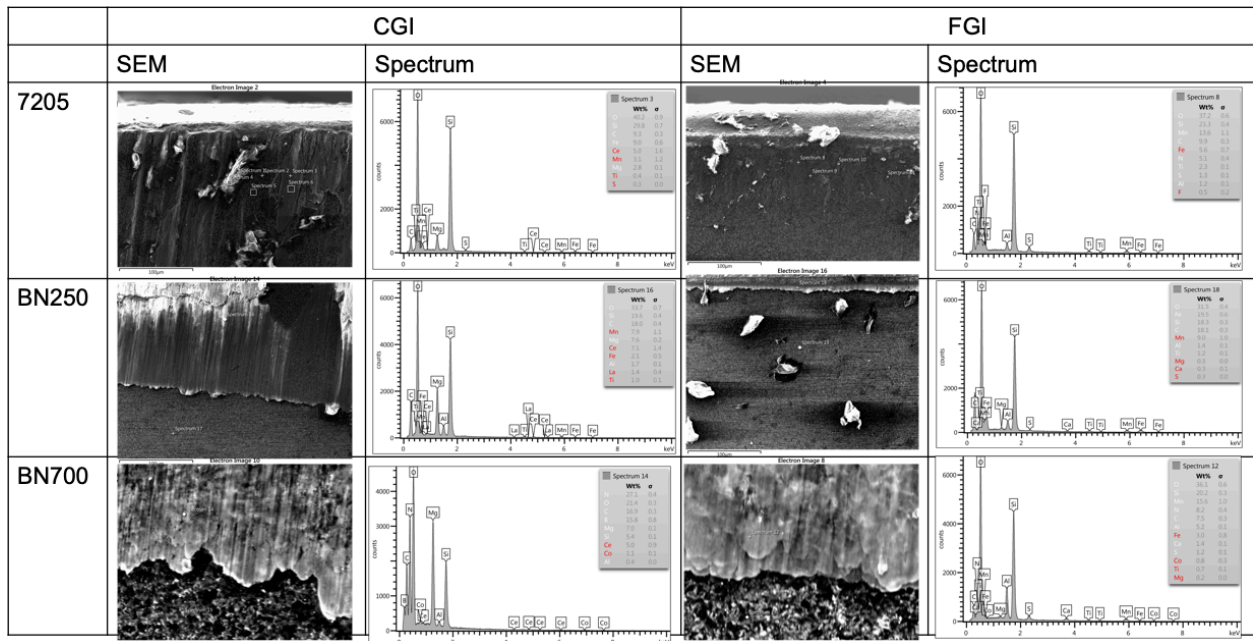
Figure 3.5. The Flank face of CB7205, BN250 and BN700 after cutting CGI and FGI at 800 m/min.

Figure 3.5 shows the worn flank face images and their elemental spectrums obtained by using

SEM/EDX technique at a magnification of 400x. Obviously, the adhesion layers is covering the

flank faces extensively on all cBN grades. With CB7205 and BN250 grades with mainly Al_2O_3

binder phase, this adhesion layers in cutting CGI are more extensive compare to those in cutting

FGI. However, in the case of BN700 grade with a Co binder phase, these adhesion layers are similar on both CGI or FGI. The chemical compound of these adhesion layers is mainly Si and O which the fraction of Si and O is close to 1:2, consistent with SiO_2. Figure 3.6 shows the flank face images and the elemental mapping of Si and O captured using the SEM/EDX technique of the CB7205 grade after cutting FGI at 800 m/min with 350 m of cutting distance. Clearly, the presence of Si and O at the same locations represent the presence of SiO_2 and their presence is more extensive nearby the cutting edge of the flank face. Quantitatively, all three grades of cBN inserts were collected after machining with FGI and CGI at same cutting distance of 350 m at the cutting speed of 800 m/min.
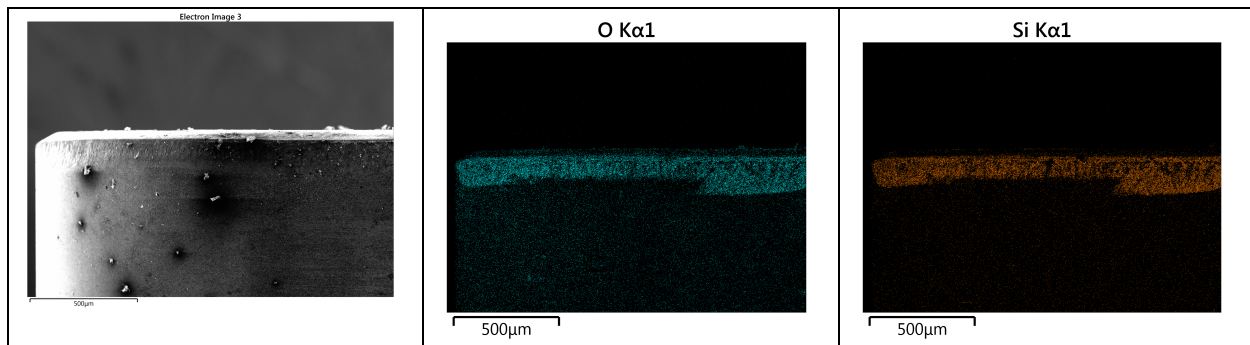
Figure 3.6. The Flank face of CB7205 after cutting FGI with distance of 350 m at 800 m/min.

Figure 3.7 shows the chips generated during our experiments which were organized to show the change, starting from the cutting speed of 100m/min to 800m/min. The connected, not quite continuous, chip is generated at the cutting speed of 100m/min and they become much more discretized as the cutting speed increases. At the cutting speed of 800 m/min, this chip comes off from the cBN inserts like 'random firework' during machining. The flank wear has slight increased because the random chip did not fully engaged with the insert, and not generate the high cutting temperature on the inserts. As will be shown in the next section, this increase crater wear.

	800 m/min	600 m/min	400 m/min	250 m/min	100 m/min
CGI					
FGI					
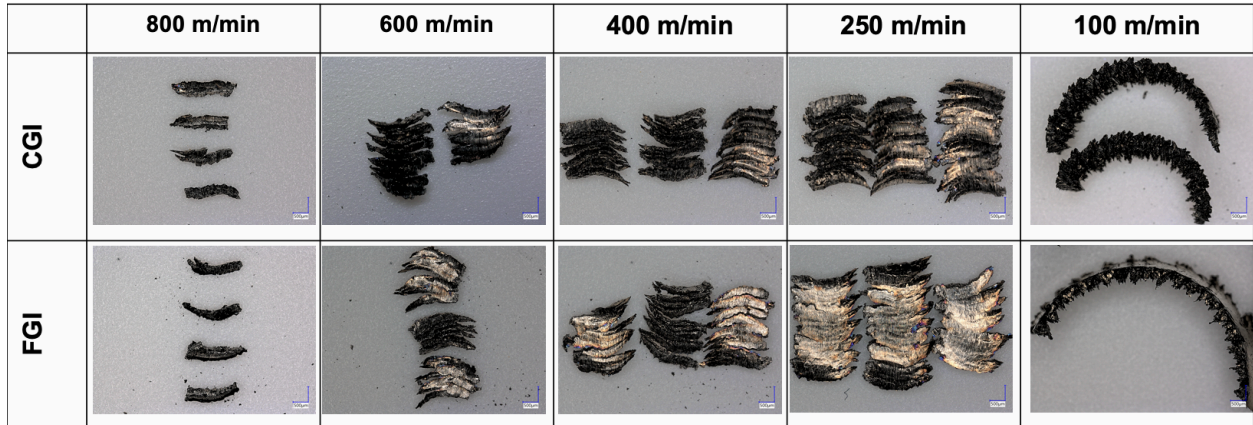
Figure 3.7. Comparison of the chips generated during machining FGI and CGI from the cutting speeds of 100m/min to 800 m/min.

3.2. Crater wear

	400 m/min	600 m/min	800 m/min
FGI			
CGI			
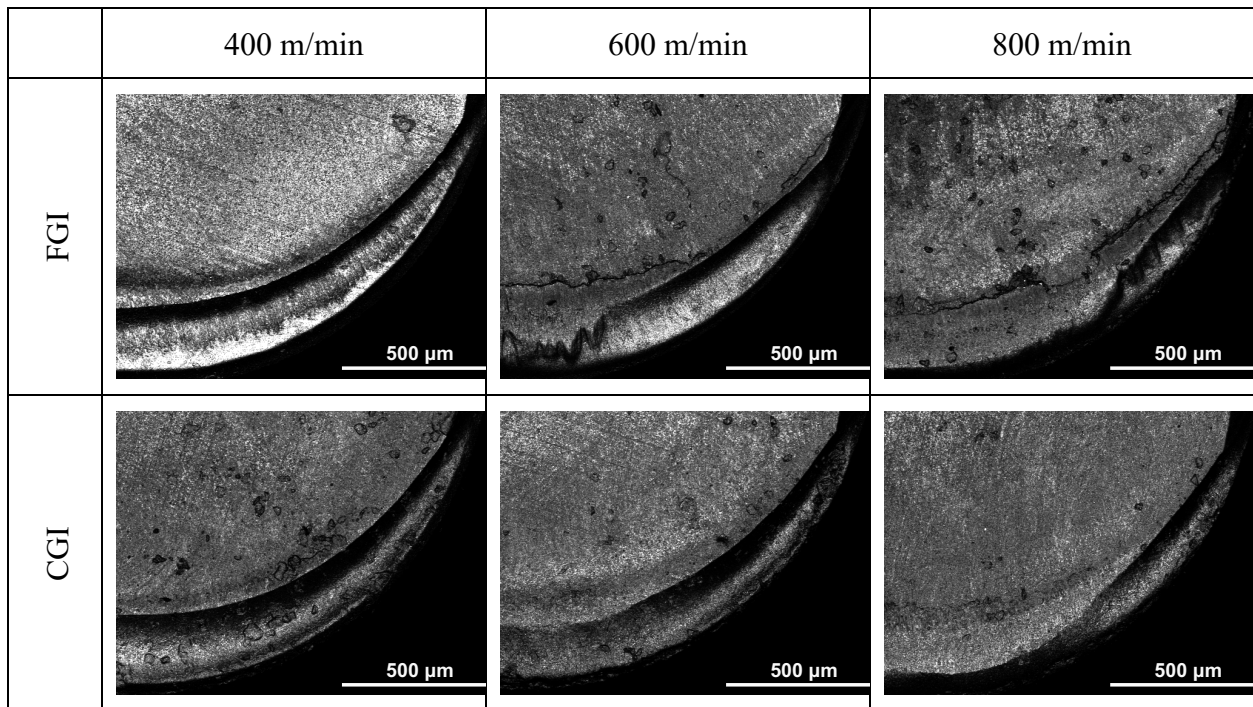
Figure 3.8. The crater wear of CB7205 after cutting the surface length of 350 m.

Figure 3.8 illustrates the worn rake face images obtained by confocal microscope after etching. The CB 7205 inserts were obtained after cutting FGI and CGI for the cutting length of 350 m at the cutting speed of 400, 600 and 800 m/min. Obviously, the size and shape of crater

49

wear and the location of the deepest crater depth change with the cutting speeds. At the low cutting speed, the crater size is larger than that from the high cutting speed and the location of the deepest crater depth leans toward the tool edge as the cutting speed increases. When cutting both FGI and CGI at 800m/min, the crater wear took place on in a much more concentrated area, which may make the chip to be discharged in a 'random firework' behavior.
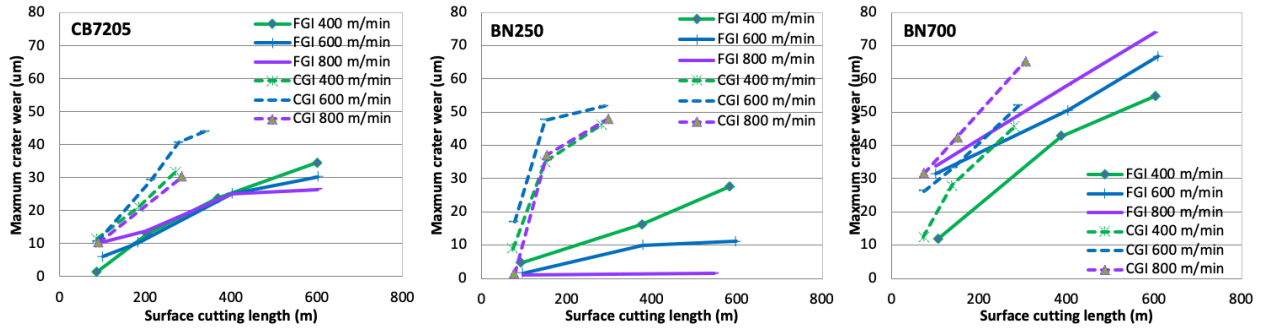
Figure 3.9. Comparison of crater wear after machining FGI and CGI with (a) CB7205, (b) BN250, (c) BN700 at 400, 600 and 800 m/min

Figure 3.9 shows the comparison of the maximum crater wear depths and their evolution between FGI and CGI with the three cBN inserts at cutting speeds of 400, 600 and 800 m/min. Obviously, similar to flank wear, the crater wear of all three cBN inserts from turning CGI is higher than FGI. With two ceramic-binder grades, CB7205 and BN250, the crater wear after turning CGI is up to three times higher than FGI for all cutting speeds. Surprisingly, at the cutting high speed of 800 m/min, the crater wear of CB7205 and BN250 after turning CGI is less than that from the cutting speed of 600 m/min. A similar phenomenon on the flank wear, as observed in the earlier section. In machining FGI, the crater wear of CB7205 and BN250, both cBN inserts with alumina binder phase, after turning FGI also is reduced as the cutting speed increases. However, with BN700, the cBN insert with the Co binder phase, the crater wear after turning both CGI and FGI increased with increasing cutting speed.

50

3.3. Adhesion Layers
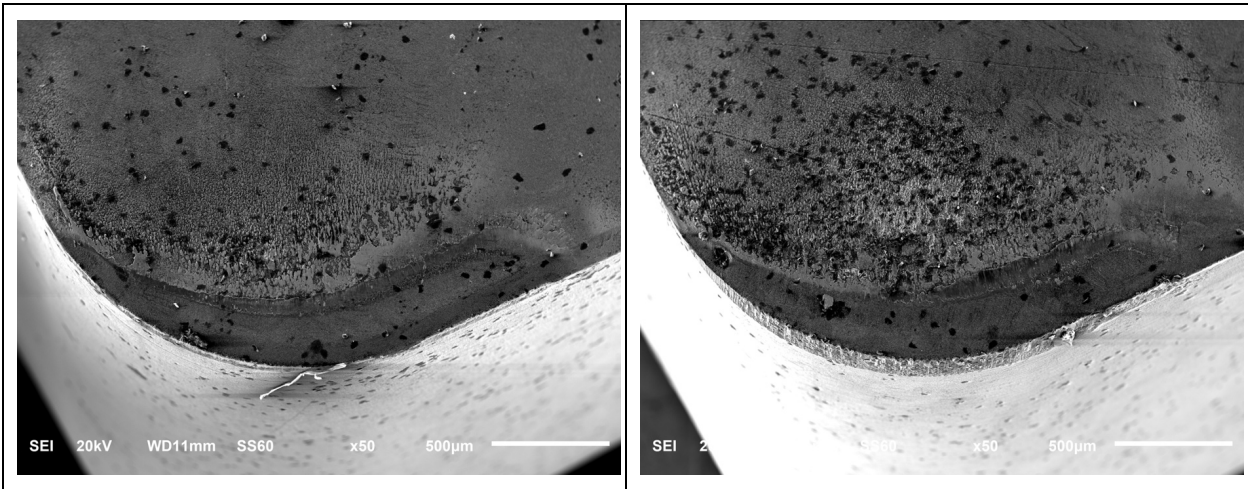
Figure 3.10. SEM of cBN 7205 after machining FGI (a) and CGI (b)

After machining CGI and FGI, the cBN tools were covered by adhesion layers which are composed of the compounds from both work and tool materials as observed in Figure 3.10. To identify the chemical composition of the adhesion layers after turning CGI and FGI, the cBN inserts were also analyzed with SEM/EDX before and after etching. The SEM parameters were 10 keV, working distance of 10 mm and magnification of 2500x.

3.3.1. MnS layer
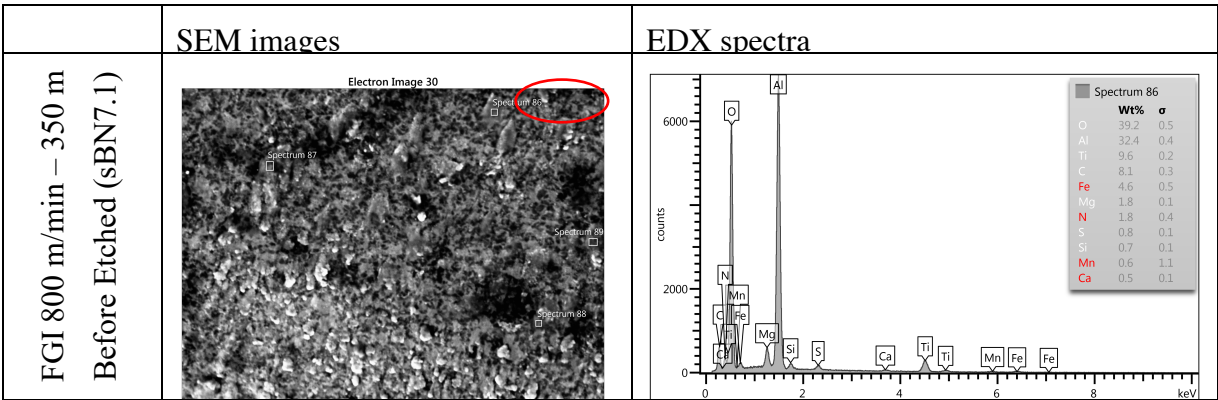
Figure 3.11. SEM/EDX data before etching of cBN inserts machining FGI at 600 m/min with cutting length of 350 m
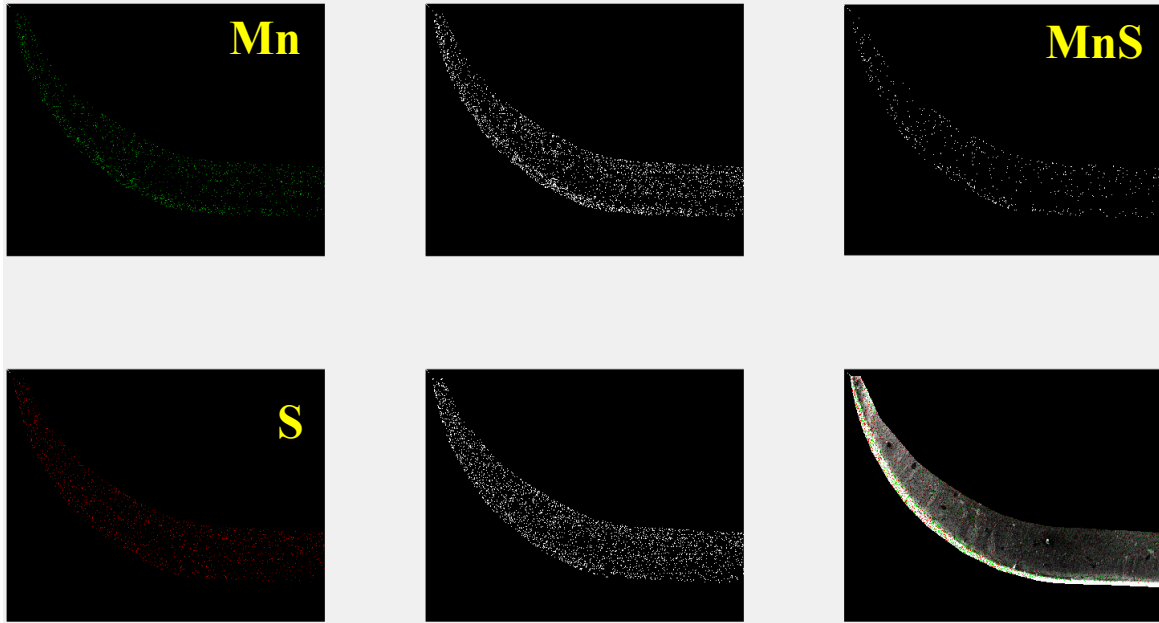
Figure 3.12. Image processing to detect the MnS from SEM image and elemental maps.
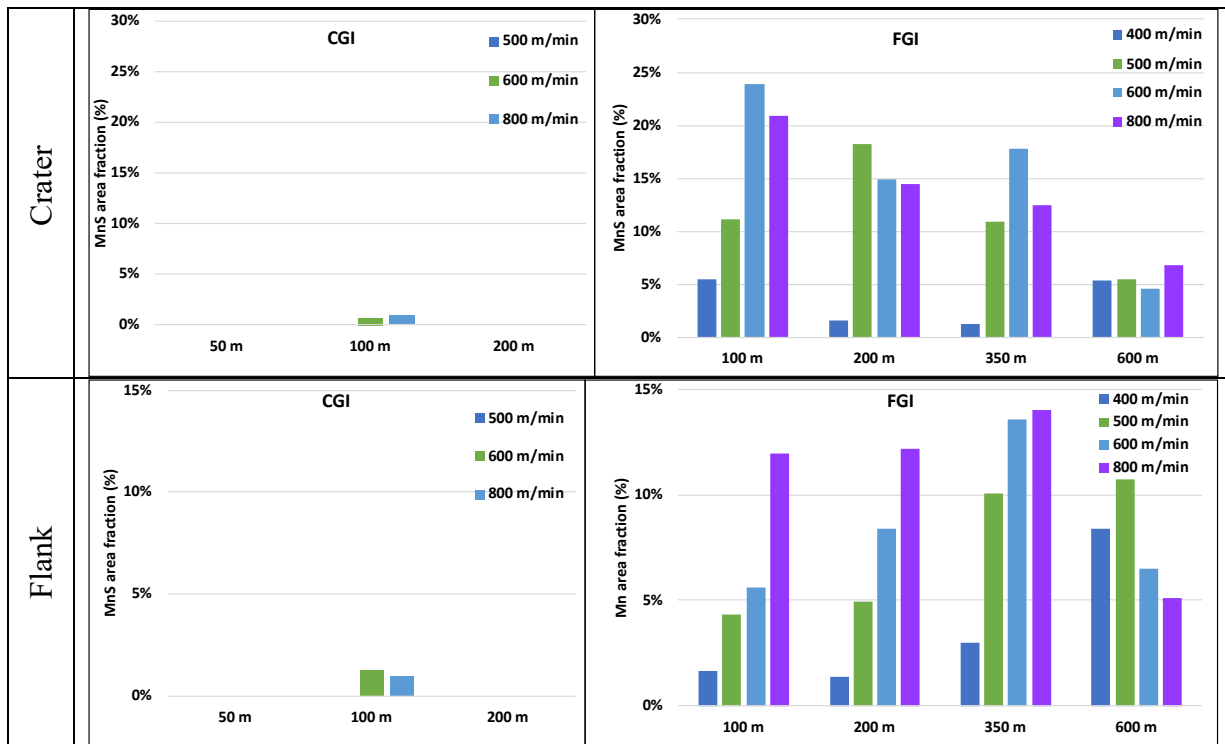
Figure 3.13. The area fraction covered by MnS on the crater (a) and flank (b) faces of CB 7205 after turning CGI and FGI
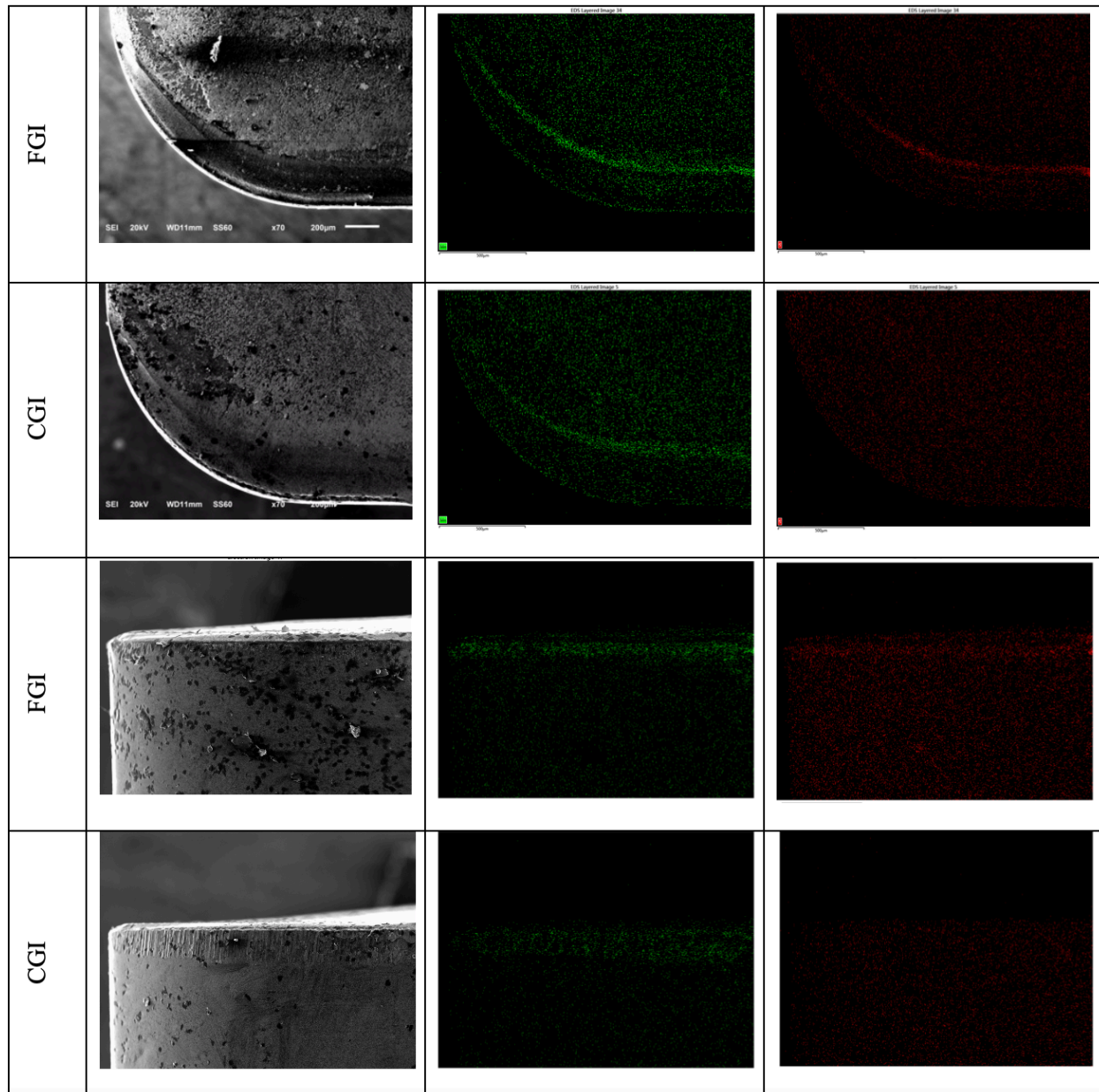
Figure 3.14. Element mapping data on rake and flank face of CB7205 machining FGI and CGI at speed of 800 m/min with cutting distance of 350 m.

Gastel et al. [28] carried out machining CGI and FGI at speed of 10, 100, 400 and 800 m/min with two cBN grades from De Beers, AMB90 which has 90% cBN and Al-based binder and DBC50 which has 50% cBN and TiN-based binder. They claimed that the presence of the MnS layer covering extensively on the tool surfaces after turning FGI at the high cutting speeds reduced tool wear. The lack of the MnS layer on the cBN inserts when turning CGI lead to the

poor machinability. To confirm the presence of MnS layer formation, SEM/EDX measurement were carried out to identify the elements present on the rake faces. Figure 3.11 presents the SEM image on the rake surface of cBN grade CB7205 and the elemental data obtained at 2500x from the insert machining FGI at 800 m/min. Obviously, the results from EDX spectra on the insert before etching indicate that the adhesion layer is made of mainly iron with the limited amounts of Mn and S in small patches after cutting FGI [25].

To investigate the MnS layer on the rake face quantitatively, an image processing program developed in Matlab was developed to process the SEM image and the elemental mappings from SEM/EDX measurement. Figure 3.12 shows six images (with 2 rows and 3 columns) of the same rake face. The two left images (the first column of images) show the elemental maps for Mn and S, which filtered into black and white images shown on the two middle images (the second column of images). The upper right image (the third column and the first raw of image) show the intersection of Mn and S, representing the presence of MnS and the final lower right image is the SEM image. Therefore, the MnS compound on the rake face can be identified (the image labeled MnS in Figure 3.12).

In order to form an extensive MnS layer, the MnS inclusions present in the original microstructure of FGI must smear onto the tool surface and accumulate on the tool surfaces. Figure 3.13 was obtained by retrieving the CB7205 inserts after cutting CGI and FGI and carrying out the EDX on the crater surfaces. For CGI, no such layer was observed except less than 1% of the total areas fraction after cutting 100 m, which may be the abnormality in the microstructure with MnS inclusion(s). For FGI, the cutting process was carried out to the cutting length up to 600 m. As evident in Figure 3.14, the MnS did not accumulated as the cutting process continued, not

supporting the extensive MnS layer on the tool surfaces of a cBN insert. In fact, the highest concentrations of Mn and S are deposited on the tailing edge, not on cutting edge or crater surface.

3.3.2 Al₂O₃ layer
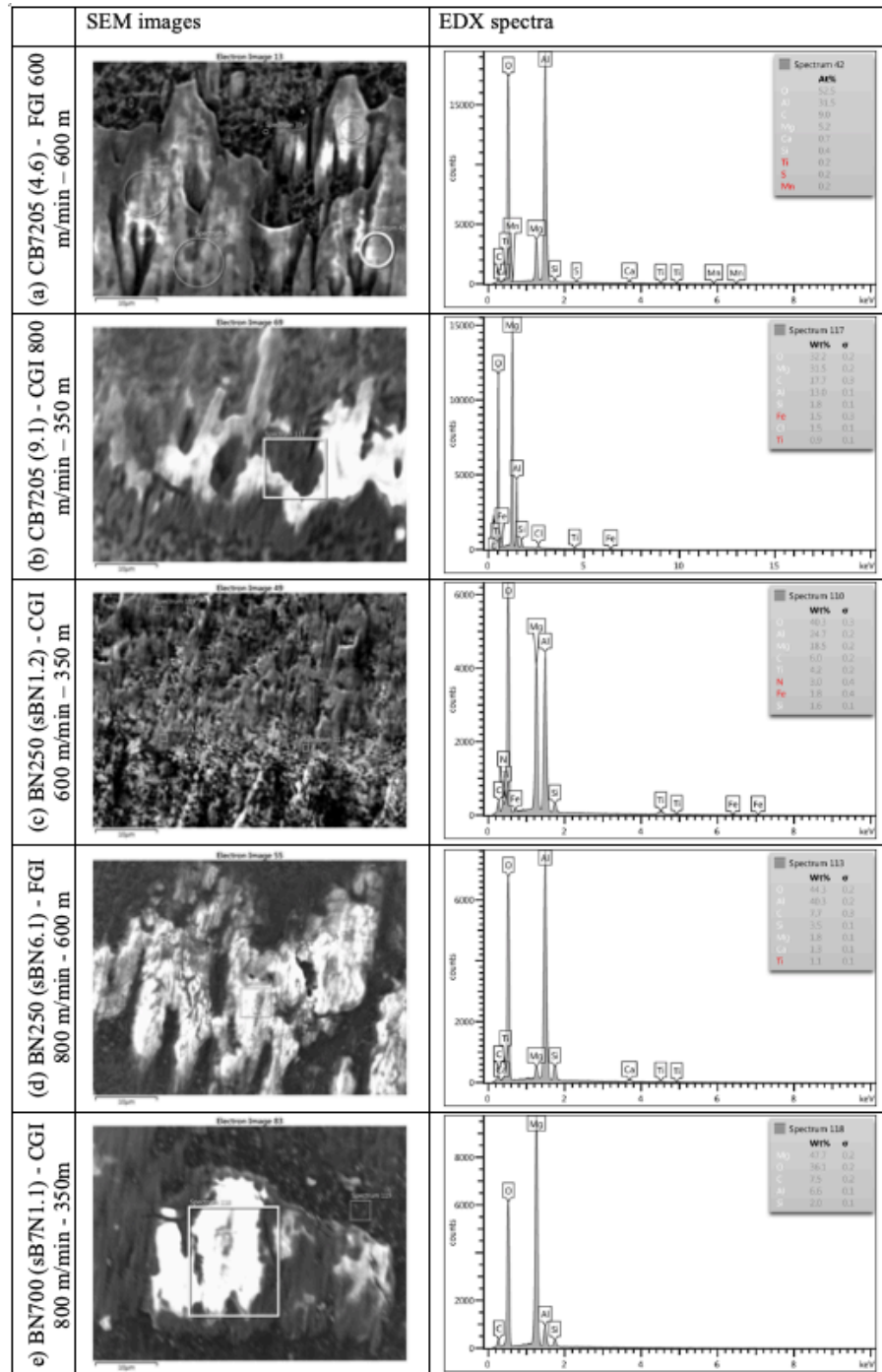
Figure 3.15. SEM/EDX data after etching time of 30 minutes of all three inserts machining CGI and FGI

After the cBN inserts were etched for 30 minutes in 10% HCL, instead of the iron-oxygen layer, another extensive adhesion layer, composed of mainly Al and O, was detected with the elemental identify technique. The location selected in the SEM images and the corresponding EDX data are shown in Figure 3.15. Figure 3.15(a-e) shows that the extensive aluminum-oxygen adhesion layer appeared at the crater surfaces of all three grades of cBN inserts after cutting CGI at the cutting speed above 800 m/min and FGI at 600 m/min. Additionally, there is evidence of the Al_2O_3 adhesion layer deposited and pressed to the crater as shown in Figure 3.16. The grey spots are TiCN and Al_2O_3 and the black spots are cBN as observed from backscatter (BSC) images of fresh cBN inserts. After machining CGI and FGI, Al_2O_3 shows as a grey area is continuously spread to cover the crater as shown in Figure 3.16.b and 3.16.c for CGI and FGI, respectively. FGI form more stable Al_2O_3 layers which survive etching for 6 hours while the Al_2O_3 layers generated on CGI did not survived after 1 hour.

FRESH	CGI at 800 m/min	FGI at 800 m/min
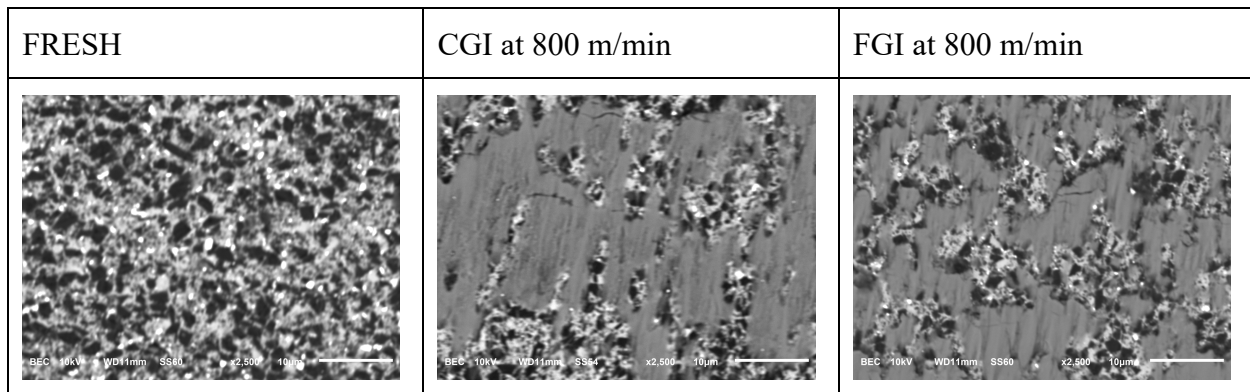
Figure 3.16. BSC images of (a) Fresh and cBN machining (b) CGI and (c) FGI at speed of 800 m/min (after etching 30 mins)

3.4. Investigation of Crater Wear

The image processing procedure described in Figure 3.12 was applied to identify the Al_2O_3 adhesion layer on the rake face. Figures 3.17 and 3.18 presents the area fraction if the total crater area occupied by Al_2O_3 on three grades of cBN inserts after turning FGI and CGI. Clearly, the

crater wear decreased with increasing cutting speed when turning CGI and FGI using CB7205 and BN 250 as mentioned above because of the Al_2O_3 formation, which functions as the dissolution barrier [58] when cutting at high speed. For CGI, obviously, the area fraction of Al_2O_3 layer at the cutting speed of 800 m/min increased compared to those at the cutting speeds of 400 and 600 m/min and the area fraction of Al_2O_3 increased as the cutting length increased, implying that the accumulation of Al_2O_3 increases as the cutting process continues. Therefore, it is clear that the formation and growth of Al_2O_3 layer occurs as the high cutting speed. The Al_2O_3 layer has the extremely low solubilities into iron, so it protected from the crater from wear during machining [134,135]. For FGI, the Al_2O_3 layer is formed at the cutting speeds of 600 and 800 m/min and grew more extensively as the cutting length increased. However, BN700 with the Co-based binder phase, the Al_2O_3 layer was not stable as the Co binder is not stable at the temperature above 800°C [136]. Therefore, the machinability difference between FGI and CGI comes from the formation of stable Al_2O_3 layer when cutting FGIs at high cutting speeds.
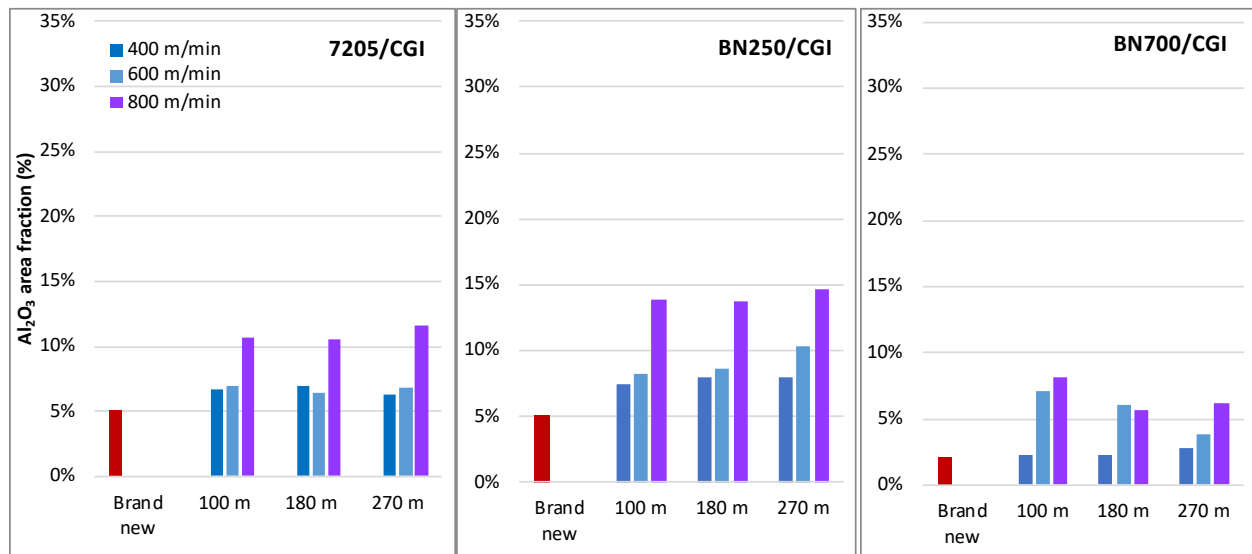
Figure 3.17. Evolution of Al2O3 area fraction in the crater of (a) 7205 grade, (b) BN250, (c) BN700 machining CGI at 400, 600 and 800 m/min.
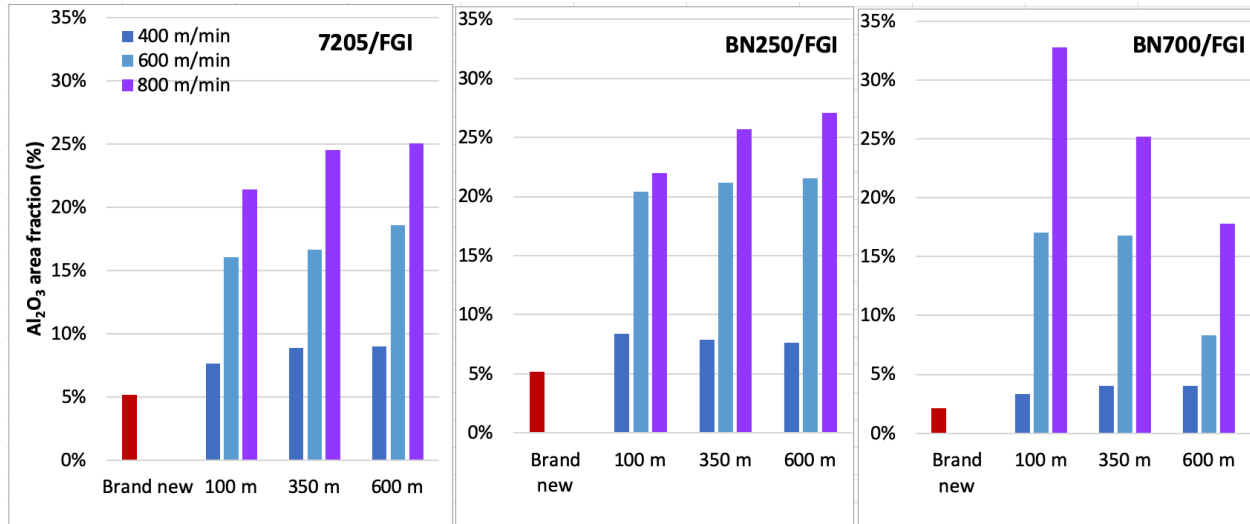
Figure 3.18. Evolution of Al2O3 area fraction in the crater of (a) 7205 grade, (b) BN250, (c) BN700 machining FGI at 400, 600 and 800 m/min.

3.5. Investigation of Flank wear

One aspect of machinability that was not paid attention there for so far is the flank wear, which has also significantly reduced as the cutting speed increases with the CB7205 and BN250 inserts. The main wear mechanism for flank wear is the abrasive action by the hard phases. The contents of cementite phase (the most abundant abrasive phase in the cast iron) do not differ between FGI and CGI, both at around 10 % in weight [25] and the rest of carbon mostly exist as graphite phases, each iron with distinct morphology. However, as the cutting speed increases, the cutting temperature reaches high enough to transform the pearlite phase (alternating layers of cementite and ferrite) into the austenite phase. In such condition, the hard cementite phases in both FGI and CGI are dissociated into the matrix of austenite phase as the phase transformation takes place [137]. The abrasive action on the flank face will be significantly diminished if the phase transformation occurs while being traversing across the flank wear land. Therefore, this explains the main reason behind the reduction in flank wear as the cutting speed increases with the CB7205 and BN250 inserts on Figure 3.4(a & b). The question is then why such phenomenon did not

58

occur on the BN700 inserts shown in Figure 3.4(c). The main reason is the difference in the thermal conductivity among the cBN inserts. The thermal conductivity of cBN is reported to be as high as 1300 W/mK compared to the diamond with the highest thermal conductivity of 2000 W/mk. The thermal conductivities of cBN inserts, mainly due to the content and nature of the binder phases, ranges between 150 and 700 W/mk according to [138] and some studies [139, 140] used as low as 44 W/mk for the thermal conductivities of a certain cBN insert. The BN700 inserts contains 90-95% cBN contents while the CB7205 and BN250 inserts contains 50-60% cBN contents with the rest in TiCN or TiN and Al_2O_3, both of which have the thermal conductivities between 10 and 20 W/mK. Thus, the thermal conductivity of BN700 is significantly higher than those of CB7205 and BN250 inserts.

To support this argument, the commercial finite element analysis (FEA) code called DEFORM 2D v.11.2 was applied to understand the cutting process. DEFORM 2D v.11.2 is capable to generate the segmentation chip corresponding to our actual experiments. The cBN inserts are modeled as a mechanically rigid but thermally conductive object with 3252 tetrahedral elements and 3504 nodes while the work material was modelled with the Johnson and Cook (J-C) model with 426 element and 471 nodes as

$$\bar{\sigma} = (A + B\bar{\varepsilon}^n)\left(1 + Cln\left(\frac{\dot{\bar{\varepsilon}}}{\dot{\bar{\varepsilon}_0}}\right)\right)\left(1 - \left(\frac{T - T_{room}}{T_{melt} - T_{room}}\right)^m\right)$$

with $\bar{\sigma}$ is the equivalent flow stress, $\dot{\bar{\varepsilon}}$ is the equivalent plastic strain, A, B, C, m & n are the fitting parameters, T is the working temperature, T_{room} is the room temperature and T_{melt} is the melting temperature. The parameters of J-C model for FGI and CGI were collected for FGI with $A = 470MPa, B = 250MPa, C = 0.004, m = 1.1$ & $n = 0.1$[141] and for CGI with $A = 260MPa, B = 1010MPa, C = 0.013, m = 1.1$ & $n = 0.47$ [142]. The friction coefficient with

the cBN inserts was assumed to be 0.25 for all cases. The parameters of the J-C models for FGI and CGI were imported through the user defined flow stress models. To represent the distinct thermal conductivities of CB7205 (or BN200) and BN700, multiple turning simulations were run with the thermal conductivities of 100 and 500W/mK at three cutting speeds used in our machining experiment. The average flank temperature under each simulation condition was collected and presented in Table 3.5, which shows the significantly higher flank temperatures with K=100 W/mK compared to those with K=500 W/mK. A similar phenomenon was reported in our previous work [102] with cutting titanium alloy with polycrystalline diamond (PCD) and carbide inserts with distinct thermal conductivities. Moreover, the transformation temperature for FGI and CGI at the atmospheric pressure is around 780ºC [25], which can be significantly reduced with the additional pressure of about 1GPa at the flank interface estimated from the FEA simulations based on Clapeyron's equation. With the results with the thermal conductivity of 100 W/mK, the average flank temperatures possibly at 600 m/min and definitely at 800 m/min may reach high enough for the phase transformation to occur from the pearlite phase to the austenite phase in both FGI and CGI. Consequently, the flank wear shown on in Figure 3.4 (a and b) was reduced as the cutting speed reached 600 and 800 m/min for the CB 7205 and BN250 inserts. However, the high thermal conductivity of 500 W/mK would not allow the flank temperature to reach the phase transformation temperature, which is evident by the flank wear shown in Figure 3.4(c). The flank wear in this case increased with the increase in cutting speed.

The flank wear behavior of CGI shown in Figure 3.4 behaves similarly as that of FGI even though the flank wear is significantly higher for CGI. The flank wear attained from cutting CGI is distinctively higher than that from cutting FGI due to the microstructural difference between FGI and CGI as shown in Figure 3.1(a) and (b). The flank wear is the manifestation of the abrasive

action by the hard phase like the cementite phase. Even though the similar amounts of cementite phase exist in FGI and CGI, the stiffness and strength of CGI are significantly improved over those of FGI. Supported by the enhanced stiffness and strength of CGI, the cementite phase intensely abrades the flank surface. Similar distinct flank wear phenomena happened in our earlier studies on low alloy steels with the cementite phase in pearlitic and speridized microstructures [48] as well as titanium alloy heat treated in four distinct microstructures [136].

Table 3.5. Average Flank Temperature estimated from Our Simulation

Temperature	FGI		CGI	
	100W/mK	500 W/mK	100W/mK	500W/mK
400m/min	357 ºC	255 ºC	359 ºC	256 ºC
600m/min	539 ºC	365 ºC	555 ºC	367 ºC
800m/min	718 ºC	479 ºC	729 ºC	483 ºC

4. Discussion

Because the maximum crater is measured to represent the extent of crater wear, the maximum crater temperature is of our interest as the location of maximum crater wear coincides with the location of maximum crater wear. Table 3.6 shows the maximum crater temperatures which were significantly higher than the average flank temperatures. Even though the average flank temperatures were similar between FGI and CGI, the maximum crater temperatures with FGI were significantly higher than those of CGI. This is one factor that enables FGI to form a much more stable Al_2O_3 layer. As presented in Figure 3.9, the crater wear decreased as the cutting speed increases when turning CGI and FGI with the CB7205 and BN250 inserts. This is unexpected as the dissolution wear dominates crater wear and should increase exponentially as the cutting speed (crater temperature) increases. The main reason behind this unexpected behavior is the formation

of the Al_2O_3 layer, which has the extremely low solubilities into iron, protecting from the crater wear during high speed machining of ferrous alloys [54, 134]. However, with the BN700 insert, the area fraction of the Al_2O_3 layer (most likely formed by the oxidation of Al present as a binder phase) was extremely small and unstable (meaning not able to grow continuously as shown in Figures 3.17(c) and 3.18(c)) as the Co binder, the main binder phase for BN 700, is not stable at the temperature above 800°C [143]. Also note that with the difference in crater wear after cutting FGI and CGI is not significant with the BN700 insert as shown in Figure 3.9, even though the flank wear did not behave similarly as in Figure 3.4.

Table 3.6. Maximum Crater Temperature estimated from Our Simulation

Temperature	FGI		CGI	
	100W/mK	500 W/mK	100W/mK	500W/mK
400m/min	754 ºC	755 ºC	377 ºC	378 ºC
600m/min	1120 ºC	1000 ºC	545 ºC	548 ºC
800m/min	1470 ºC	1180 ºC	704 ºC	717 ºC

The formation of extensive Al_2O_3 layer has a significant implication on the machinability of cast iron when using the CB7205 and BN250 inserts (both with Al_2O_3 binder phase). That is the main reason why the Al_2O_3 coating is extensively used in many multi-layered coated carbide inserts. Figure 3.19 depicts the formation of Al_2O_3 layer from the individual grains of Al_2O_3. Figure 3.19(a) shows the Al_2O_3 binder phase within the cBN matrix, which may contain other compounds (e.g.: TiCN as in the CB7205 insert). With the nonuniform rake temperature, certain locations within the rake face reached high enough temperature to dissolve away cBN particles (see Figure 3.19(b)) while the Al_2O_3 particles, which is resistant to dissolution are exposed and, under the high shear loading and temperature, deformed into a layer (see Figure 3.19(c)). When

cutting FGIs, the formation of Al_2O_3 layer is much more extensive (almost double in terms of area fraction) compared to CGIs as evident in Figures 3.17 and 3.18. This is corroborated by the maximum crater temperature on Table 3.6, which shows a significantly higher temperature for FGI. A higher temperature will enable the Al_2O_3 binder phases to coalesces as in sintering in powder metallurgy. In particular, the BN250 insert was very effective in forming the Al_2O_3 layer even at the cutting speed of 600 m/min as shown in Figures 3.17 and 3.18.

(a) Fresh cBN insert   (b) Exposure of Al2O3 phases   (c) Deformation of Al2O3 phases
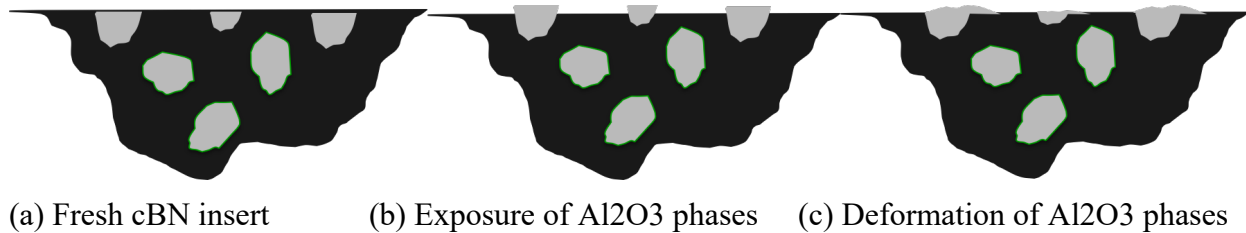
Figure 3.19. Exposure and Deformation of Al2O3 Binder phases within cBN matrix.

The machinability difference between CGI and FGI also comes from the stability of the Al_2O_3 layers when cutting FGI. The Al_2O_3 layer formed while cutting FGI at the cutting speed of 600 and 800 m/min could not be removed after etching for more than 60 hours, demonstrated in Figure 3.20 by comparing two CB7206 inserts, one after cutting CGI and the other after cutting FGI at 800 m/min. This may come from the higher crater temperature when cutting FGI. However, the formation of Al_2O_3 layers must have been enhanced by the elements present in FGIs. As reported in [143, 144], the addition of 0.3% (in weight) Mn_xO has improved the sintering of the Al_2O_3 powder with the average size of 5 m at the sintering temperature between 1450 and 1600°C and the addition of MgO (with the significant Mg presence in CGI) retards the sintering of the Al_2O_3 powder. Thus, when cutting FGIs, the presence of about 0.73% Mn in the matrix FGIs (see Table 3.2) enables to 'coalesce or sinter' the individual Al_2O_3 binder phases on the rake face even after a small fraction of Mn may be consumed to form MnS_2 inclusions in FGIs. On the other hand, when cutting CGIs, the 0.39% of Mn in CGIs may not be enough to provide the sintering

enhancement but also the significant Mg presence in CGI retards the sintering of the Al_2O_3 powder. Therefore, the Al_2O_3 layers formed while cutting FGI were much more stable which survived even after etching for 60 hours while the Al_2O_3 layers formed after cutting CGI did not survived after etching more than 1 hour. Therefore, the nature of Al_2O_3 layers formed between FGI and CGI is significantly different. We can conclude that the machinability difference between FGI and CGI come from the formation of more extensive and extremely stable Al_2O_3 layer when cutting FGIs at high cutting speeds.

Etching Time	CGI at 800 m/min	FGI at 800 m/min
0.5 hrs		
60 hours		
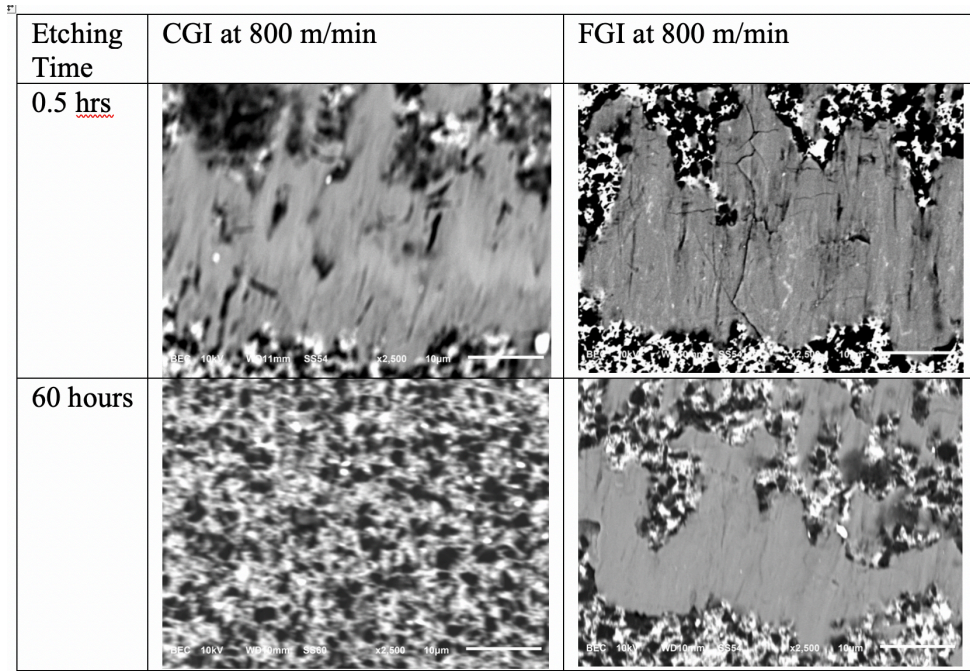
Figure 3.20. Back Scatter images on the rake faces of CB7205 at the cutting speed of 800 m/min after cutting CGI and FGI for 350m

The formation of Al_2O_3 layer caused 'the double crater' observed on the CB7205 and BN250 inserts. As shown on Figure 3.15, the Al_2O_3 layer is formed between the cutting edge and the trailing edge on the rake face, not on the upper left corners of the CB7205 and BN250 inserts, the same corner where 'double craters' were formed on the CB7205 and BN250 inserts. The smaller crater near the corner radius is formed (see Figure 3.8 at 800m/min) as the temperature within the

double crater is not high enough to shear the Al₂O₃ binder phase. The formation of the double

crater promotes the generation of the 'firework' chips. This also may impact the flank wear even

though that is beyond the scope of this study. By contrast, the BN700 inserts without the Al₂O₃

binder phase have the typical smooth crater wear observed in high speed metal cutting.
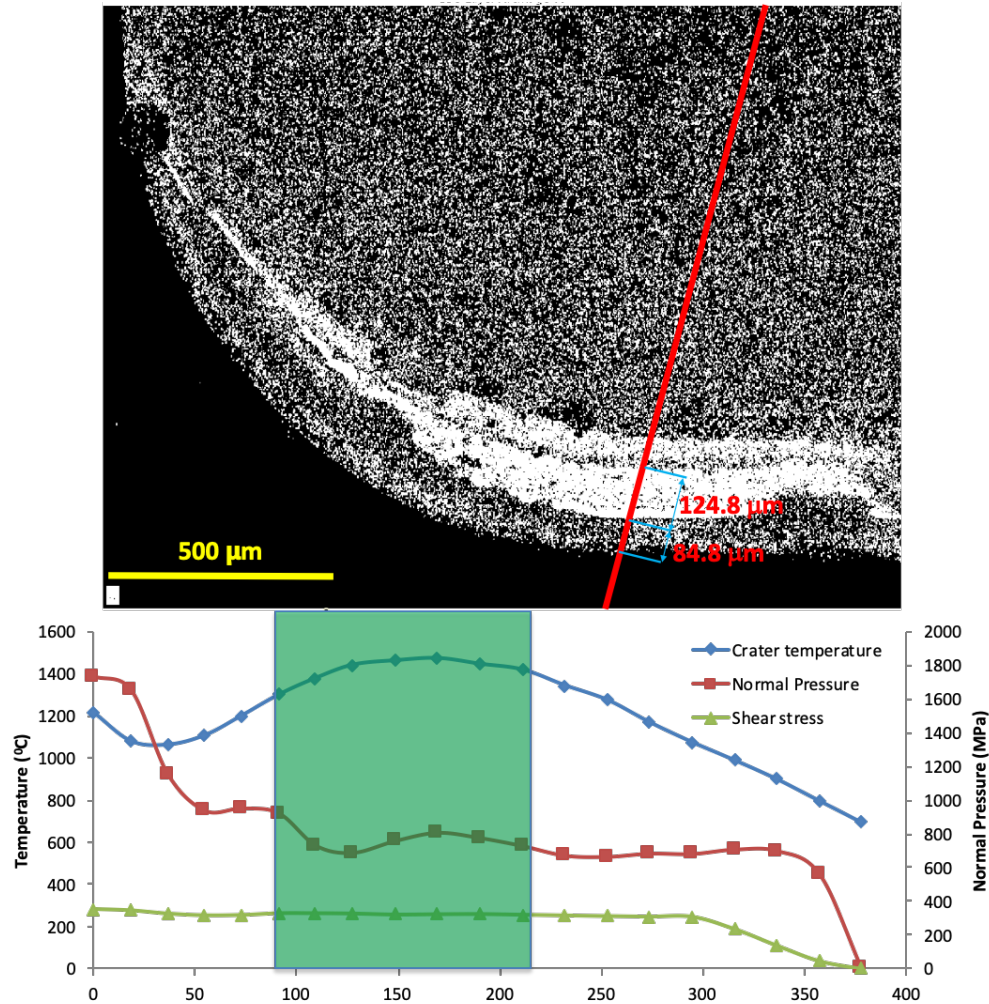
Figure 3.21. The Elemental Mapping representing the location of the Al2O3 layer on the crater of CB7205 after cutting FGI at 800m/min and the crater temperature, normal and shear stresses along the chip flow direction (represented in a red line) from the simulation with K=100 W/mK

To confirm this with the FE simulation, the location of the Al₂O₃ layer within the crater was

superimposed with the temperature and interface traction (both normal pressure and shear stress)

results from our machining simulation presented in Sec. 3.4. The top figure on Figure 3.21 presents

the location (light shaded region) of Al_2O_3 layer formed on the CB7205 after cutting at 800m/min with the line representing the chip flow direction. The location of the Al_2O_3 layer on the CB7205 after cutting at 800m/min is presented from the cutting edge along the chip flow direction between 84.8 and 124.8 , which nearly matches the region with the highest crater temperature. The shear stress and normal pressure on the insert are nearly uniformed. This temperature is high enough to deform the Al_2O_3 binder phase and 'coalesces or sinter' more readily with the additional Mg coming from FGI as the matrix of the rest of the cBN phase is exposed.

5. Conclusion

We presented our study on the formation of 'layers or patches' mainly made of MnS, SiO_2 and MgO and Al_2O_3 between FGI/CGI and cBN inserts in order to identify the root cause for the machinability difference between FGI and CGI. Among them, the Al_2O_3 layer coming from the Al_2O_3 binder phase in certain grades of cBN inserts is the major contributor for the machinability difference between FGI and CGI. Our experiments showed that the extensive MnS layer claimed in [28] to protect the cBN inserts when turning FGI at high cutting speed cannot protect the insert. In fact, numerous MnS 'patches' in total covering only up to 24% of crater wear and 13% of flank wear land did not accumulate as the turning process continues. The MnS patches may provide the lubricity between work material and cutting tool, which may mildly reduce the cutting temperature but are constantly being removed during the machining process. Instead, we determined that the main reasons for the excellent machinability of FGI is the formation of not only an appreciably larger area of Al_2O_3 layer but also a much more stable Al_2O_3 layer on the crater surface when cutting FGI and the microstructural impact on flank wear with CGI providing much more aggressive abrasion conditions. With the cBN inserts with the Al_2O_3 binder phase, the Al_2O_3 layer was exposed, after the other materials of cBN inserts including cBN particles dissolved away at

high cutting temperature, and deformed under high shear loading and temperature and transformed or sintered into protective Al_2O_3 layers. The stable Al_2O_3 layer provides a solubility barrier in machining ferrous materials including FGI and CGI. On the other hand, the cBN insert with Co binder phase (e.g.: BN700) did not perform as well the cBN inserts with Al_2O_3 binder phase (e.g.: CB7205 and BN250) due to the fact that Co binder is not stable at high temperature. Flank wear is mainly shown by the contribution of thermal conductivity of the cBN insert and the phase transformation of pearlite phase with hard cementite phase into the austenite phase, which eliminates the abrasive action by the hard cementite phase in FGI and CGI. More extensive flank wear on CGI comes from the nature of the microstructures, which are substantially harder and stronger compared to FGI. In particular, the following conclusions are drawn.

- The MnS inclusions in FGIs smeared onto the cBN tools as discrete patches, which are not stable to protect the cutting tool. The formation of MnS 'patches' on the cBN inserts is not the main reason to explain the excellent machinability of FGI.

- At the cutting speed of 400, 600, and 800 m/min, FGI has better machinability than CGI based on the flank and crater wear. However, the particular wear behaviors, where the increase in cutting speed reduced both flank and crater wear, were observed. The reduction in flank wear were attributed to the phase transformation of pearlite with cementite into austenite, which is achieved by the increase in flank temperature, which is boosted by the low thermal conductivity of the cBN inserts with the Al_2O_3 binder phase. In addition, once the maximum crater temperature reaches high enough to form the Al_2O_3 layer with its low solubility into iron, crater wear is reduced when cutting both FGI and CGI. The formation of the Al_2O_3 layer on the rake face triggered 'double' crater where more extensive crater formed outside the formed Al_2O_3 layer within the crater.

- The cBN inserts with Al_2O_3 binder phase outperformed the cBN insert with Co binder phase in machining both FGI and CGI mainly due to the presence of the stable Al_2O_3 layers when cutting FGI.

- The difference in flank wear between FGI and CGI comes from the microstructural difference, which is the main reason behind the enhanced mechanical properties of CGI over FGI.

CHAPTER 4: THE EFFECT OF FIBER ORIENTATION ON TOOL WEAR IN EDGE-TRIMMING OF CFRP LAMINATES[†]

1. Work materials

The CFRP laminates used for the experiments were acquired from Innovative Composites Engineering (White Salmon, WA, USA). The carbon fiber prepreg obtained was HR40, an intermediate modulus fiber with an aerial weight of 200 grams/m^2 from Mitsubishi (Sacramento, CA, USA). The matrix was an epoxy resin system of DGEBA epoxide with DDS diamine curing agent (Aldrich Chemical Company, St. Louis, MO). The CFRP laminate had a total thickness of 3.3 mm with an average ply thickness of 0.114 mm. Two 254 mm × 102 mm × 3.3 mm cross-ply CFRP laminate coupons, $[0_{14}/90_{14}]$ and $[45_{14}/135_{14}]$, were fabricated for this study. The average fiber volume fraction of these laminate coupons is approximately 60%.

2. Experimental Procedures

2.1 Edge-Trimming Experiments
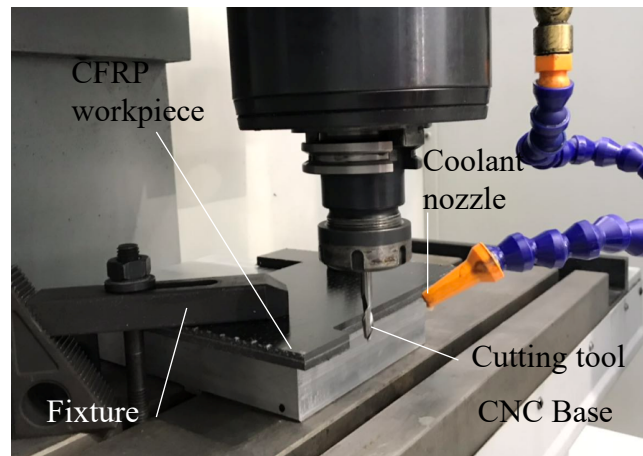
Figure 4.1. Experimental set-up for the edge-trimming experiment

---

A 3-axis CNC milling machine (Minimill, HAAS, Oxnard, CA, USA) was used for the edge trimming experiments. The edge-trimming was done by up-milling, which is reported to produce better surface quality in machining of CFRP [145]. The edge-trimming experiments were conducted under two spindle speed conditions at 1000 (19.9 m/min) and 6000 (119.7 m/min) RPM under flood cooling due to the excessive debris generation. Other parameters such as feed per revolution, depth of cut, and coolant application were kept constant. All edge-trimming experimental conditions including geometric information for the uncoated tungsten carbide (WC-Co) 2-flute end-mills (MSC Industrial Supply, Elkhart, IL) used in the experiment are summarized in Table 4.1. The set-up of the edge-trimming experiments is shown in Figure 4.1. Cutting tool paths for the experiments were carefully designed to investigate the tool wear progress or wear evolution by interrupting the edge-trimming process. To investigate the initial stages of tool wear, data points at cutting distances of 0.25 m, 0.5 m, 1 m, and 1.5 m were chosen. These experiments were followed by using cutting distances of 2 m, 4 m, 6 m, and 8 m to investigate the steady state region of tool wear.

Table 4.1. Summary of edge trimming experiments

Cutting tool	Type: 2-flute solid carbide end mill; Material grade: Micro-grains; Tool diameter: 6.35 mm; Shank Diameter: 6.35 mm; Length of cut: 19.05 mm; Overall Length: 63.5 mm; and Helix angle: 30°
Spindle speed	1000 RPM; and 6000 RPM
Feed	0.0508 mm/rev. (0.002 inch/rev.)
Depth of cut	0.508 mm (0.020 in)
Tool traveling distances	0.25 m; 0.5 m; 1 m; 1.5 m; 2 m; 4 m; 6 m; and 8 m
Other conditions	Up-milling; Flood coolant using water-soluble cutting fluid

2.2 Laser Confocal Microscope Measurement
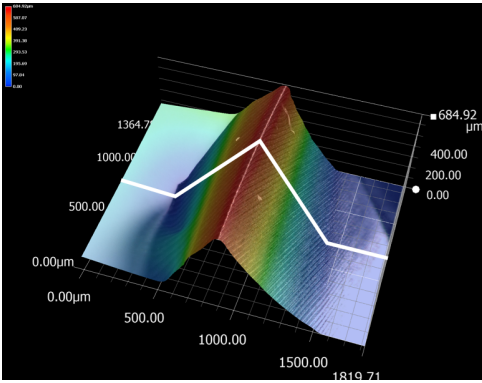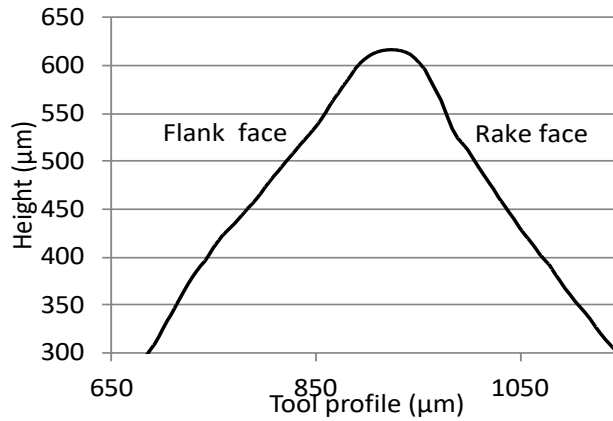
(a) 3D tool profile	(b) 2D tool profile extracted from 3D profile (a)

Figure 4.2. 3D and 2D Tool profiles

The dust collected on the end-mills after each trimming experiment was removed by applying compressed air. Subsequently, the end-mills were cleaned in an ultrasonic bath containing acetone for 30 minutes (Model 5300, Ultrasonic Power Corporation, Freeport, IL, USA) using the modulation frequency of 1000 kHz, temperature of 140°C, and power of 120W. The moisture was then removed by keeping the carbide tools on a hot plate (Super Nuova, Thermo Fisher Scientific, Waltham, MA, USA) set at 90°C for a few minutes. Afterwards, the tool edge was measured using the laser confocal digital microscope, VHX-6000 (Keyence Corporation®, Itasca, IL, USA). The 3D geometry of the cutting edge shown in Figure 4.2(a) was generated by capturing a series of 2-D optical images with a step size of 1 μm and magnification of 200x. For the tool wear analysis, the wedge-shaped tool profile was extracted from the midpoint of each tool section to represent the wear profile of the cutting edge as shown in Figure 4.2(b).

2.3 SEM Analysis

Both the cutting tool and the machined CFRP surface were studied using two scanning electron microscopes (Quanta 3D 200i, Thermo Fisher Scientific®, Waltham, MA, USA and ASPEX PSEM-75, Delmont, PA, USA). SEM images were taken at 20 keV using approximately 60% filament drive. Prior to SEM investigations, the tools were cleaned by ultrasonicating in acetone at a frequency of 1000 kHz, temperature of 60°C, and power of 60W for 30 minutes. The same ultrasonication technique was applied as well to clean the machined CFRP coupons for 5 minutes.

3. Tool Wear Characterization Process

Flank wear is a major tool wear mode in metal cutting and is defined by the flank wear land (V_B) on the flank face. This flank wear land has been simply adopted to represent the extent of tool wear in CFRP machining. However, the dominant wear mode in CFRP machining has been identified as the blunting of the cutting edge, commonly known as edge rounding [67]. As noted previously, Figure 4.3 illustrates a typical 2D profile of the cutting tool edge after edge trimming CFRP. All the 2D edge profiles presented in this study were obtained from the 3D confocal microscope images. As shown in Figure 4.3(a), the flank wear land (V_B) is quantified as the distance of tool material removed measured from the tool edge on the flank side. The edge radius as presented in Figure 4.3(b) is computed based on the 2D edge profile. This radius is found using a best fit circle (the dotted line) to the 2D edge profile of the worn tool with a series of measured points: P_1, P_2, and P_3. P_1 is the tangential intersection with the flank face, P_2 is the tangential intersection with rake face and P_3 represents a series of points measured from the worn cutting-edge profile between P_1 and P_2. The GRG (Generalized Reduced Gradient) non-linear algorithm [146] was applied to calculate the coordinates of the center point and radius of the best fit circle.

In addition to the flank wear land and edge radius, the worn area of the tool is defined by the area difference, represented by the shaded area (Figure 4.3(b)), between the fresh and worn tool. Since the 2D profiles are extracted by the 3D confocal microscope measurements at the same reference line on each tool section, the worn area of a tool can be calculated by numerical integration between two 2-D profiles, the worn profile and the fresh profile.

(a) Flank wear land   (b) Edge radius (dotted circle) and worn area (shaded area)
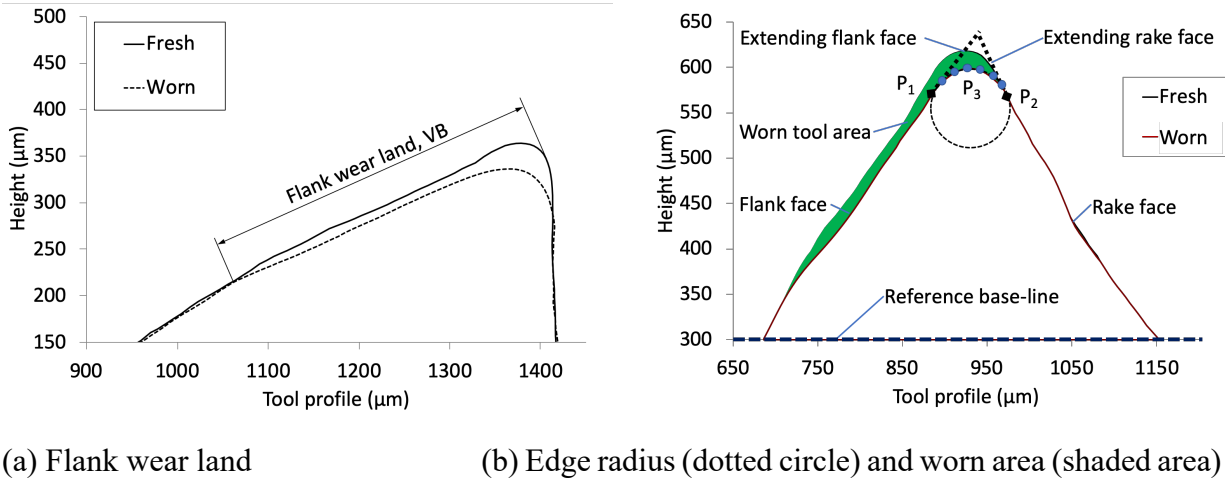
Figure 4.3. Three tool wear measurement techniques

4. Characterization of the Machined Surface

SEM images were utilized to characterize the machined CFRP surfaces. As shown in Figure 4.4(a), the carbon fibers on the newly generated surface can be classified into three groups: 1) exposed fibers, 2) fiber pulled-outs, and 3) fibers covered by matrix due to matrix smearing. The exposed fibers are clearly visible in the SEM images as they have been separated from the matrix. Figure 4.4(b) shows the lengths of the individual fibers measured for the discussion in a later section. The pulled-out fibers are ones broken below the newly generated surface. The third dominant surface characteristic is matrix smearing which is the accumulated mass of matrix debris. The short fibers broken off from CFRP may exist but did not survive our cleaning procedure. To obtain the statistical data, the number of fibers exposed, pulled-out, and covered by matrix

73

smearing were evaluated using a randomly chosen sample area of 300 μm x 130 μm for the four ply angles after cutting 1.5 m (relatively fresh tool) and 8 m (worn tool). The number of exposed fibers and respective heights have been determined by implementing ImageJ software. The lengths of exposed fibers on 45° and 135° plies have been determined by applying a trigonometric relationship to obtain the mean value and standard deviation of the exposed height. The number of fiber pull-outs was also counted using ImageJ. The lines in Figure 4.4(b) show the process of tracking the length of each exposed fiber. After measuring each length, the exposed length of each exposed fiber was computed as well. The length of each exposed fiber from the 90° plies has been measured by tilting the surface by 45°. Finally, after identifying each matrix smearing location, the area was computed using ImageJ and the number of covered fibers due to matrix smearing were calculated based on the average fiber content.

| (a) Exposed fibers, pulled-out fibers, | (b) Exposed fiber length |
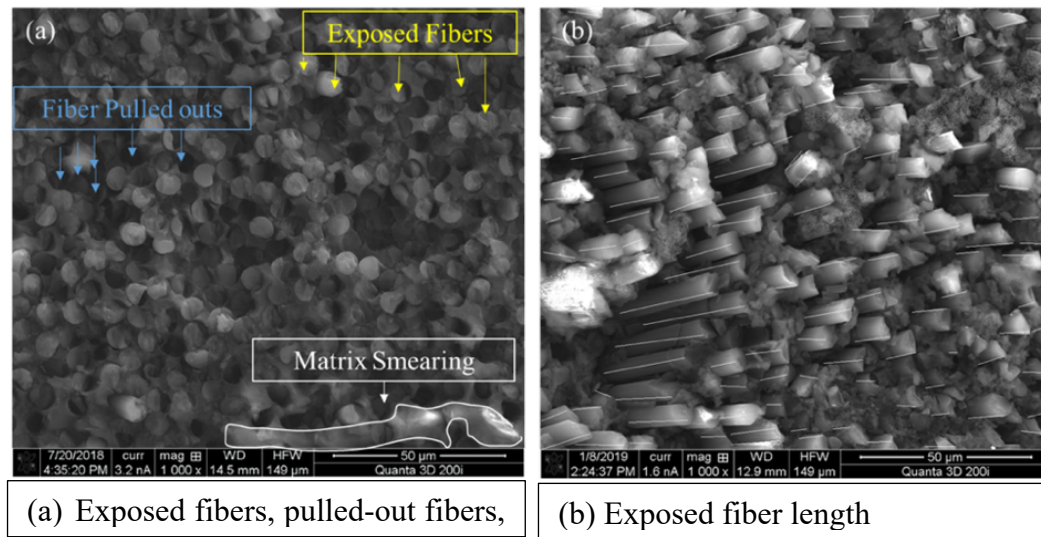
Figure 4.4. Machined CFRP surface characterization process using SEM images

5. Results and Discussion

The cutting force during edge-trimming exerted by the cutting edge can be decomposed into two, the cutting and thrust forces, which is uniquely different for each ply angle. Figure 4.5

illustrates these forces in each ply angle. For the 0° plies, the cutting direction is along the fibers and the main mechanism for chip formation is delamination, causing minimal interactions between fibers and cutting edge. By contrast, for the 90° plies, the cutting direction is perpendicular to the fiber direction, causing most interactions between fibers and cutting edge. For the 45° plies, the fibers are both pulled and sheared. For the 135° plies, the fibers are compressed while being sheared. These interactions between tool tip and workpiece have a direct impact on how carbon fibers fracture during cutting. As will be discussed, the 135° plies resulted in the 'burst' type of chip formation, which causes less interactions between fibers and cutting edge. These phenomena have direct implications on the surface finish of the CFRP.

(a) 0° plies   (b) 45° plies   (c) 90° plies   (d) 135° plies
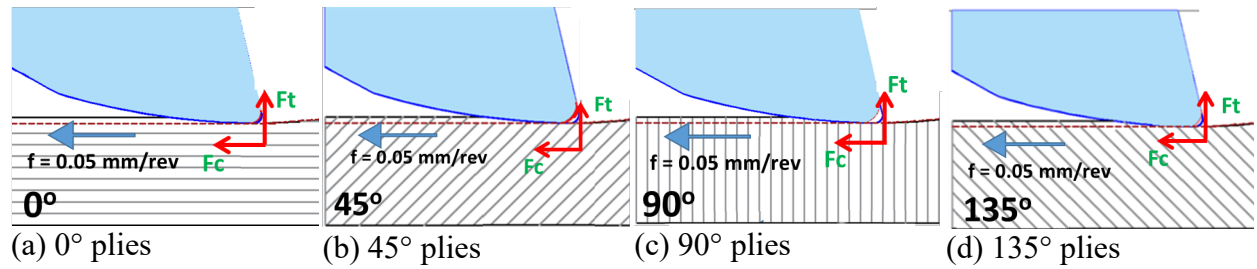
Figure 4.5. Schematics of Cutting 0°, 45°, 90°, and 135° plies

Bhatnagar *et.al* [147], Hagino [79] and Wang [70] measured the forces during orthogonal cutting of each ply. They reported the highest thrust force with the 45° plies and the lowest with 135° plies while the highest cutting force was obtained with the 90° plies and the lowest with the 135° plies. Thus, the 135° plies have overall the lowest cutting forces among the four plies. The forces in the 0° plies and the 45° plies are comparable with the slightly larger forces in cutting the 45° plies. For the 0° plies, the matrix breaks first, and the uncut fibers which are becoming the chip are bent. These fibers will eventually break due to the transverse shear stress with the small chip thickness or the bending with the larger and stiffer chip thickness due to the low shear strength of CFRP, typically 20-40 % of its tensile strength [148]. Thus, the cutting and thrust force for 0°

plies are relatively low. When cutting the 45° plies, the cutting edge directly compressed the fibers and matrix causing to break at the contact point. As the cutting tool travels, the fibers are loaded in tension, breaking every fiber along the cutting plane. With both thrust and cutting forces, the fibers are reinforcing the matrix which makes difficult breaking apart [149]. The combined load of cutting and trust forces should break the fibers in tension. Cutting the 90° plies require all the fibers to break, causing the cutting force to be the highest but not the thrust force. The 135° plies are loaded in compression along the fiber direction during cutting. Due to the low shear strength of the matrix [150], a bundle of fibers as a group would break apart from the rest of the plies, yielding a 'burst' type of chips.

5.1 The 0° Plies

(a) Flank wear land

(b) Cutting tool edge radii
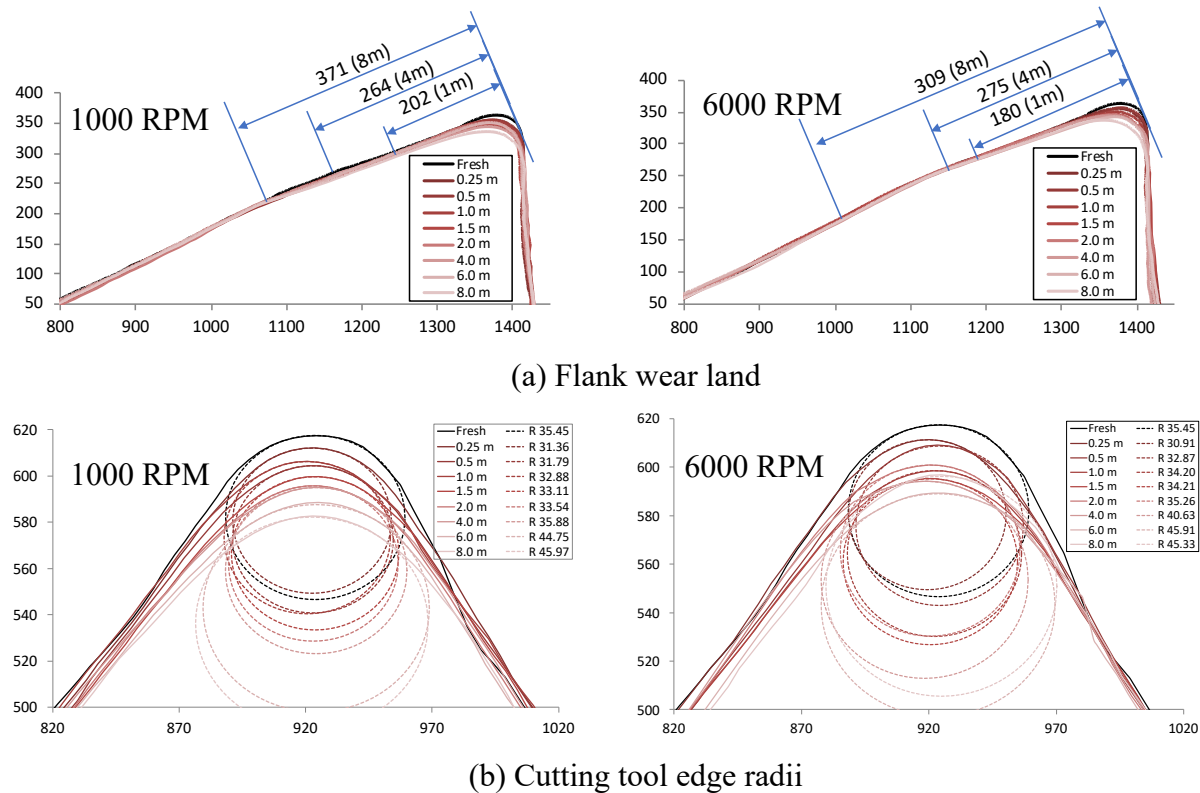
Figure 4.6. Tool wear for the 0° plies at cutting speeds of 1000 and 6000 RPM
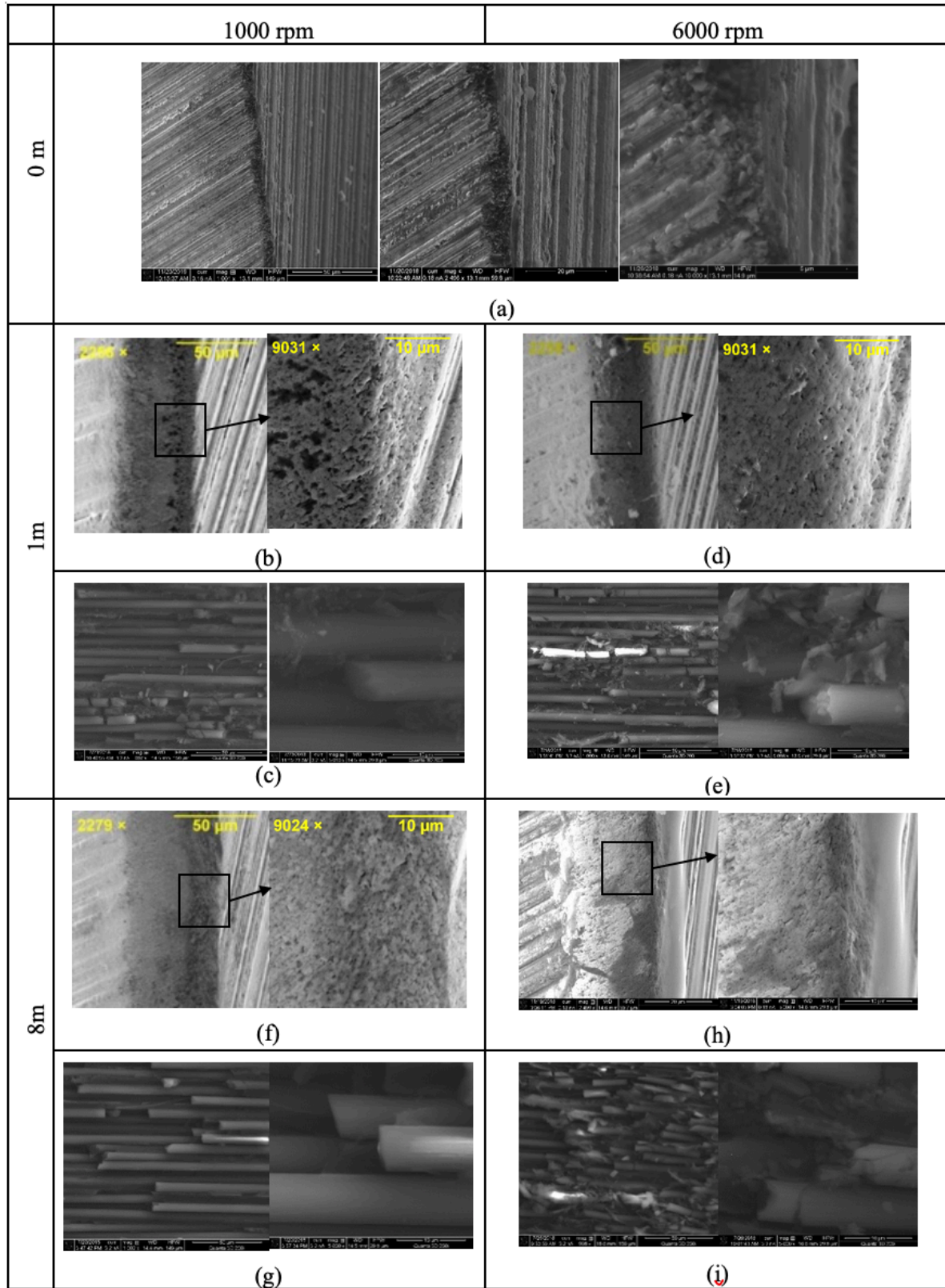
Figure 4.7. SEM images of fresh and worn tool for the cutting length of 0, 1.0, and 8.0m of 0°
orientation CFRP ply angle at cutting speeds of 1000 and 6000 RPM

Figure 4.6 presents the flank wear land, tool edge profiles and measured edge radii at various cutting distances under two spindle speed conditions, 1000 and 6000 RPM, when cutting the 0° plies. The flank wear profiles between 1000 and 6000 RPM are quite similar, indicating that flank wear is not heavily dependent on the cutting speed. The progression of flank wear land as a function of cutting length is presented in Figure 4.14 together with other ply angles. It can be observed that flank wear increases rapidly up to a cutting distance of 1.0m and then steadily increases up to 8.0 m, which can be interpreted as the initial and steady states of tool wear [71, 148]. The results of the edge-radius and worn area are presented in Figures 4.6(b) and 4.15, respectively. The edge radii for both spindle speed conditions are similar. Initially, the edge radius reduces up to a cutting distance of 0.5 m, increases steadily with cutting distance up to 6 m and becomes stabilized between 6 and 8 m. The total worn area computed from the 2-D profile of the cutting edge is presented in Figure 4.16. This result is in a good agreement with the edge radius results in general. However, the worn area does not stabilize but kept increasing even between 6 and 8 m. All three wear assessment techniques are indifferent to the spindle speed when cutting the 0° plies.

Figure 4.7 presents SEM images revealing wear damage on the end mills for both spindle speed conditions (1000 and 6000 RPM), from the fresh state to the final cutting distance of 8 m. Figure 4.8(a) shows the fresh edge of the end mill in three different magnifications, x1000, x2500 and x10,000. On each edge (b, d, f or h) in Figure 4.7, the left side is the flank surface while the right side displays the rake surface. Figure 4.7(b, d, f and h) shows the SEM images with 2000x magnification of the cutting edges with the dominant edge rounding at both cutting speeds. The surface topographies of the cutting edge after cutting 1 m have the almost identical rounded edges between 1000 rpm and 6000 rpm. Also note that the removal of the softer cobalt phases from the

harder carbide particles, which is manifested by the black pockets on the SEM images in Figure 8(b). This indicates that the wear mode is mostly soft abrasion [146], which is defined as the removal of tungsten carbide (WC) grains after the softer cobalt binder phase is removed. The SEM images of the machined surface show the unbroken and broken parallel carbon fibers. The chip formation mechanisms consist of mainly delamination with some detachment of the fibers from the matrix and fiber-matrix debonding, all of which are due to the bending of the plies to be peeled off [151]. Sometimes the bending load causes some fibers to fracture perpendicularly to the fiber axis, some in multiple places. During the cutting process, the $0°$ plies build compressive stresses to the tool surface and which causes abrasion of the soft cobalt phase. This soft abrasion dominant wear mode is consistent with 1000 RPM after cutting 8 m. However, more distinct scratches are observed on the cutting edge of the tool after cutting 8 m at 6000 RPM as shown in Figure 4.7(h). As the angle of the scratches is consistent with the cutting direction, the $0°$ fibers remove the tungsten carbide grains, resulting in hard abrasion at this speed. The corresponding machined surface after cutting 8 m at 6000 RPM also reveals severely damaged and compressed carbon fibers (Figure 4.7(i)), which are acted upon by the tool flank face with the large edge radius during the cut.

5.2 The 45° Plies

Figure 4.8 presents the tool wear results from the three assessment techniques presented in Sec. 3 with the 45° plies. Among the four plies, the flank wear increased most rapidly when cutting the 45° plies. According to Figures 4.8(a) and 4.14, the resulting flank wear between the two spindle speeds are distinct for the 45° plies despite no significant difference while cutting up to 2.0 m. The flank wear lands after cutting 4 m at 6000 RPM are about 40% higher than those at 1000 RPM. The changes in edge-radius (Figure 4.15) and worn area (Figure 4.16) over the cutting

distance are relatively small in both spindle speeds and did not differ between two spindle speeds. Compared to the 0° plies, the difference in the worn area between two spindle speeds is slightly different. With the 45° plies, the higher spindle speed condition resulted in significantly more flank wear when compared with those at the lower cutting speed condition. Thus, at a higher cutting speed, the wear accumulates more significantly on the flank side without significantly increasing the edge radius.

(a) Flank wear land

(b) Cutting tool edge radii
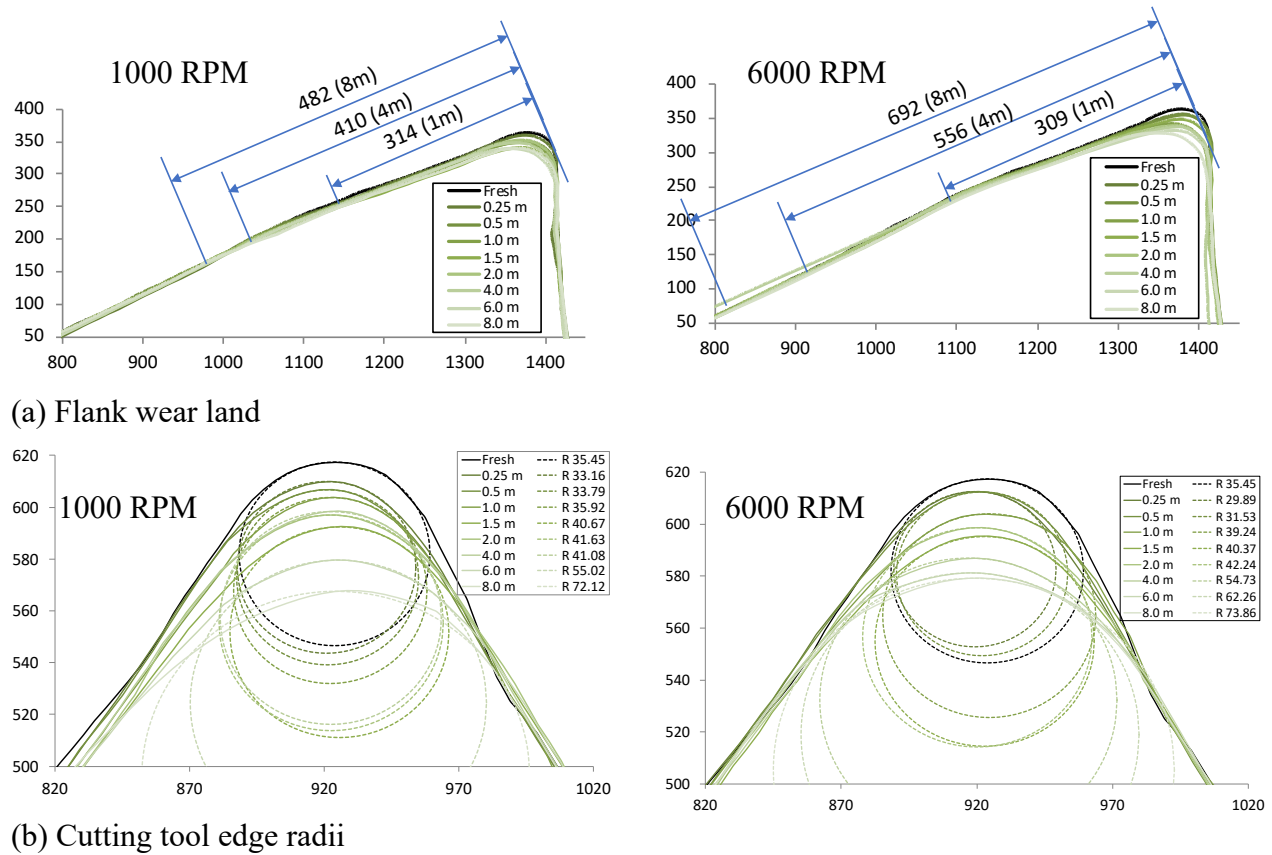
Figure 4.8. Tool wear for the 45° plies at cutting speeds of 1000 and 6000 RPM

The SEM images in Figure 4.9(a, e, c, and g) show the tool cutting edges after cutting the 45° plies for 1 m and 8 m at both spindle speed conditions. The cutting tools show significant edge rounding even after cutting 1 m as demonstrated on the high magnification (~9000x) SEM images showing sporadic scratches regardless of the spindle speed. Analyzing SEM images of the tool

Figure 4.9. Tool edge SEM images 1 and 8 m at the 45° plies (spindle speeds of 1000 and 6000 RPM) and their corresponding CFRP machined surfaces.

after cutting 8 m of CFRP, the scratches become much more evident which is shown in Figure 4.9(c). Typically, these scratches seem to originate from the pockets where the carbide grains were dislodged and the dislodged carbides scratched the flank surface. According to Ramulu *et al.*[152]

and Sheikh-Ahmad and Davim [153], the carbon fibers are fractured due to the compression-induced shear across the fiber axis and interfacial shearing. Observed on the machined surfaces in Figure 4.9(b, f, d and h), the fractured ends of the carbon fiber are typically sharp. These fractured fibers directly interact with the tool flank surface, exhibiting 2-body abrasion if the fibers are securely anchored into the rest of the laminates. This 2-body abrasion is experimentally supported by the average width (~10 μm) of the scoring marks on the flank surface correlating with the average distance of carbon fibers. This is the reason for the observed higher flank wear on 6000 rpm as the interaction between fibers and tool is mainly confined to the flank surface and multiplied by 6 times compared to the 1000 rpm case.

5.3 The 90° Plies

(a) Flank wear land

(b) Cutting tool edge radii
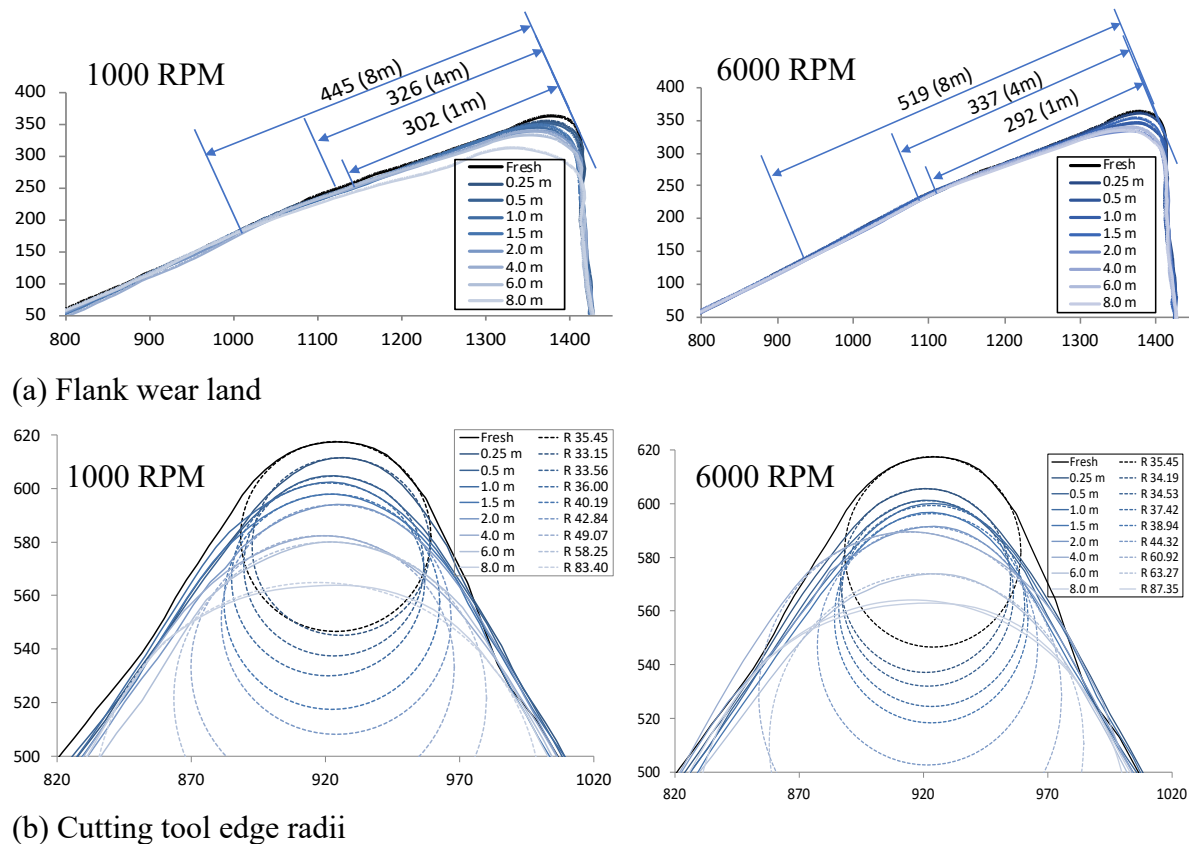
Figure 4.10. Tool wear for the 90° plies at cutting speeds of 1000 and 6000 RPM
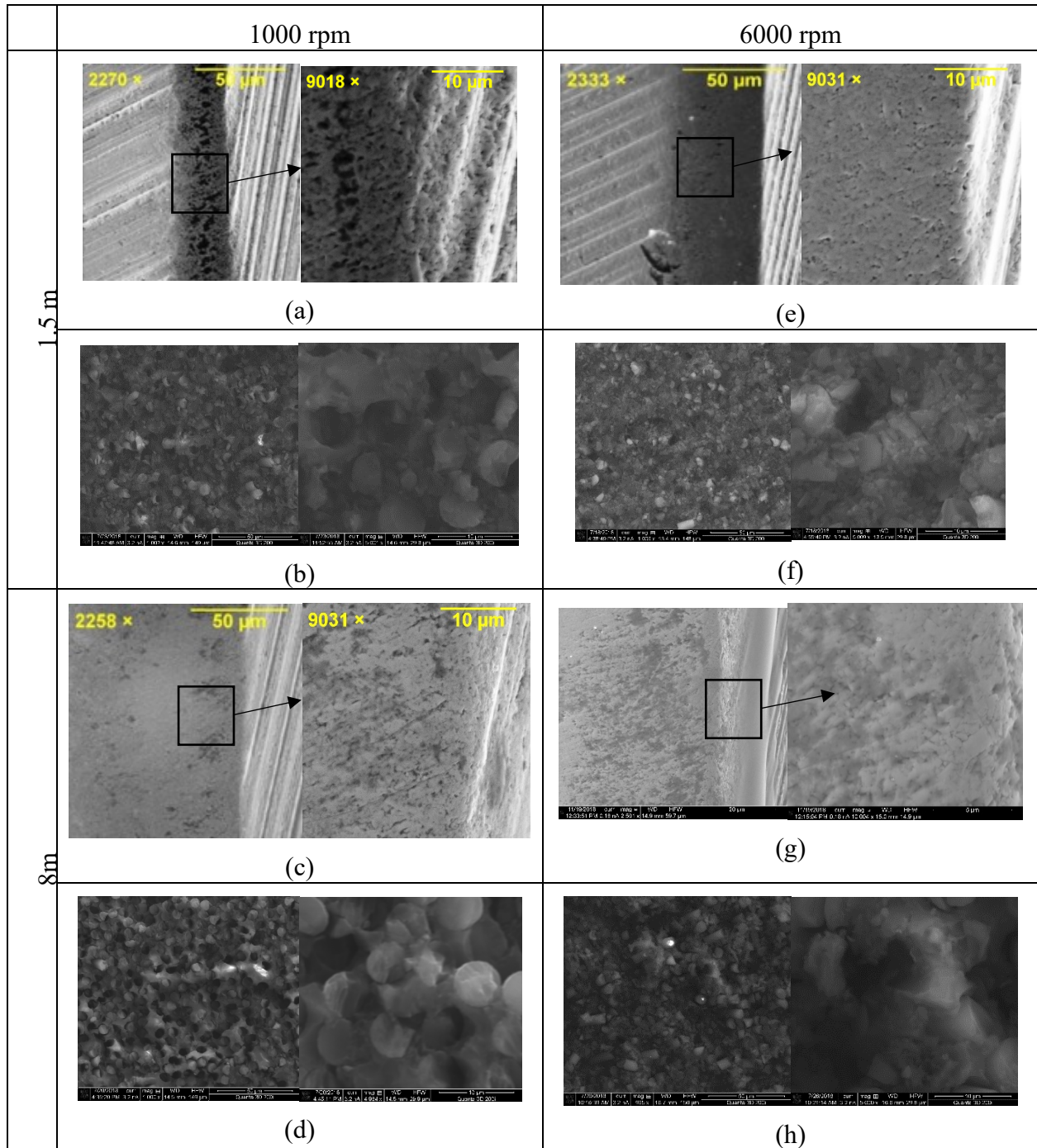
Figure 4.11. Tool edge SEM images 1 and 8 m at the 90° plies (spindle speeds of 1000 RPM and 6000 RPM) and their corresponding CFRP machined surfaces.

The flank wear measurement results for the 90° plies shown in Figures 4.10(a) and 4.14 indicate that the flank wear land increases most mildly among the four ply angles when cutting up

to 1 m regardless the spindle speed. After cutting 4m, the increase in the flank wear land is more significant at 6000 RPM compared to 1000 RPM. Not only the higher cutting speed condition results in greater edge radii but also the edge radius was most significantly increased with cutting distance, reaching the biggest radius among the four plies. Akin to the edge radii results, the worn tool area is affected by the spindle speed as this area is resultant from a combination of an increase in both flank wear and edge radii. In terms of the worn area and the edge radius, the 90° plies attained the most rate and reached the highest value with 6000rpm.

Figure 4.11 presents the SEM images of the cutting edges as well as the machined CFRP surfaces at cutting distances of 1 m and 8 m at both spindle speed conditions for the 90° plies. The chip formation mechanisms in the 90° fibers during orthogonal cutting are determined to be compression-induced shear fracture perpendicular to the fibers and inter-laminar shear fractures along the fiber matrix interface [152], [153]. These fractured carbon fibers classified as 'exposed' will make the tool edge dull (e.g.: increase in the edge radius). Multiple intermittent scratches on the machined surface, as shown on Figure 4.11(c and g), are observed after cutting 8 m of work material at both spindle speeds. However, these defects are not visible in the initial tool wear stage (cutting distance of 1.5 m). After edge-trimming the 90° fibers, a significant number of fibers are exposed at low and high-speed conditions. The total number of the exposed fibers increases with cutting distance, which is more than any other ply angles. Only with the $90°$ plies, the extent of the fibers pulled-out had increased as the cutting progresses. Further observation of the machined surface SEM images reveal carbon fiber debris that may contribute to 3-body abrasion [154].

5.4 The 135° plies

Three types of wear measurements for the 135° plies are presented in Figures 4.12, 4.14, 4.15 and 4.16. Flank wear land area steadily increases from a cutting distance of 1 to 8 m as shown in

Figure 4.18(a), even with a significant increase in flank wear after cutting 8 m at 6000 RPM. Figures 4.18 (b and c), the edge radii and worn area increase steadily as the cutting distance increases at both spindle speed conditions. Edge radius and worn tool area data from cutting at 6000 RPM continuously maintain a larger magnitude than any data point from cutting at 1000 RPM.

(a) Flank wear land

(b) Cutting tool edge radii
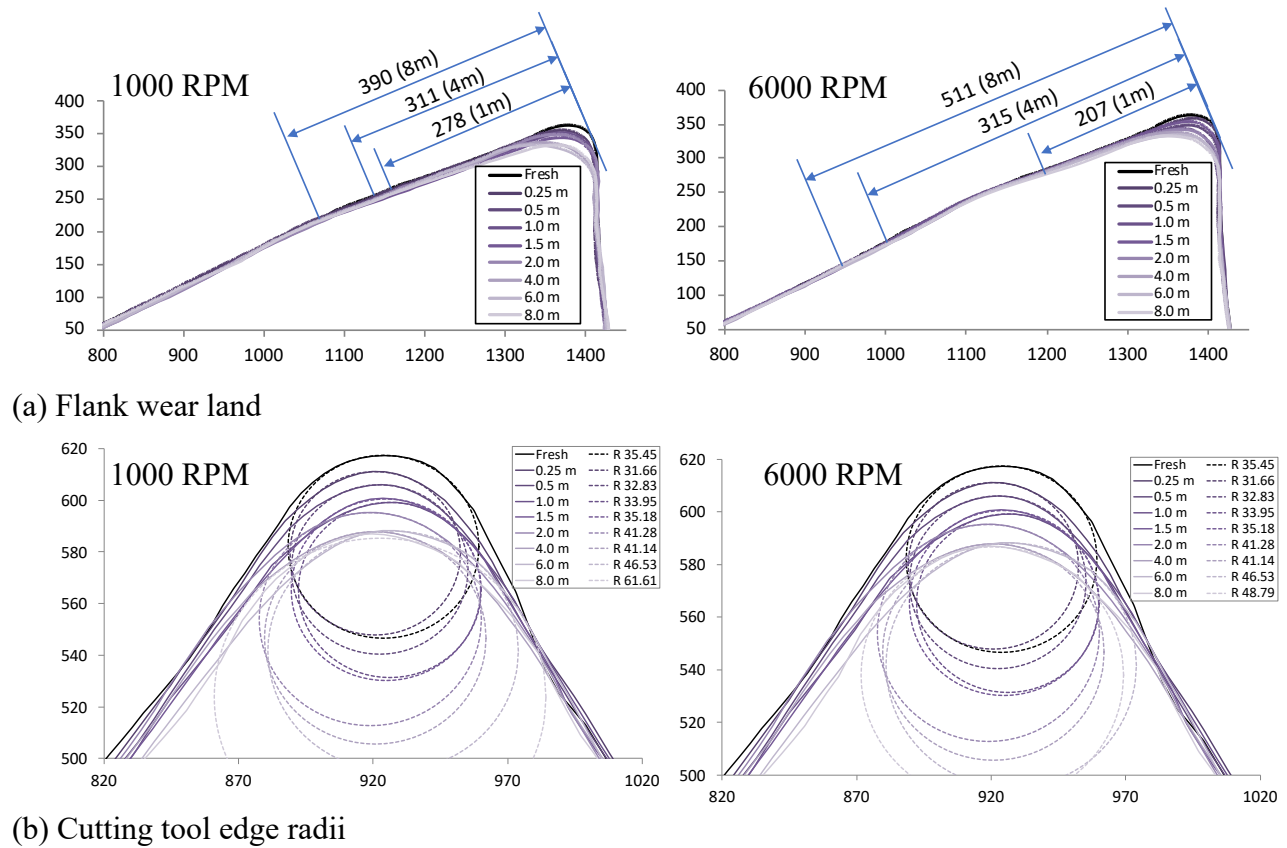
Figure 4.12. Tool wear for the 135° plies at cutting speeds of 1000 and 6000 RPM

Figure 4.13 presents the SEM images of worn cutting edges and machined surfaces of the 135° ply angle. For orthogonal cutting, the fiber cutting mechanism for this orientation can be characterized by burst type cutting. This scenario occurs where a group of fibers ahead of the cutting tool become bent and fracture beneath the surface. Deep valleys or pockets will remain on the machined surface and allows fibers to be pulled out because of the intermittent fractures. The
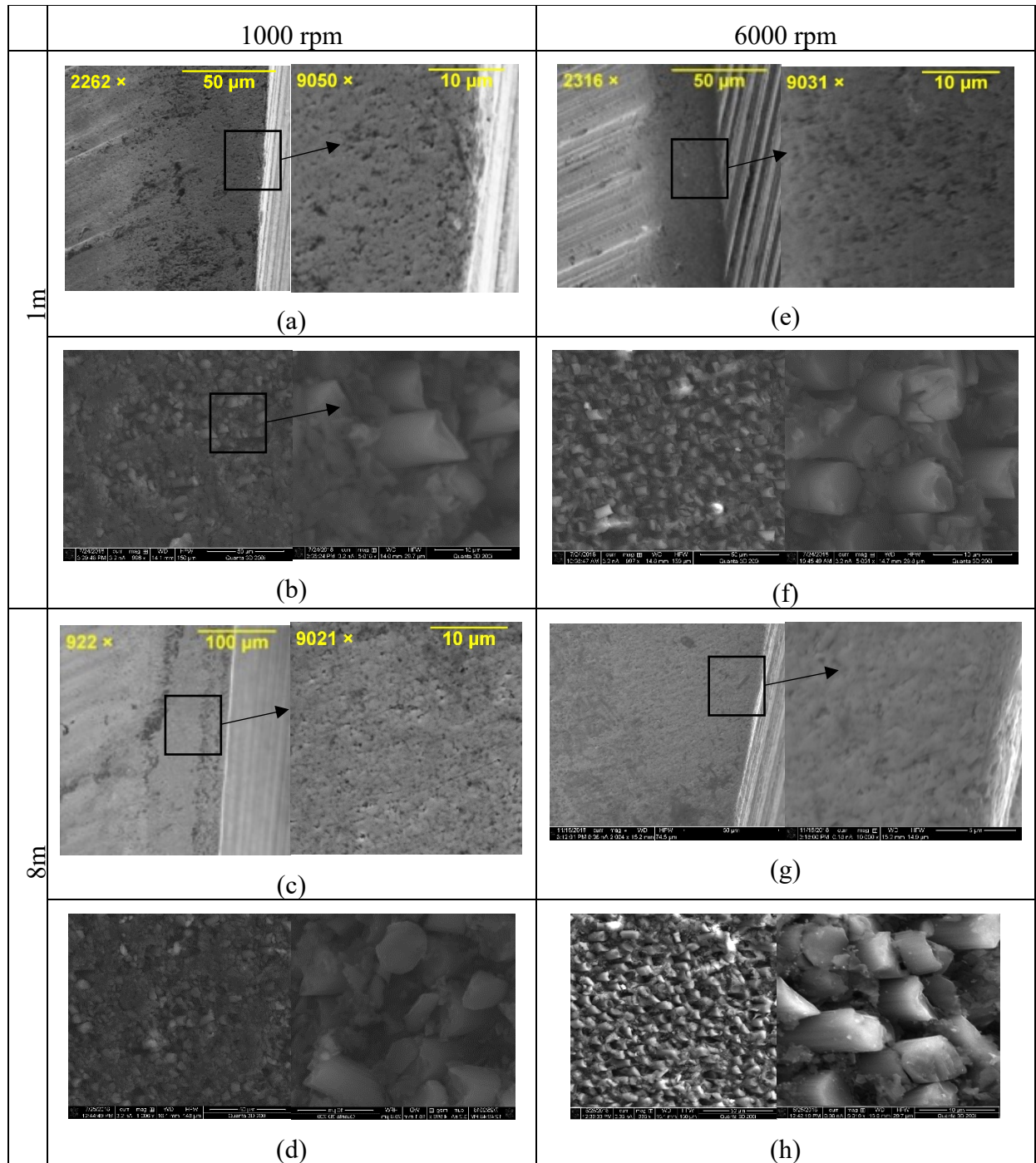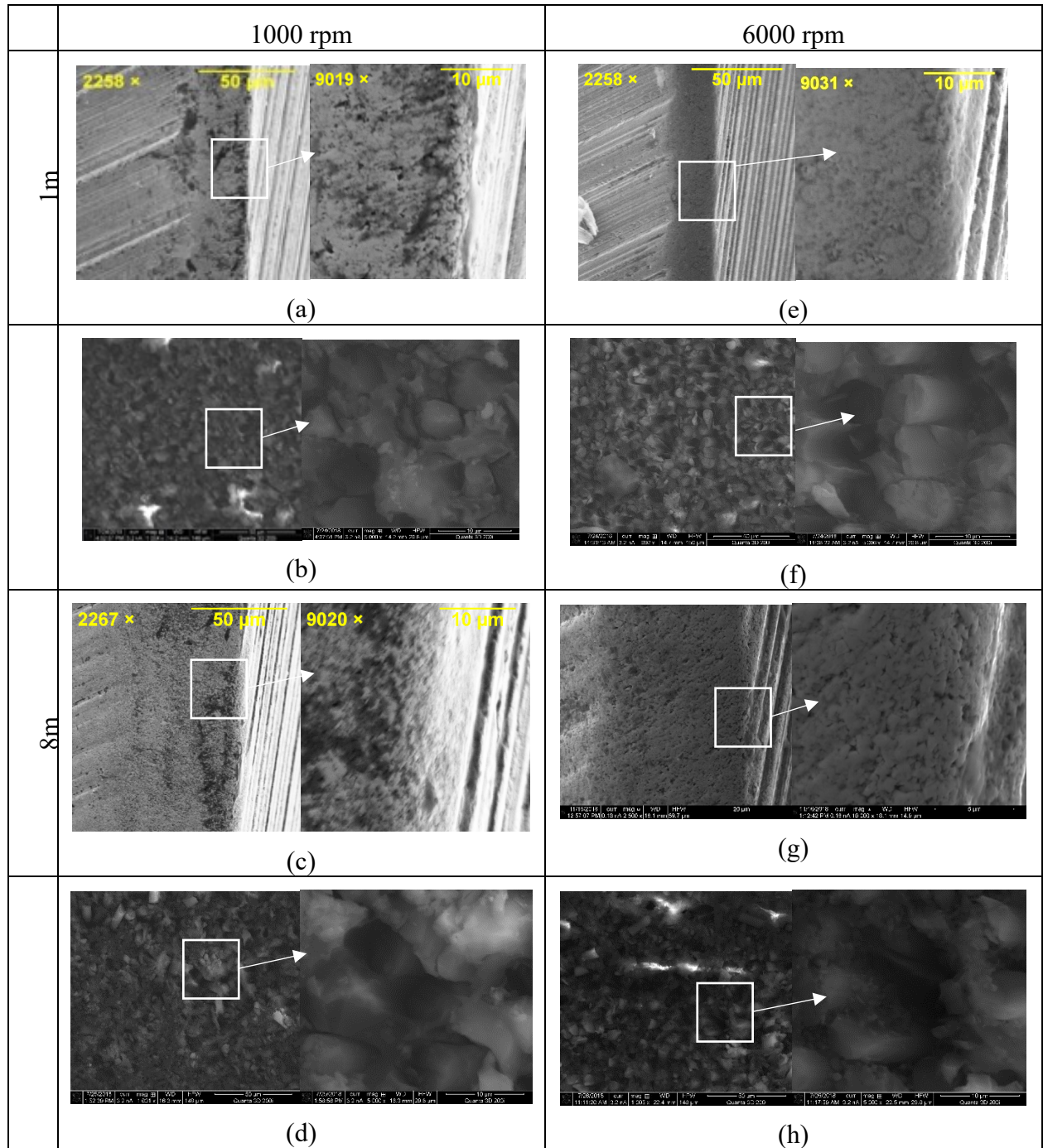
Figure 4.13. Tool edge SEM images 1 and 8 m at the 135° plies (spindle speeds of 1000 RPM and 6000 RPM) and their corresponding CFRP machined surfaces.

cutting edge will compress the plies and shear the fibers [152]. As shown on Figure 4.13 (a, c, e and g), the SEM images at the higher magnification (~9000x) show irregular patterns of scratches along the cutting direction at both initial (1 m) and steady state cutting distances (8 m) for 1000

and 6000 RPM. These irregular scratches can be related to the randomly located fibers exposed on the machined surface due to the bust type of chip formation. These fibers directly interacting with the flank side will cause 2-body abrasion as shown in Figure 4.13 (b, f, d, h) while the fiber debris may cause 3-body abrasion similar to the fiber-pull outs occurring on the 90° plies.

5.5 Analysis of the Tool Wear Progression
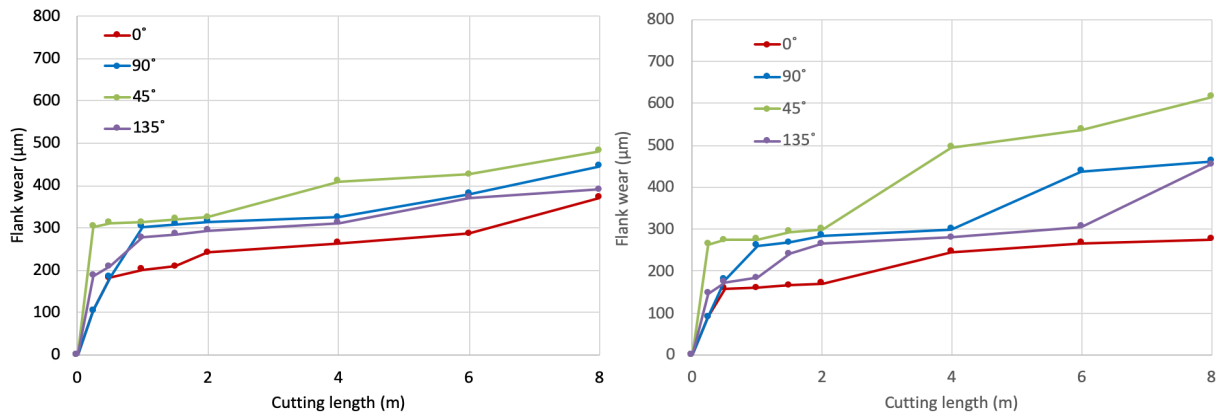
(a) Flank wear at 1000 rpm   (b) Flank wear at 6000 rpm

Figure 4.14. Flank wear progress for all ply angles at 1000 and 6000 RPM

In this section, a comparative analysis on tool wear measurements will be conducted for the four plies. Figure 4.14 presents the flank wear progression of both spindle speed conditions where an expeditious increase was observed in the initial cutting stage up to 0.5 m and a steady increase up to an 8 m cutting distance. The higher cutting speed generates greater flank wear lands for 45° and 90° plies. However, we cannot make the same claim for 0° and 135° plies. Flank wear was most severe when cutting the 45° plies. In general, the order of flank wear severity is as follows: 45, 90, 135, and 0° plies at both cutting speed conditions. Sakuma et al. [155, 156] provided a hypothesis that the fibers with orientation smaller than 45° may create the largest tool wear in turning glass fiber reinforced plastic (GFRP). While a few scholars found similar results, this was not studied in an extensive manner [81], [154-156]. This trend is closely related to the numerous

scratches observed on the flank surfaces, which are shown in Figure 4.11 (c and g). This implies 2-body abrasion by the direct interaction of the fractured carbon fibers and tool flank surface and the extent of the abrasion may be proportional to the number and length of exposed carbon fibers. In addition, the cutting tool experienced a bouncing-back phenomenon which is elastic-recovery of the fibers [70]. This phenomenon has a great impact on the extent of flank wear and may intensify abrasion on the flank surface. When cutting the 45° plies, the individual carbon fibers loaded in both shear and tensile normal stresses bounce back towards the tool flank surface by the shear load [70]. When trimming the 90° plies, the fibers were perpendicular to the cutting direction yielding a high number of exposed fibers, a possible cause of flank wear. However, the length of exposed fibers was relatively short. This implies that the shorter exposed fibers do not bounce back as much as that of the 45° plies. For the case of 135° plies, most fibers were either pulled out or covered by matrix smearing, which results in less tool flank wear as a substantially less number of fibers are expected to interact with the cutting tool surfaces. The 0° plies were cut along the fiber direction, which causes peeling or delamination, as depicted in Figure 4.8. Therefore, flank wear can be generated only by the sliding actions between the flank side and the ends of the broken fibers, resulting in minimal wear at the 0° orientation.

(a) Edge-rounding radius at 1000 rpm   (b) Edge-rounding radius at 6000 rpm
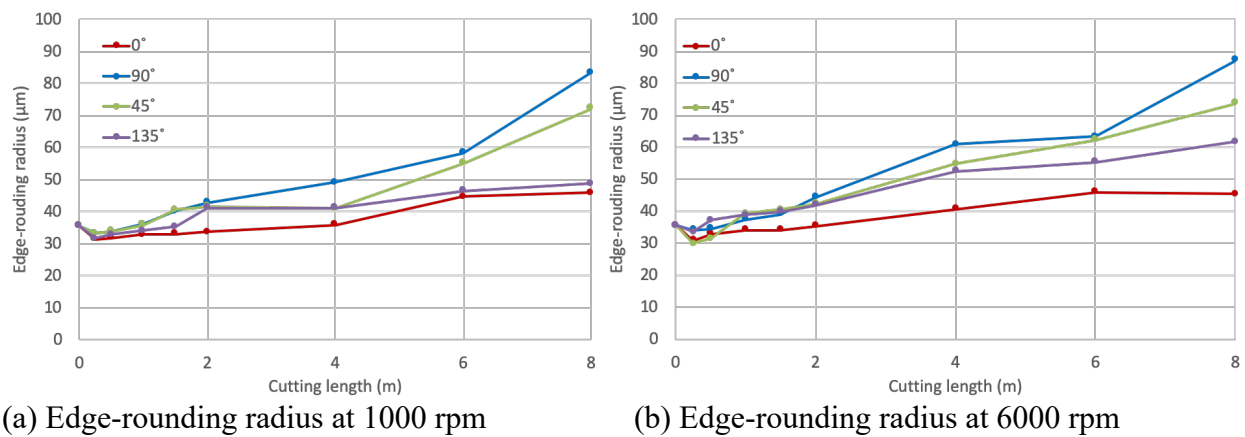
Figure 4.15. Comparison of the edge-rounding radius at 1000 and 6000 RPM

Figure 4.15 presents a comparison of the edge radius measurement for all plies at both spindle speeds after a cutting distance ranging from 1.5 m to 8 m. The trend of edge-rounding radius change is similar between the two cutting speed conditions. Initially, the radius of edge-rounding decreases slightly after cutting up to 0.25 m then increases steadily while cutting up to 8 m. This happens in order to conform to the condition at the cutting edge. Among the four plies, the edge-rounding radius increases the most with the 90° plies and least with the 0° plies. When cutting the 90° plies, chip formation was due to a series of in-plane shear fractures of CFRP by directly interacting with the cutting edge. For this reason, the highest cutting force was generated by the 90° plies [70]. Thus, the cutting edge is rounded most when cutting stiff and abrasive carbon fibers perpendicular to the cutting direction. During machining of the 45° plies, the chip formation did not result in a cutting force as high as the 90° plies as reported in [70]. However, the cutting edge will experience abrasion when interacting with the 45° fibers, which fail due to the compression-induced shear perpendicular to the fiber direction. For the 135° plies, the chip formation can be characterized by shear fracture along the fiber/matrix interface causing high deformation due to compressive loading [70]. This causes the burst type chip formation resulting in fiber pull-outs and further reduces direct interactions between the fibers and tool cutting edge. When machining the 0° plies, the carbon fibers will delaminate due to micro-buckling and only a few fibers will fracture perpendicular to the fiber orientation [151]. This type of chip formation minimizes cutting edge and carbon fiber interactions.

Figure 4.16 shows worn tool area measurements. The worn area refers to the results found by integrative wear measurement which includes mostly edge rounding and flank wear from 2D tool profiles. However, the amount of work area being affected by flank wear is very small. Thus, the worn area is more directly related to the edge radius. At both cutting speeds, the worn area rapidly

increases in the initial stage from 0 m to 2 m cutting distances before gradually increasing from 2 m to 8 m. For all distances, the largest worn tool area occurred at the 90° ply angle, followed by 45°, 135°, and 0°. This is similar to the results found during edge radius measurement.

(a) Worn area at 1000 rpm

(b) Worn area at 6000 rpm
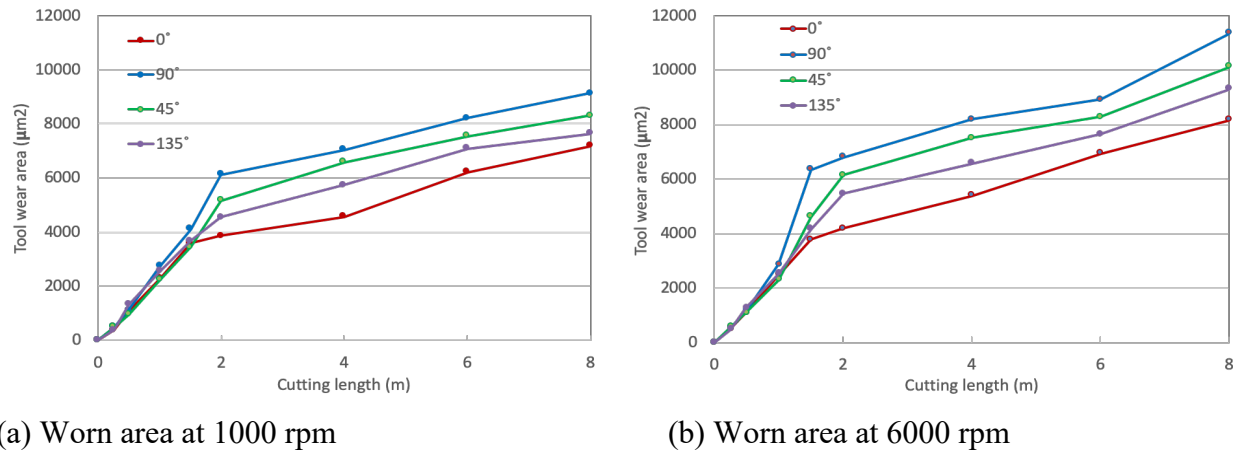
Figure 4.16. Comparison of the worn area for all ply angles between 1000 rpm and 6000 RPM

5.6 Analysis of the Machined CFRP Surfaces

The fibers exposed on the machined surface interacts with the cutting edges and impacts tool wear during the edge-trimming process. Therefore, SEM images of the machined surfaces of the 45°, 90°, and 135° plies were examined. Any further examination of the 0° plies is not necessary as the main chip formation mechanism is delamination where the interaction with the exposed fibers is minimal. Figure 4.17 presents the total numbers of the exposed fibers, fibers pulled-out, and fibers covered due to matrix smearing at various cutting conditions. These numbers are counted based on the classifications shown in Figure 4.5 on the SEM image area of 300 μm x 130 μm for each ply angle. With the plies made of 60% fiber volume fraction, approximately 500 fibers for the 45° and 135° plies and around 700 fibers in the 90° plies exist in the image area. The 90° orientation has the highest number of exposed fibers, ranging from 357 to 393, among all ply

angles and cutting conditions studied. The number of exposed fibers on the 45° plies ranges from 235 to 323 while that on the 135° plies shows the range of 97 to 255.

(a) 45° plies

(b) 90° plies

(c) 135° plies
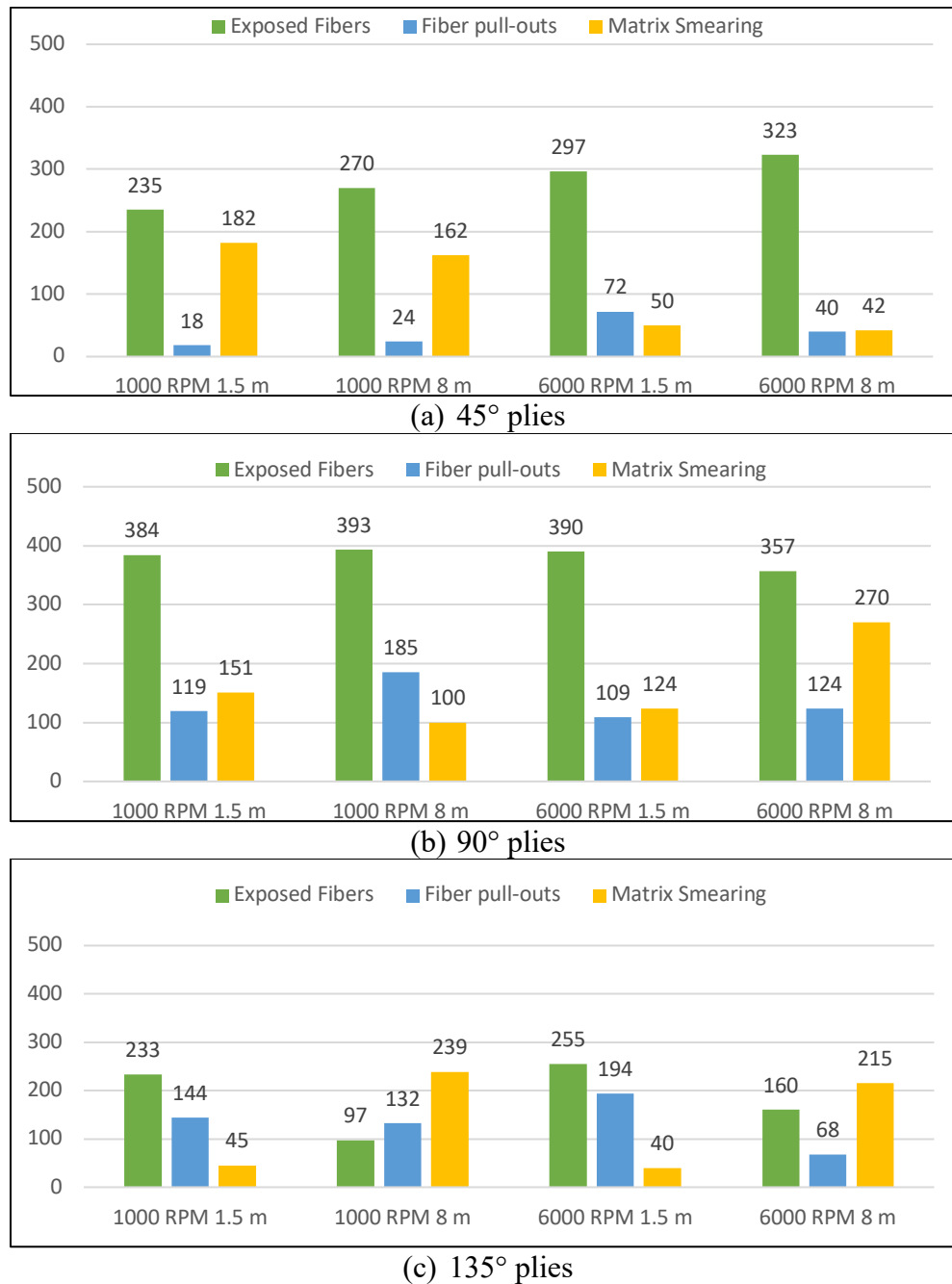
Figure 4.17. Numbers of exposed fibers, fibers pulled-out, and fibers covered under matrix smearing from SEM image in an sample area of 300 μm x 130 μm.

As mentioned in previous sections, the fractured edges of the exposed fibers contribute heavily to flank wear. The quantity of exposed fibers increases directly with cutting distance for both 45° and 90° plies regardless of spindle speed. These two ply angles also show larger flank wear and edge rounding than other ply angles that were observed.
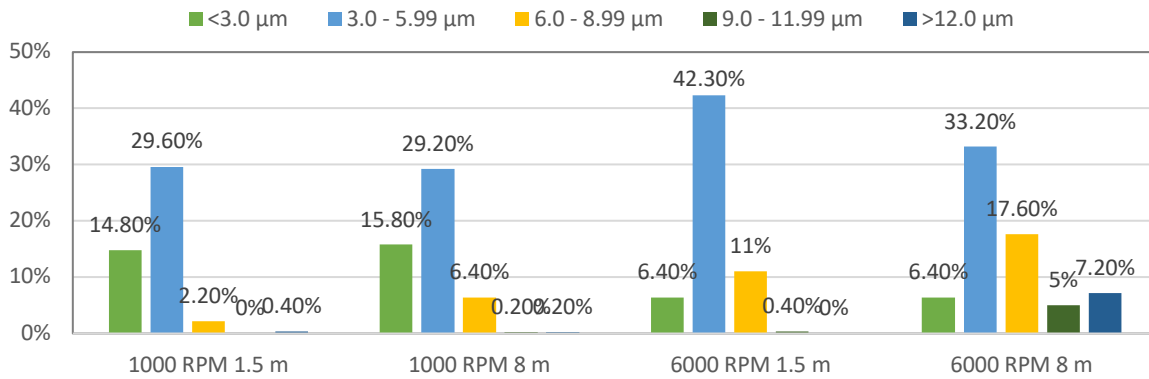
(a) 45° plies
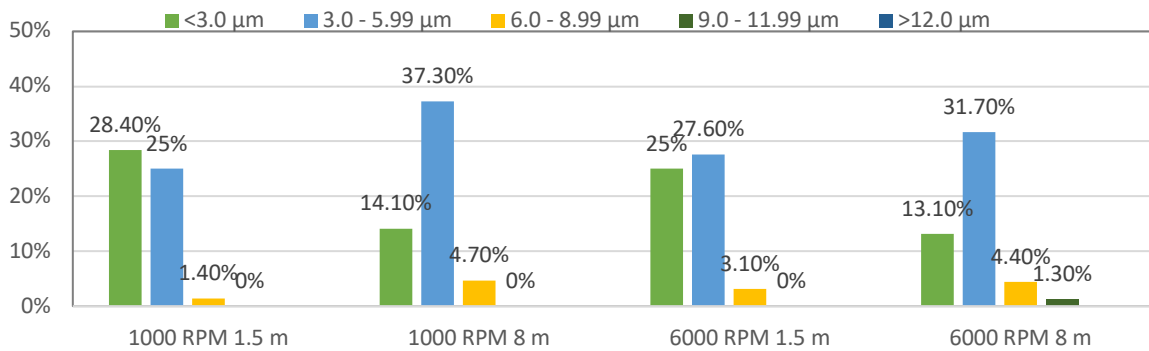
(b) 90° plies
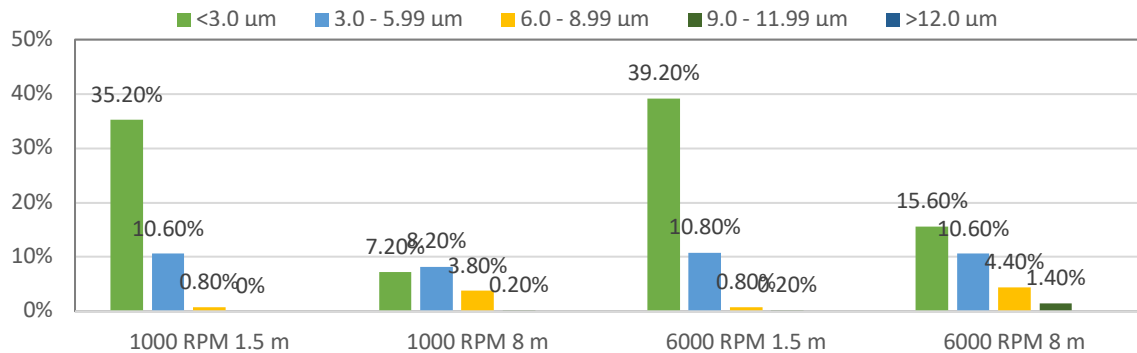
(c) 135° plies

Figure 4.18. Length Distribution of the exposed fibers perpendicular to cutting direction and its percentage in an sample area of 300 μm x 130 μm.

Another characteristic, the fiber pull-outs, was studied on the machined CFRP surface. Comparatively fewer number of fiber pull-outs are observed in the 45° plies while both 90° and 135° plies display significant numbers of the fiber pull-outs. The difference lies in the cutting mechanisms of the 45° plies consisting of tensile and shear loading on the fibers while both 90 and 135° plies leads to more fiber pull-outs. Cutting the 90° plies requires breaking the fibers indivisually and the high cutting force pulls out the fibers [150]. The 90° ply data shows that the fiber pull-outs increase with cutting distance regardless of the cutting speed, indicating that tool wear affects the fiber pull-out. Cutting the 135° plies promotes the matrix failures between fibers and, with the fiber-matrix debonding, the bundel of fibers can 'burst' open. Fiber pull-outs may lead matrix smearing due to the cavities formed when the fibers has been pulled out. From the data, matrix smearing was seen to increase with cutting distance for both 90 and 135° plies while tool wear on matrix smearing of the 45° plies was minimal. Matrix smearing at both the 90 and 135° plies was manifested most at an 8 m cutting distance and 6000 RPM spindle speed.

Of the three classifications used to describe the machined carbon fibers, the exposed fibers are the major contributing factor to tool wear. To further delve into the effect of the exposed fibers on tool wear, the distributions of the exposed fiber length perpendicular to the cutting direction are presented in Figure 4.18. The total number of exposed fibers is the largest when cutting the 90° plies. However, the amount of flank wear of the 90° plies is overall less than that of the 45° plies. Figure 4.18 shows that the most of the exposed fibers range from 0 μm to 6 μm after cutting the 90° plies. Although most fibers are exposed throughout the matrix, these are relatively short and did not contribute to flank wear significantly. For the 45° orientation, a high fraction of the exposed fibers longer than 6 μm are observed at an 8 m cutting distance. Approximately 29.8% of observable exposed fibers are longer than 6 μm at 6000 RPM after 8 m of CFRP was cut. The

flank wear data in Figure 4.14 also indicates a rapid increase in explosed fiber length beyond a 4 m cutting distance. It was noted that the longer exposed fibers (over 6 µm) contribute to 2-body abrasion on the tool flank surface.

6. Conclusion

These experiments aims to investigate the tool wear in the edge-trimming process (up-milling) of CFRP using four distinctly oriented plies of 0°, 90°, 45°, and 135° to examine the impact of fiber orientations on tool wear. The laser confocal microscope was used to quantitatively evaluate the flank wear land, edge radius, and worn tool area when edge trimming with eight different tool traveling distances of 0.25 m, 0.5 m, 1 m, 1.5 m, 2 m, 4 m, 6 m, and 8 m. Qualitative analysis was conducted using SEM images of the tool edges and machined CFRP surfaces. Some key discoveries that may be drawn from this study are:

- For the edge trimming process via up-milling of CFRP laminates, the cutting speed affects all wear characteristics such as flank wear, edge-radius rounding, and worn tool area regardless of the ply angle. However, the changes in wear behavior are not as significant compared to machining of metallic alloys.

- The 45° plies resulted in the most extensive flank wear while the 90° orientation yields the worst edge radius rounding and largest worn tool area. Contrastingly, the 0° ply angle has the least tool wear for all measurement types due to minimal interactions between carbon fibers and the cutting edge.

- In edge-trimming the 45° plies, the flank wear land increases rapidly up to 2 m and is followed by a steady increase up to 8 m. A larger number of exposed fibers has the length greater than 6 µm, which accerlerated the flank wear. This indicates the amount of exposed fibers and length of these perpendicular to the cutting direction directly impact the extent of flank wear.

94

- Cutting of the 90° fibers results a rapid increase in edge rounding observed in both spindle speed conditions. This large amount of edge rounding at the 90° orientation is related to extensive interactions between the carbon fibers and both rake and flank edges of the cutting tool.

- Edge-trimming of 135° fibers resulted in a high paced increase of flank wear and edge rounding radius up to 1m. This was followed by a steady increase up to 8m. Compared to the 45° and 90° fibers, 135° fibers created less tool wear because of an excessive presence of fibers pull-outs pertaining to far fewer tool face and carbon fiber interactions.

CHAPTER 5: TOOL WEAR ANALYSIS OF SUPERHARD CERAMIC COATED TOOLS IN DRILLING OF CFRP/TI STACK[†]

1. Overview of superhard coated tool wear in drilling of individual CFRP or Ti plates.

Our previous studies of drilling individual CFRP or Ti plate [157,158] were conducted experimentally to investigate the tool wear mechanisms of the superhard coated tools including $AlMgB_{14}$ (BAM), DLC, and (AlCrSi/Ti)N. One coating from the previous studies [157,158] was eliminated if the inferior performance was observed on each individual plate. For example, BAM coating [158], despite its superior performance in drilling Ti, was not selected for this study as it miserably failed in drilling CFRP. The selected drilling conditions were consistent with the conditions used in [157,158] with the WC-9%Co drill diameter of 9.525mm, which is the combination of 6000 rpm spindle speed and 0.0762mm/rev feed for CFRP plate, and the combination of 500 rpm spindle speed and 0.0508 mm/rev feed for Ti plate.

The experimental results [157] from drilling CFRP only indicated that the wear mode when drilling CFRP is edge rounding. The results on the uncoated and DLC and (AlCrSi/Ti)N–coated drills are summarized in Figure 5.1 after making 40 holes on CFRP plates. The 2D profiles on a consistent location were presented by extracting from the 3D profiles obtained from CLSM. The DLC coating prevented cutting edge rounding up to first 10 holes when compared with the uncoated tool. After 10 holes, DLC coating was completely removed from the cutting edges and margins, unable to provide the protection against edge rounding. The (AlCrSi/Ti)N coating outperformed any other drills used in the study. Coating removal at the cutting edge and margin, as well as edge rounding, is noticeable after drilling 20 to 40 holes, although it is significantly less

---

[†] This chapter was published at "Dinh Nguyen, Vadim Voznyuk, Mohammad Sayem Bin Abdullah, Dave Kim, Patrick Kwon, 2018. Tool wear of superhard ceramic coated tools in drilling of CFRP/Ti stacks., 2018, Proceedings of the 2019 ASME Manufacturing Science and Engineering Conference."

than the other drills. The reasons for the superior performance of (AlCrSi/Ti)N coating can be explained by its stiffness of the coating comparable to the substrate, the solid adhesion between coating and substrate, and the unique morphology (multilayered and thickness) of the coating [158].
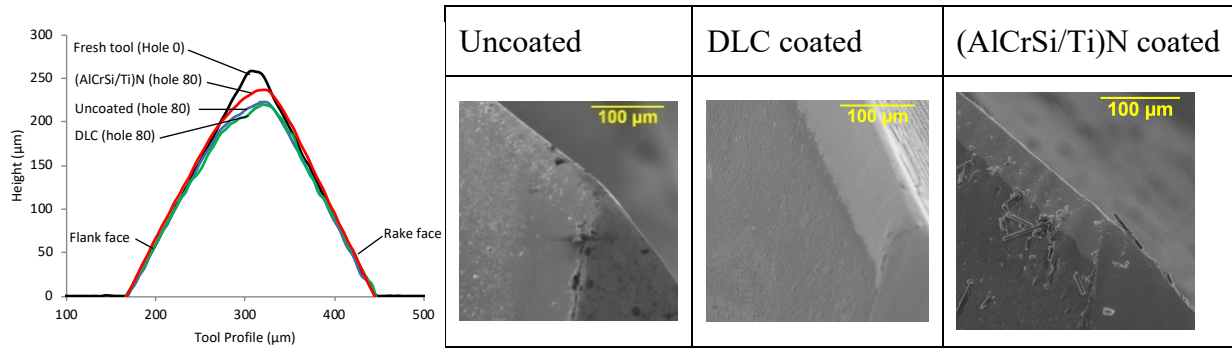
Figure 5.1. 2D Profiles from CLSM and SEM images of hole 80 for uncoated, DLC, and (AlCrSi/Ti)N coated WC drills when drilling CFRP only [157].

In our previous work [158], the individual Ti plates were drilled with uncoated, BAM, DLC, and (AlCrSi/Ti)N coated drills. The results on the uncoated and DLC and (AlCrSi/Ti)N – coated drills are summarized in Figure 5.2 after making 40 holes on Ti plates. The main wear mechanisms are micro-chipping and steady state flank wear. It is inferred that the attrition wear occurs when the adhesion detached the segments of cutting edge causing micro-chipping. At the same time, the 'hard' phases, which are the hard-orientation of alpha phase (hexagonal closed packed (HCP) crystalline phase) and the lamellar phase (a combination of alpha and beta phases) present in Ti alloys causes abrasive wear. The hardness of HCP is highly anisotropic with the hardness on the c-axis about 50% harder than any other direction [104]. Thus, in cutting the polycrystalline Ti work materials, the individual grains, whose 'hard' orientations are aligned along the flank surface, abrade and generate the flank wear. In addition, the lamellar phase, the 'hard' phase is constrained due to the complex lamellar microstructure and cause substantially more flank wear [159]. The

uncoated drill failed at hole 23 with extensive micro-chipping, while BAM coated drill made the holes up to 80 without any noticeable microchipping. The (AlCrSi/Ti)N coated drill also results in less Ti adhesion and minimal microchipping over the uncoated drill; however, it had major chipping at hole 58. The DLC coating with the reduced frictional coefficient mitigates Ti adhesion during the drilling process. However, the DLC coating was flaked off before making 40 holes as multiple micro-chippings (see Figure 5.2(b)) occurred on the cutting edges of DLC coated drill [158].
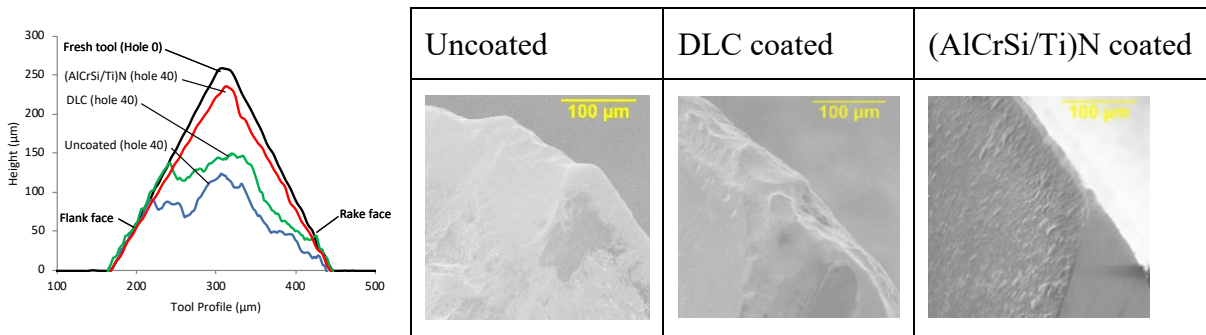
Figure 5.2. 2D Profiles from CLSM and SEM images of hole 40 for uncoated (fractured at hole 23), DLC, and (AlCrSi/Ti)N coated WC drills when drilling Ti only (Ti adhesion was removed.) [158].

2. Experimental Procedures

2.1. Workpiece Material

The CFRP-Ti stack used in the experiment were composed of a CFRP plate (top) and a Ti plate (bottom), as depicted in Figure 5.3. The Ti plate used in the experiment was Ti-6Al-4V made to a thickness of 6.73mm with a hardness of 400Hv. The CFRP plates used in the experiment were quasi-isotropic laminates with the layups of $[(0/45/90/-45)_4/90/0_2/0]_s$ made of graphite fibers in an epoxy matrix. The CFRP laminate had a thickness of 7.54 mm with an average ply thickness of 0.189 mm. The average diameter of the carbon fiber is 5 μm. The hardness of carbon fibers used

in this experiment is reported to be between 0.8-1.1GPa [160, 161]. The stack material was provided by the Boeing Company (Seattle, WA).

2.2. Cutting Tools

Uncoated, DLC coated, and (AlCrSi/Ti)N coated WC-9% Co drills were used in this investigation. The base uncoated carbide drills were manufactured by Precorp Inc. (Spanish Fork, UT) and were made to premium Ultra-Grain® (submicron grain size) with a SmoothGrind® finish specifications. Both DLC and (AlCrSi/Ti)N coatings were prepared by Fraunhofer USA Center for Coatings and Diamond Technologies (CCD) (East Lansing, MI) as mentioned earlier. The proprietary processing technology has been developed by Fraunhofer USA CCD to increase the thickness of (AlCrSi/Ti)N coating to 7.3 m, which was found to improve the machinability on CFRP [157]. This new coating is twice the thickness of the coating used in [158], which together with (AlCrSi/Ti)N coating did not perform as well as uncoated drills when drilling CFRP only, Ti only and CFRP/Ti stack [88]. The processing technology for thicker DLC could not be developed. The uncoated and coated drills have the same drill geometry with an outside diameter of 9.525 mm and flute length of 38.1 mm. The shank diameter was 9.525 mm and the overall length was 88.9 mm. The drills had a standard configuration with two flutes with a helix angle of 25 degrees and a right-hand spiral, right-hand cut (RHS/RHC). The drill point angle was 135 degrees.

2.3. Drilling Experiments

Drilling experiments of CFRP-Ti stack were carried out on a 3-axis CNC vertical mill (MiniMill, HAAS, Oxnard, CA, USA). The experimental setup is shown in Figure 5.3. A pre-drilled backing plate was put underneath the work material. This backing plate had 1.27cm holes in a pattern that matched the holes to be drilled in the work material. CFRP and Ti plates were mechanically fastened to the fixture to form a stack. The stack material with the packing plate is

mounted in a combined force & torque dynamometer so that the forces generated during drilling could be measured. The measured thrust and torque forces were transmitted to signal amplifiers, then to an A/D board (NI USB-6251, National Instruments, Austin, TX, USA), then recorded on a personal computer using data acquisition software (LabView 7.1, National Instruments, Austin, TX, USA).
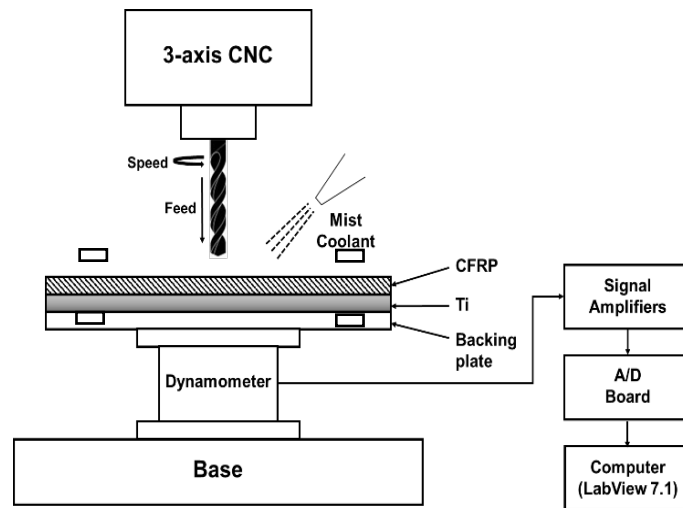
Figure 5.3. Experimental drilling setup and CNC equipment used for drilling

The drilling condition was fixed for all types of drills. When drilling the top CFRP layer, a spindle speed of 6000 rpm and a feed rate of 0.0762mm/rev were used. The drilling condition was changed during the drilling process from those of CFRP to Ti just prior to entering the Ti layer. For the bottom Ti layer, the combination of a 500 rpm and 0.0508mm/rev was used. These conditions represent the typical conditions used in aerospace industries. A water-soluble mist coolant was applied to the stack workpiece during the entire process at a constant flow rate averaging 16mL/min. The drilling experiments were conducted while sporadically stopping to observe the tool wear until critical failure of the drills occurred.

2.4. Tool Wear Evaluation & Measurement

A number of instruments and techniques were employed to measure tool wear. A scanning electron microscope/energy dispersive x-ray spectroscopy (SEM/EDX, ASPEX PSEM-75, FEI Co. Delmont, PA, USA) was used to provide high-magnification images of the wear pattern and to analyze the elemental distribution of the tool. The SEM was operated at 25kV and 24.5 mA of power. SEM images and confocal laser scanning microscopic (CLSM) profiles were taken before the experiment (0 holes), after making 5 holes, 10 holes, and then after every 20 holes. A confocal microscope (Fluoview FV1000, Olympus, Center Valley, PA, USA) provided a quantitative tool wear profile of the worn cutting edges at a consistent location, 300 μm from the margin for each drill. Wavelet filtering was used to eliminate the noise and artifacts inherent with the height encoded image obtained by confocal microscopy [162, 163].

3. Results and discussion

3.1. Dynamometer measurement

Figure 5.4 presents the maximum thrust force and torque data from the dynamometer in the CFRP cutting region and the Ti cutting region for the three drills. Drilling of the top CFRP plate results in much less thrust force and torque when compared with the bottom Ti plate drilling despite of much higher spindle speed and feed for CFRP. Maximum thrust force ranges from 241.6 N to 964.3 N when drilling CFRP while that of Ti ranges from 1222.6 N to 3163.5 N. The difference in maximum torque is more significant. Maximum torque values when cutting CFRP range from 501.6 N-mm to 1433.6 N-mm, while drilling of the bottom Ti plate results in the range from 3906.5 N-mm to 6988.1 N-mm. Similar to the data reported in [88], the maximum thrust force and torque increase with increasing hole number for both CFRP and Ti. A steady increasing trend is apparent with the (AlCrSi/Ti)N coated drill when the uncoated and DLC coated drills show relatively

101

irregular patterns. This may be due to the edge chippings on the two drills. The maximum thrust and torque of the uncoated drill become unsteady after making 20 holes, while those by the DLC coated drill become unsteady after hole 10. These results corroborate with the fact that the uncoated drill was chipped after hole 20 and the coating on the DLC drill was removed even before hole 5. Therefore, the fractured and sharp cutting edges of the uncoated and DLC coated drills resulted in irregular force magnitudes.
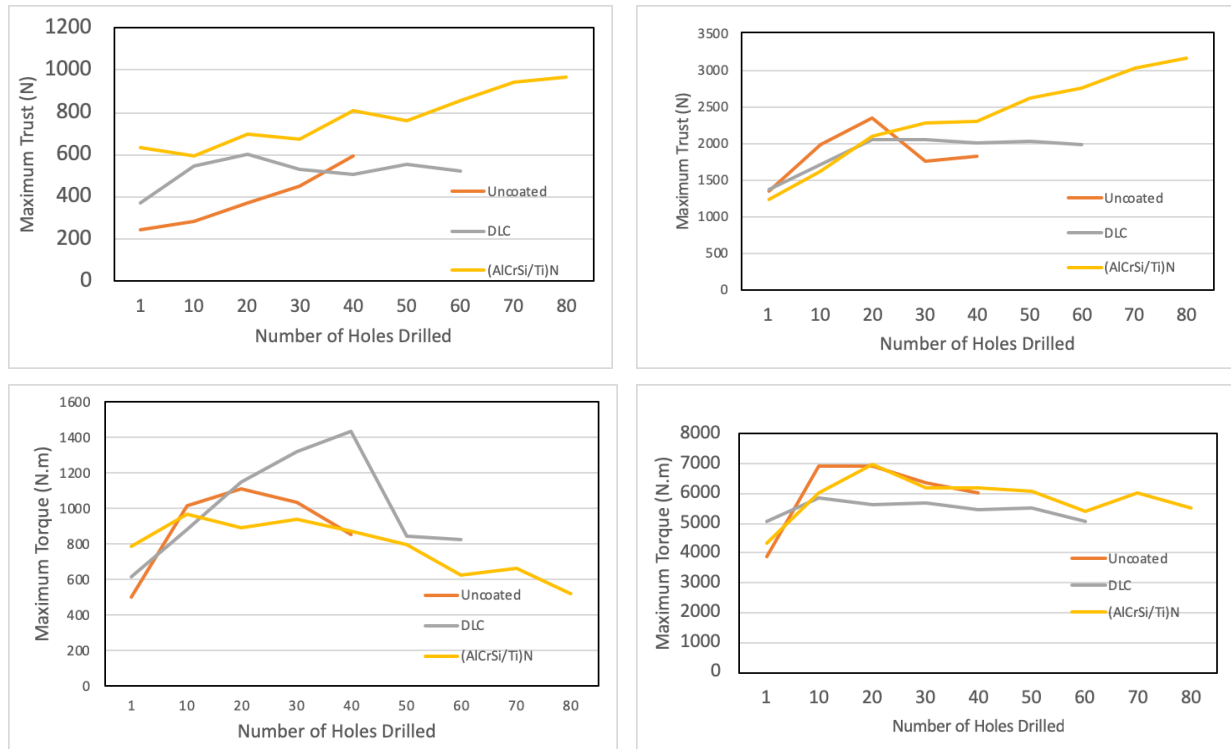
(a) drilling the top CFRP   (b) drilling the bottom Ti

Figure 5.4. Summary of Maximum Trust Forces and Torques

3.2. SEM images

Figure 5.5 shows the SEM images of the cutting edges of the uncoated, DLC and (AlCrSi/Ti)N coated drills starting from the fresh drills in the experiments. The images taken after the experiment showed that extensive Ti adhesion is evident at the cutting edge near the margin for all tools.

Overall, Ti adhesion is more evident as more holes are made with the evidence of more irregular cutting edge and coating removal. Large irregular Ti adhesion is observed when chipping at the cutting edge occurs, seen after making 60 holes in the DLC coated drill and 40 holes in the uncoated drill.
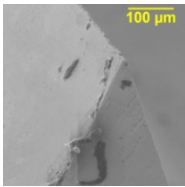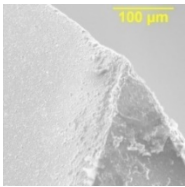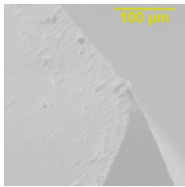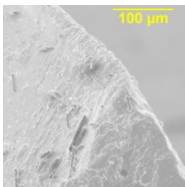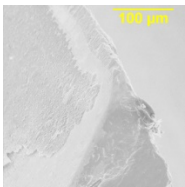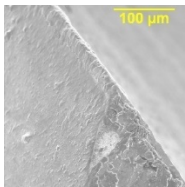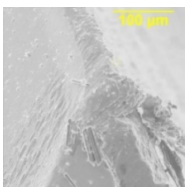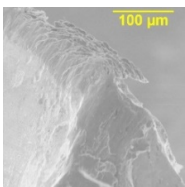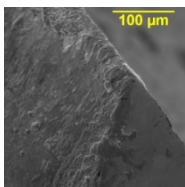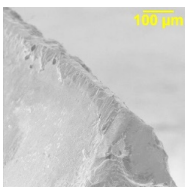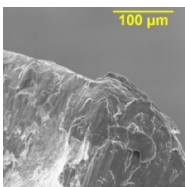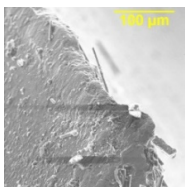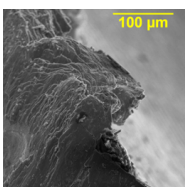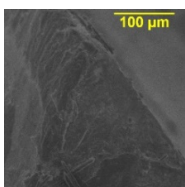
	Uncoated	DLC	(AlCrSi/Ti)N
Hole 0 (fresh)			
Hole 10			
Hole 20			
Hole 40			
Hole 60	Not applicable		Failed to taken
Hole 80	Not applicable	Not applicable	

Figure 5.5. SEM Images for uncoated, DLC and (AlCrSi/Ti)N coated with Ti-adhesion in CFRP-Ti Stack drilling.
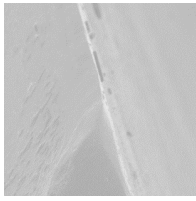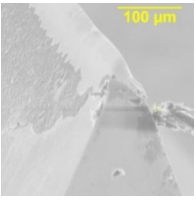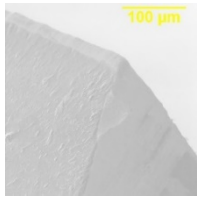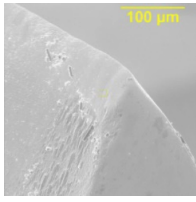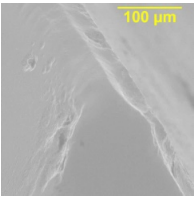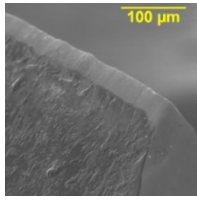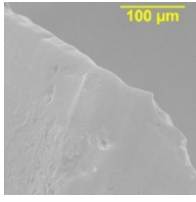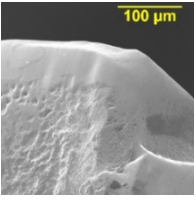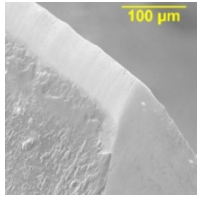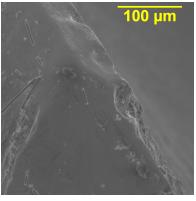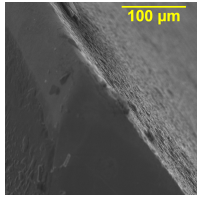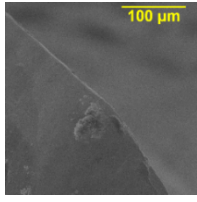
	Uncoated	DLC	(AlCrSi/Ti)N
Hole 10			
Hole 20			
Hole 40			
Hole 60	Not applicable		
Hole 80	Not applicable	Not applicable	

Figure 5.6. SEM Images for uncoated, DLC and (AlCrSi/Ti)N coated WC without Ti-adhesion in CFRP-Ti Stack drilling.

Figure 5.6 presents the SEM images of the same drill bits after drilling the top CFRP layer only. When comparing Figures 5.4 and 5.5, Ti adhesion present from the last hole is removed mechanically when drilling CFRP. Since the stack is configured with CFRP at the top and Ti at the bottom, the Ti adhesion generated when penetrating the bottom Ti plate is removed by the top CFRP when drilling the next hole, which increased the overall tool life [88]. In Figure 5.5, the

SEM images depict the removal of the coatings and the tool chipping as Ti adhesion is not present on the tools. The uncoated drill experienced major facture at hole 41. For the DLC coated tool, the coating is removed at both the cutting edge and the margin even in hole 10. The DLC coated drill had a major facture at hole 60, which resulted in extensive Ti adhesion on the cutting edge. Unlike DLC coated tool, (AlCrSi/Ti)N coated tool showed that the coating is intact (approximately 100 μm from the cutting edge) with no signs of major chippings up to hole 80.

In order to verify the removal of coating and to confirm the presence of Ti adhesion in drilling of the stack, SEM/EDX was performed at many locations along the cutting edge of the coated drills after making 5 holes. In Figure 5.7.a, a summary of the EDX results is shown for the DLC coating. Significant Ti adhesion is both along the cutting edge at location D and margin at location E shown on Figure 5.7.a. In contrast, almost no Ti adhesion is observed at location C, nor does there appear to be a protective coating. Further down near the trailing edge of the flank face from the cutting edge, the coating remains intact.

The (AlCrSi/Ti)N coated tool was evaluated after making 10 holes and every 20 holes thereafter. Figure 5.7.b presents the SEM/EDX results of the drill edge after making 40 holes and removing the Ti adhesion layer. In contrast to the coating performance of the DLC coated drill after making 5 holes (Figure 5.7.a), Al signals presented at the cutting edge indicates that the (AlCrSi/Ti)N coating is intact despite of being damaged extensively by edge rounding. The (AlCrSi/Ti)N coating was present on the drill after making 40 holes. The presence of tungsten (W) peaks from the tool substrate appears at the margin, C, indicating that the coating has been removed. Additional scans of the rake face indicate only the presence of hard-coating elements is noticeable without any visible wear. The EDX results of the drill after making 80 holes indicates

the Al & Cr signals are completely gone at the edge round region, indicating that the coating is completely worn off at the cutting edge.

(a) DLC after making 5 holes
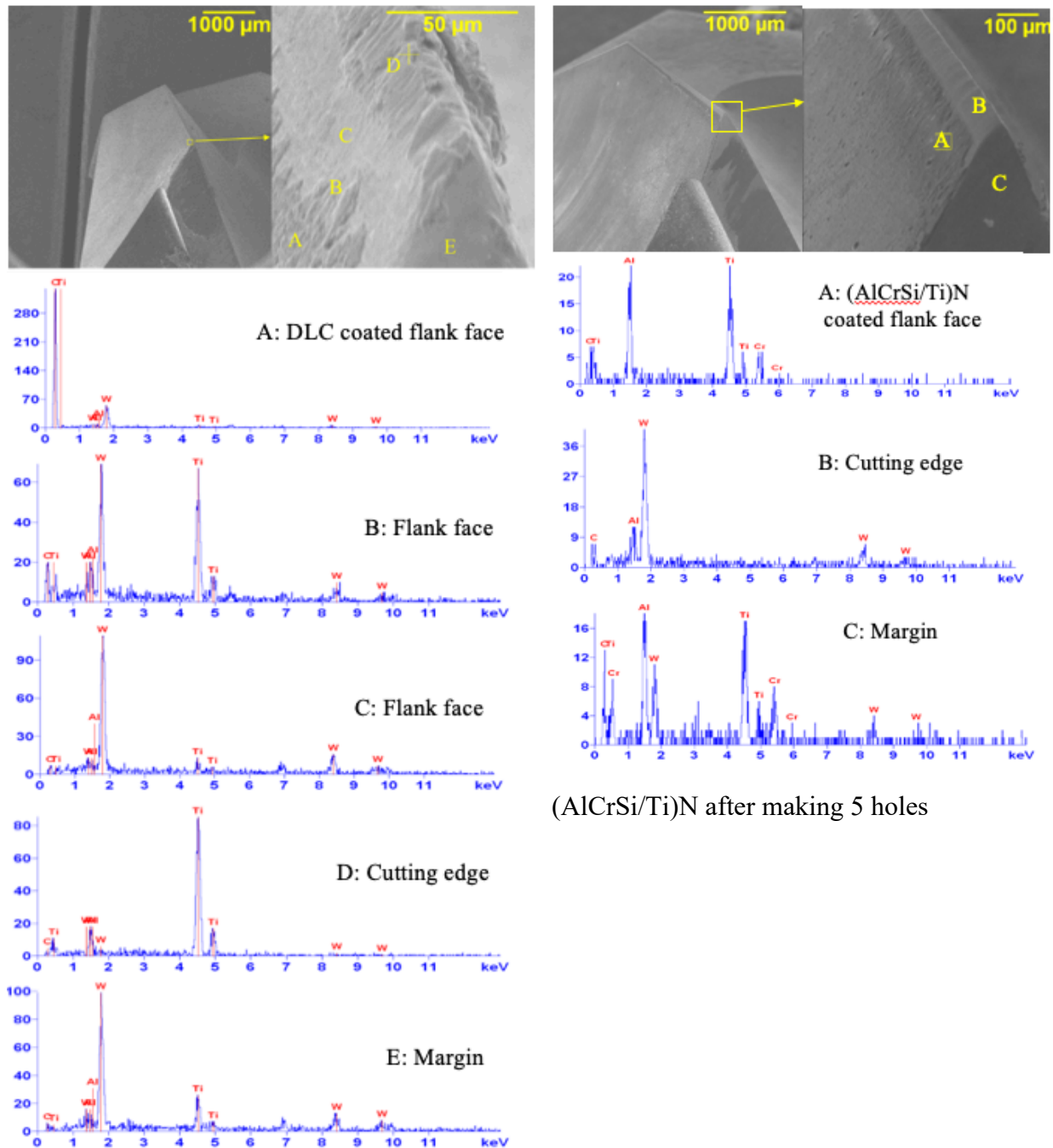
(AlCrSi/Ti)N after making 5 holes

Figure 5.7. EDX Summary of drill tool & coating composition

Surprisingly, the performance of this (AlCrSi/Ti)N coating with the thickness of 7.3 m as investigated by SEM and SEM/EDX evaluation is starkly different than those of the uncoated and DLC coated drills in this study and the thinner (AlCrSi/Ti)N coated drill (the coating thickness of approximately 3 μm) used to drill the stack in [88]. Only after making 40 holes, edge rounding of the (AlCrSi/Ti)N coated drills started to be noticeable practically without chipping and coating removal along the cutting edge. In contrast, the uncoated and DLC coated drills showed clear chipping at the cutting edge, extensive damage from Ti adhesion, and rounding of the cutting edge, providing no significant protection nearly from the beginning of drilling experiments. Based on the SEM observations, these phenomena occurred similarly in both the uncoated and DLC drills after making 10 holes, indicating the ineffectiveness of the uncoated and DLC coated drills.

3.3. CLSM results

The 2D cutting edge profiles of uncoated, DLC, and (AlCrSi/Ti)N coated carbide drills after drilling in CFRP-Ti stack at 10, 20, 40, 60, 80 holes extracted from 3D profiles from CLSM are illustrated in Figure 5.8. The CLSM technique was applied to quantitatively measure the tool wear with 20x of magnification in the stack mode. Some early measurements of these drills had the double-peaks in the profiles due to the saturated laser intensity on the top plateau of the edge-rounding [88, 95]. To distinguish these data, the dashed line was used on the profiles shown in Figure 5.8. The profiles of the uncoated drill indicate rapid edge wear until making 20 holes. After making 20 holes, the gradual edge rounding is followed by the chippings on the cutting edge evident by the profile of the drill after making 40 holes shown in Figure 5.8(a). The uncoated drill was completely fractured while making the 41st hole.

The DLC coating has steadily worn down while making 10 holes and showed major change in the cutting edge after 10 holes as shown in Figure 5.8(b). The drill may have undergone multiple
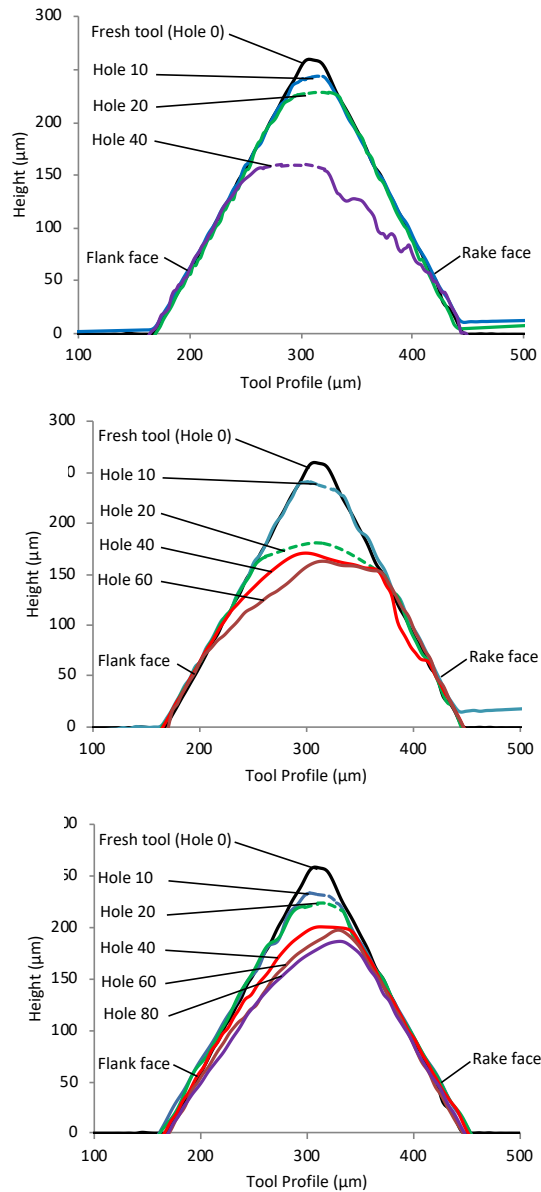
Figure 5.8. 2D profiles of the cutting edges of (a) Uncoated, (b) DLC coated, and (c) (AlCrSi/Ti)N coated WC drills from hole 0 to hole 80 in CFRP/Ti stack drilling.

micro-chippings between 10 and 20 holes. Between hole 20 and hole 60, the tool shows more gradual wear before experiencing gross fracture after making 60 holes. For the (AlCrSi/Ti)N coated drills, the cutting edge was well protected beyond making 80 holes as shown in Figure 5.8(c). No chipping in both micro- and macro-scales was observed. The profiles indicate the mixture of two main wear modes, edge rounding, the dominant wear mode of CFRP and flank

wear, the dominant wear mode of Ti64. However, the edge rounding is dominant on the drill while making the first 20 holes and the flank wear become more dominant after making 20 holes. This trend is also evident with the DLC coated drill.

4. Discussion
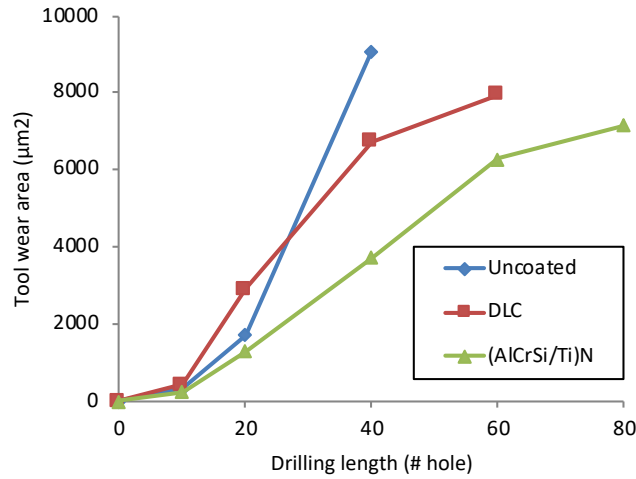
Figure 5.9. Tool wear area calculated based on the profile at 300-micron from the margin of the drills in CFRP-Ti drilling.

To quantitatively capture the wear profiles, the total wear area is used for the study. The tool wear area, which can be multiplied by a unit distance along the cutting edge. to converted to wear volume, is generated by subtracting the profile of a worn drill from that of a fresh drill for each of the drills after making certain numbers of holes. The results are presented in Figure 5.9. For example, the total wear area of the uncoated drill increases from 326 μm^2 to 1712 μm^2 between hole 10 and hole 20. The uncoated drill experienced major chipping after hole 20 which shows the largest wear area presented at hole 40. For the DLC coating at 10 holes, the worn area was 435 μm^2 and at 20 holes it is 2910 μm^2. Edge chipping occurred between hole 10 and hole 20 contributes a rapid increase in tool wear area. Then, the tool wear of the DLC coating increases gradually up to hole 60. The wear areas of the (AlCrSi/Ti)N coating are 236 and 1299 μm^2 at hole

10 and hole 20, respectively. The (AlCrSi/Ti)N coated tool shows the least amount of wear with a gradual increase up to hole 60.

In the series studies of superhard coatings in the drilling process of CFRP only [157] and Ti only [158] and the CFRP-Ti stack in [88] and this study, the thicker (AlCrSi/Ti)N coated drill outperformed any other coatings used. For CFRP only [157], the tool wear area of the (AlCrSi/Ti)N coated drills in the drilling process up to 120 holes showed less wear than the DLC coated drill. For the drilling experiments with Ti only [158], the (AlCrSi/Ti)N coated drill does not show any edge chipping up to hole 40, while the DLC coated drill has chipping before making 20 holes. Obviously, in drilling CFRP-Ti stack, the (AlCrSi/Ti)N coated drills were outstanding making up 80 holes without any noticeable damage. Beside the thickness, there are few unique features of the (AlCrSi/Ti)N coating. One feature is the multilayers and the other is the alternating layers between TiN layer and the composites layer of AlCrN and Si_3N_4.

Compared to the results presented in [88] where the thinner (AlCrSi/Ti)N coated drills did not performed well, the thicker (AlCrSi/Ti)N coated drills used in this study outperformed any other drills. The main difference is the thickness of the coating, 7.3 m in this study and 3 m in [88]. It turns out that the thickness of the coating directly impacts the performance of the coating. A similar conclusion was made with the CVD diamond coated tool in machining CFRP [106] as well as with (AlCrSi/Ti)N coated drill in drilling CFRP [157]. These works provided the importance of attaining thicker coating on our drills. However, the thickness cannot be increased on any coating. In addition to the CVD diamond coating, the processing of (AlCrSi/Ti)N coating allows the coating to be deposit to 7.3 m thick and, unlike CVD diamond coating, (AlCrSi/Ti)N coating works well in drilling Ti alloys.

5. Conclusion

Our experiments presented a preliminary tool wear study of the drilling process on CFRP-Ti stacks. To understand the fundamental wear mechanism, drilling experiments of the stack were conducted. Uncoated, DLC-coated, and (AlCrSi/Ti)N coated tungsten-carbide tools were used in the experiments. With regards to tool wear in stack drilling, the main points that may be drawn from this study are:

- The uncoated and DLC coated tools experienced major chipping at hole 41 and hole 60, respectively, while (AlCrSi/Ti)N coated tool could generate holes up to 80 without major chipping. The uncoated drill has large irregular Ti adhesion due to edge chipping occurred during Ti machining.

- The DLC coating despite of its low friction does not particularly minimize Ti adhesion during the CFRP-Ti stack drilling experiments. The DLC coating was readily removed from the cutting edge and margin of the drill tool even before making hole 10. Another factor of the DLC coating's low performance can be the relatively thin coating, which the coating process limits its thickness to about 1.7 μm.

- The (AlCrSi/Ti)N coating has a significant reduction of tool wear in this study. The (AlCrSi/Ti)N coating is still intact although some exposure of the substrate is beginning to show from hole 40. The (AlCrSi/Ti)N coating did not fail until making 80 holes with the gradual wear patterns consisting of flank wear and edge rounding.

- Compared to our previous results [88] with about 3μm-thick (AlCrSi/Ti)N coating on CFRP/Ti stack, 7.3 μm-thick- (AlCrSi/Ti)N coating performed extremely better. The thickest (AlCrSi/Ti)N coating may be effective when drilling the top CFRP resulting in the superior tool life to the other two drills.

CHAPTER 6: TOOL WEAR ANALYSIS ON COATED CARBIDE IN TURNING TI64[†]

1. Work materials

The cylinder Ti64 bar provided by RollerAlloys Inc (Michigan, U.S) has the outer diameter of 125 mm and the length of 673 mm. The microstructure of work material is captured by scanning electron microscopy (SEM) in backscattered electron imaging (BEI) as observed in Figure 6.1, which consists of fully equiaxed alpha grains (dark color) and lamellar phase (light color) with alternating alpha and beta phase.
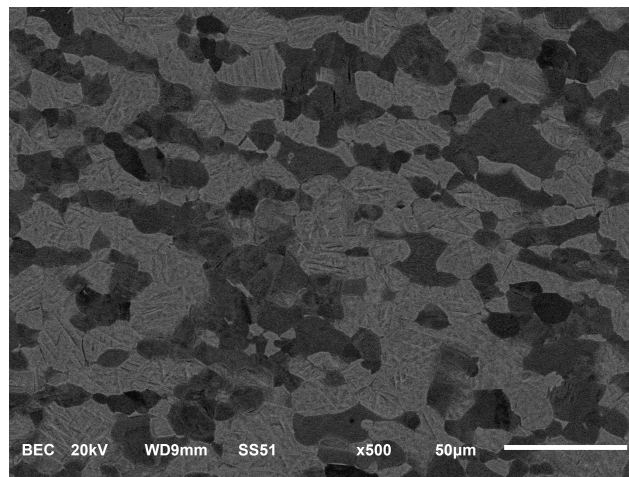
Figure 6.1. Microstructure Ti64 STA (BEI mode)

2. Experiments

2.1. Coated tools

The uncoated carbide inserts (SCMW 432-H13A) provided by Sandvik Coromant (Hebron, KY) with geometry SCMW 12 04 08 and tool holder SSBCR 2525R 12 were chosen for cutting

---

[†] This chapter was summitted at "Ryan Khawarizmi, Dinh Nguyen, Yang Guo, Patrick Kwon, 2020, June. A feasability study of coated inserts for turning ti-6al-4v, 2020. In ASME 2020 15th International Manufacturing Science and Engineering Conference. American Society of Mechanical Engineers. (be summitted Oct 31th 2019, under reviewing)."

insert with the rake angle and relief angles of 0^0 and 7^0, respectively. No chip breaker inserts were purposely chosen to eliminate the cutting temperature variations on the rake face. The detailed specification of the insert, whose average size of the carbide grains is 1 μm, is given in Table 6.1.

Table 6.1. Specification of the uncoated carbide insert used
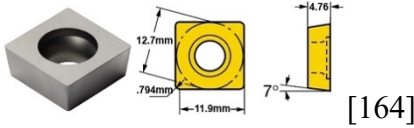
Grade	H13A
Substrate	WC + Co (6 wt. %)
Thermal conductivity	65 W/m·K
Dimension	[164]

Table 6.2. Coating inserts used in turning experiments

Coating	Substrate	Layer thickness (μm)	Layer structure
Uncoated carbide	WC	-	-
MM1115	WC	1.8	Two layer
MM1125	WC	3.6	Two layer
BAM1	WC	3.5	Single layer
BAM2	WC	4.3	Double layer
TiAlN	WC	2.3	Single layer
AlTiN	WC	1.33	Single layer
ZrN	WC	2.03	Single layer
(AlCrSi/Ti)N3	WC	3.3	Multilayer Nanocomposite
(AlCrSi/Ti)N7	WC	6.7	Multilayer Nanocomposite

Five coatings processed by Fraunhofer USA (East Lansing, Michigan) namely, AlMgB14(BAM), $Al_{0.66}Ti_{0.34}N$ (AlTiN), $Ti_{.5}Al_{.5}N$, ZrN, (AlCrSi/Ti)N were used for turning experiments in addition to the uncoated carbide. BAM coating, which has a considerably low

friction, has two types: single layer (BAM1) with 3.5 of thickness and double layer (BAM2) of 4.3 μm. The (AlCrSi/Ti)N coating is a multilayer coating structure which compose alternatively of AlCrSiN layer and TiN layer. The AlCrSiN layer has a nanocomposite structure which the nanocrystalline AlCrN grains embedded in amorphous Si_3N_4 matrix. In these experiments, there are two types of the (AlCrSi/Ti)N coating, they are (AlCrSi/Ti)N3 with 3 μm of thickness and (AlCrSi/Ti)N7 with 7 μm of thickness. To measure the thickness and the layer structure of those coating, the diamond saw was used to section of all inserts and the line scan technique of SEM/EDX was applied. The thickness of all grades used in experiments are shown in the table 6.2.

2.2. Experiment set-up
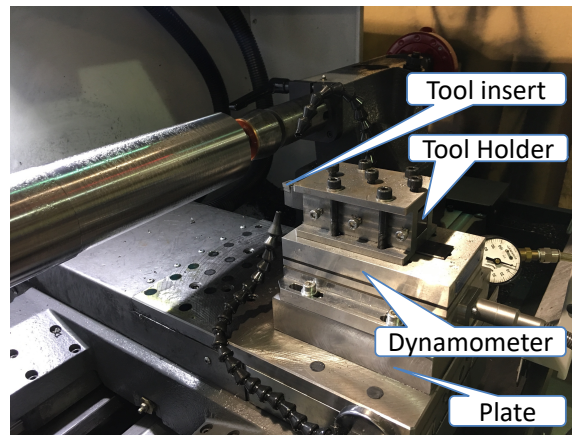
Figure 6.2. Experimental set up.

The straight turning experiments were conducted on CNC Lathe (TL01, Haas Automation Inc., California, USA). For each experimental condition, the surface cutting speed, depth of cut, and feed rate are fixed at 122 m/min, 1.2 mm, and 0.127 mm/rev, respectively and in the dry condition. The cutting forces in three directions were measured during the turning tests with Kistler stationary dynamometer (Kistler Instrument Corp., Amherst, NY) including Kistler Piezo-

Multicomponent Stationary Dynamometer type 9257B, the Kistler Multichannel Charge Amplifier type 5070A, the Kistler acquisition system type 5697A and Kistler Dynoware type 2825A The experimental setup is shown in Figure 6.2. These experiments for each type of inserts were carried out until the fracture happened.

2.3. Tool wear measurement

After turning experiments, the Ti-adhesion layers on the inserts are removed. With Uncoated, AlTiN and (AlCrSi/Ti)N the HF solution is applied to etch these layers however with BAM and ZrN grade, the steel brush is used mechanically to remove the layers. The flank and crater wear are captured with Olympus Fluoview FV1000 Confocal Laser Scanning Microscopy (CLSM) using reflect laser z-stack with the magnification of 20x, and the step size of 1 μm The CLSM data including conjugal focal plane images are overlapped to generate the height encoded images (HEI). Then the wavelet-based algorithm constructed in MATLAB [165] to eliminate the noise from the HEI images. The 2D profile of flank and crater are extracted from the three-dimensional images as shown in figure 3.3.

3. Results and discussion
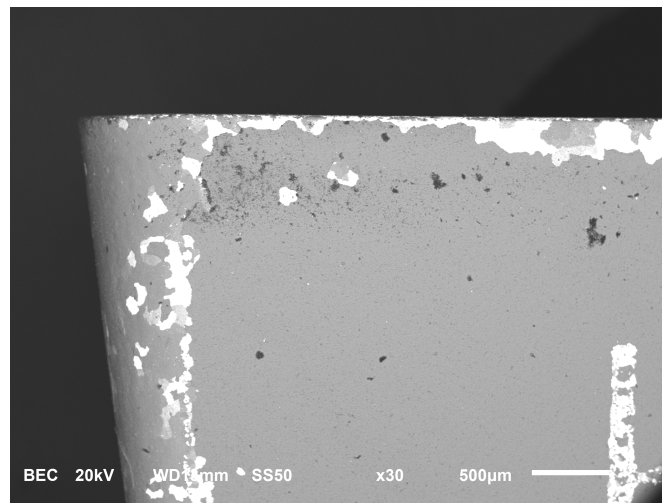
Figure 6.3. SEM image of flank face of TiAlN coated insert

115

The premature failure occurred at the beginning of the experiments with TiAlN coating inserts. Initially, the TiAlN coating did not adhere well to the substrate of uncoated carbide and flank off at cutting edge and flank face of the inserts as shown in the figure 6.3. Therefore, no additional experiments were performed for this coating.

	61 m/min	122 m/min
MM1115	1:21	0:13
MM1125	0:55	0:10
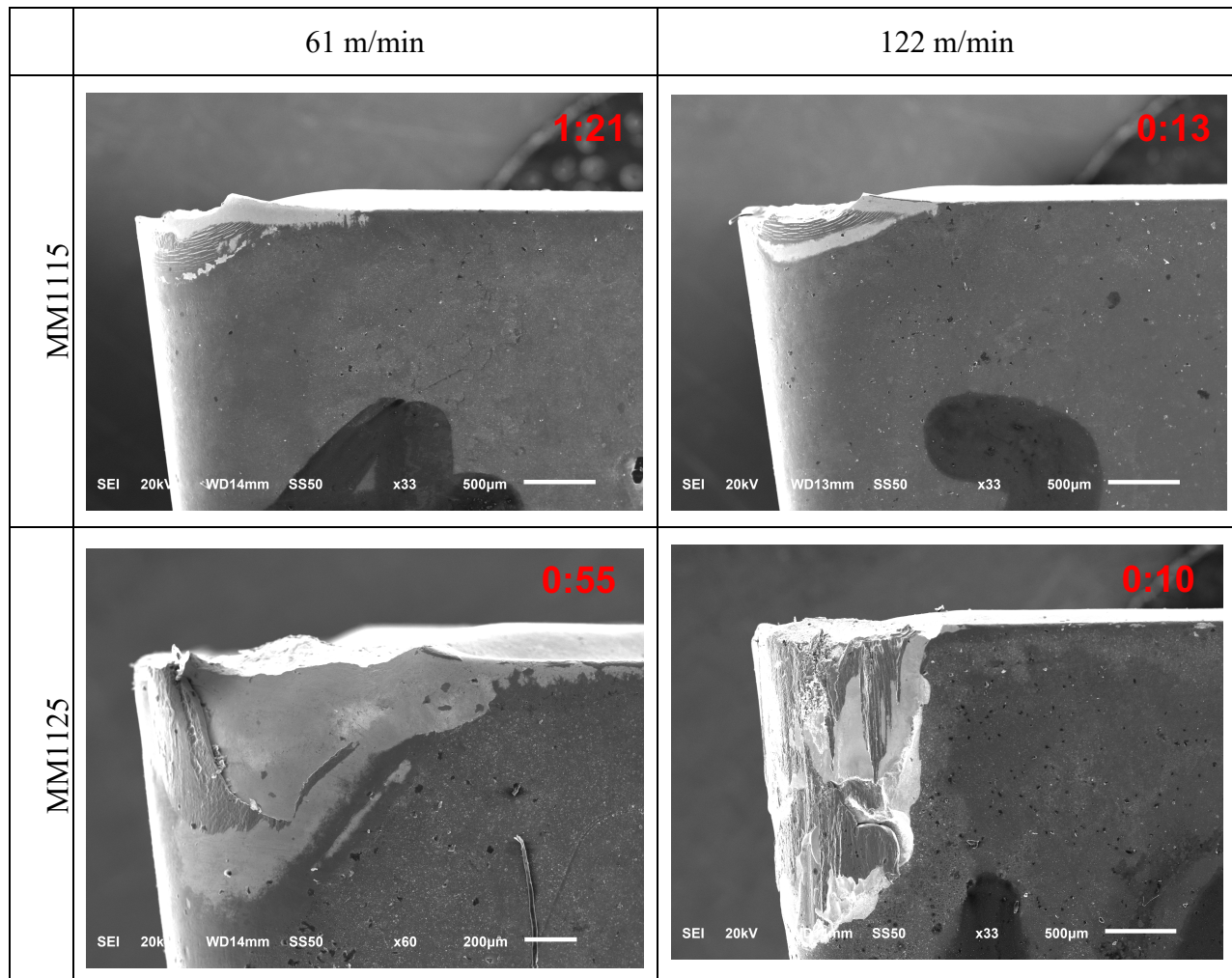
Figure 6.4. SEM image of MM1125 and MM1125

The MM1115 and MM1125 inserts, commercial available TiAlN/Al$_2$O$_3$, also underwent severely wear and fracture during the experiments at low and high speeds as shown in figure 6.4. For MM1115, the fracture happened at low speed, 61 m/min, and high speed, 122 m/min, after cutting 81 and 13 seconds, respectively. The fracture occurred more severe in MM1125 at both

speed. At low speed, it happened at 55 seconds and at high speed, it was 10 seconds. Due to the quick failure happened, no further experiments were performed on these coatings.

3.1. Cutting force measurement
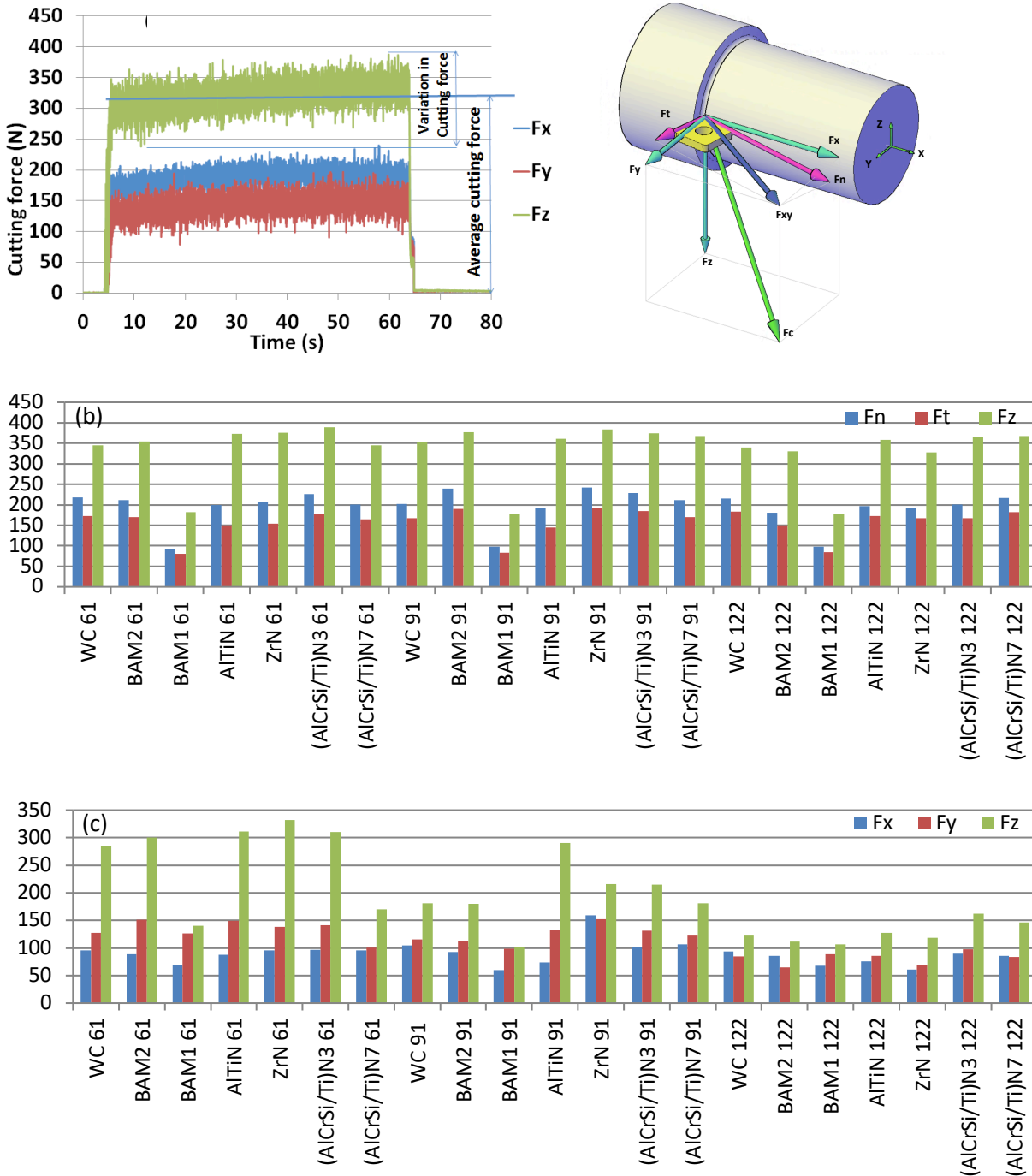
Figure 6.5. Cutting forces in x, y, z direction from all grades with 3 speeds 61, 91 and 122 m/min

The figure 6.5.a presents the schematic of cutting force components during the machining experiments, which the sample rate of cutting force was set at 100. The total cutting force (Fc) can be decomposed in three directions, x (feed), y (radical) and z (tangential), they are thrust force (F_X), radial force (F_Y) and cutting force (F_Z). The thrust and radial forces are geometrically related to the tool cutting-edge angle, which can be converted into the normal (F_N) and tangential force (F_T). The average and variation of all cutting force components were present in figure 6.5.b and c.

At three speeds, the average and variation of cutting forces from the BAM1 inserts, BAM single layer coating, has significant reduce in compare with other coating.

3.2. Tool wear

The average flank wear land (V_B) and maximum crater depth as a function of cutting length at three speeds are presented on figure 6.6. At the low cutting speed, all the inserts except the (AlCrSi/Ti)N7 coated insert fractured when the cutting length reached between 400 and 800m, with the least tool life with the uncoated inserts is attained with the cutting distance of roughly 500m. (AlCrSi/Ti)N7 coated inserts lasts more than the cutting length of 1400 m with the flank wear land only reaching 160 μm without any fracture. Next BAM1 coated inserts performed the best reaching the cutting distance over 1100 m. (AlCrSi/Ti)N3 coated inserts performed initially better than the (AlCrSi/Ti)N7 until reaching the cutting length of 700 m, then rapidly worn and eventually failed at 900 m cutting length. All the other coated inserts, even though not performing as well as (AlCrSi/Ti)N7 and BAM1 inserts, performed better than the uncoated inserts.

At the medium cutting speed, the uncoated inserts still failed only after reaching the cutting length of around 500m. However, all the other coated inserts except BAM1 failed much earlier after reaching the cutting distance of 200-300 m. (AlCrSi/Ti)N7 did not work at this cutting speed as it fractured after reaching the cutting length of 300m. However, it never reached the maximum

flank wear length due to the premature failure when the flank wear land reached less than 200 m. It can be speculated that all the coating except the BAM1 coating may have prematurely detached at this cutting speed. For the high cutting speed, all inserts failed before reaching the cutting length of 200 m with each insert indistinguishable in determining tool life. Again, the BAM1 coated inserts has the best tool life with the cutting distance of 300 m.
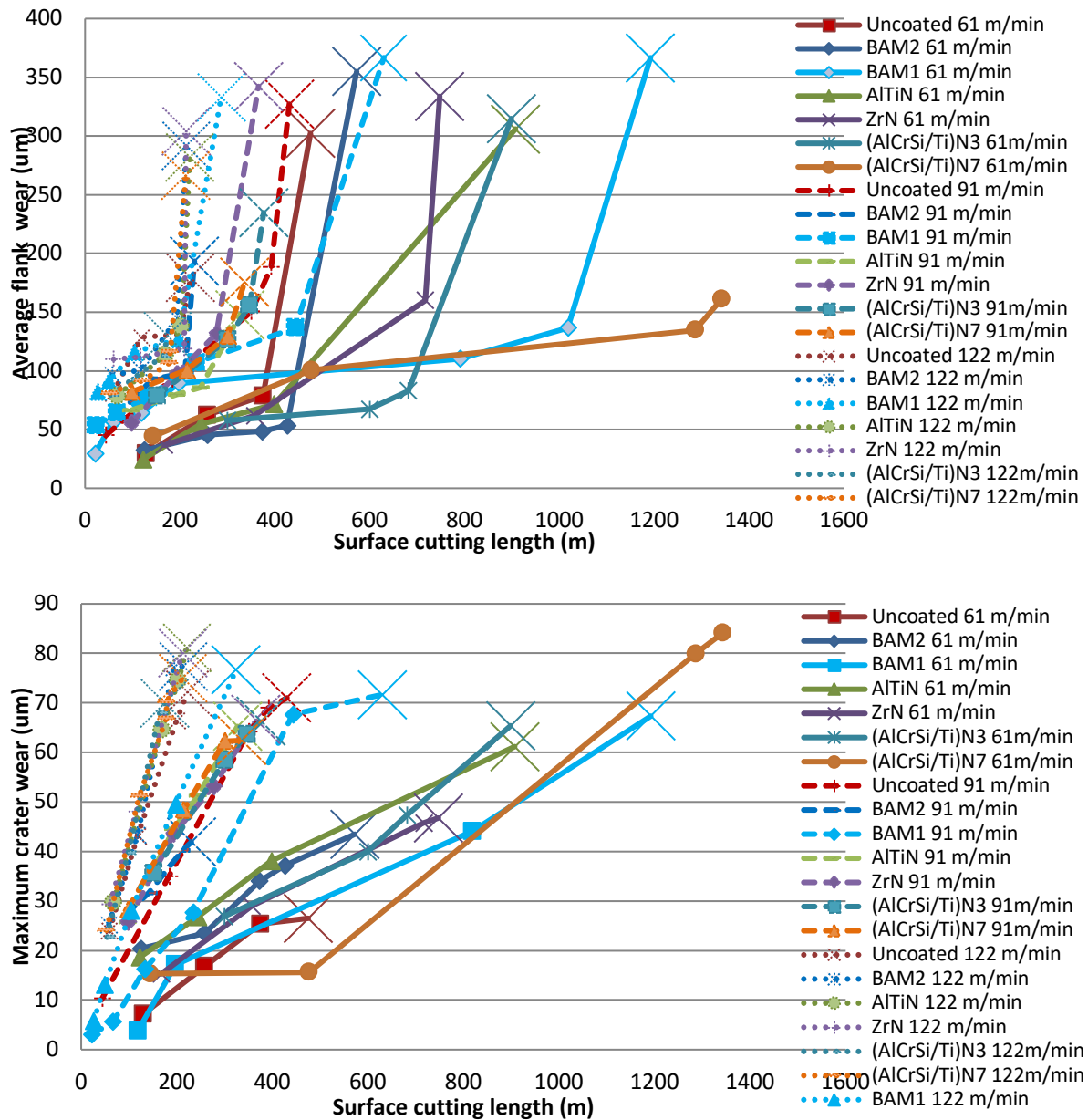
Figure 6.6. Flank wear and crater wear at three speeds of 61, 91 and 122 m/min.

At the low speed, 61 m/min, when the abrasive wear dominates, the excellent hardness of (AlCrSi/Ti)N improved the tool life significantly. At room temperature, the hardness of (AlCrSi/Ti)N is the highest, it reaches to 35-40 GPa in compare with carbide and other coatings, they are not over 32 GPA as shown in the table 6.3. At the medium and high speed, when the dissolution/diffusion wear occurs. The (AlCrSi/Ti)N coating does not provide the resistance tool wear due to the the hardness degrades. The BAM coating, whose friction coefficient is reported to be as low as 0.02 [166], improved the tool life better than (AlCrSi/Ti)N coating.

Table 6.3. Hardness of various coating materials

Coating	Hardness (GPa)	Ref
WC	23.5	[167]
BAM	30-32	[166]
AlTiN	30.7	[168]
ZrN	22	[169]
(AlCrSi/Ti)N	35-40	[170]

4. Conclusion

Our straight turning experiments presented preliminary tool wear study of the turning process on Ti64. With regards to tool wear in Ti turning, the main points that may be concluded from the study are:

- The TiAlN and commercial available coated carbide inserts failed prematurely during machining experiments due to the those coating did not adhere strongly with substrate.

- No substantial difference in the average cutting forces among the coated and uncoated inserts except BAM with single layer coating.

- Thicker (7 um) multilayer nanocomposites (AlCrSi/Ti)N coating performed the best at low cutting speed. However, as the cutting speed increases, the coatings quickly wear down and do not offer any significant improvement.

- The tool life of the BAM coating with the thickness of 3.5 μm improved at medium and high speeds.

CHAPTER 7: WEAR EVALUATION OF MINIMUM QUANTITY LUBRICATION WITH EXFOLIATED GRAPHITE NANOPLATELETS IN TURNING TITANIUM ALLOY[†]

1. Overview

Recently, light-weight metals have drawn extensive attention in many applications in aviation and automotive industries in order to boost the fuel economy and reduce the carbon dioxide emission. Among the light-weight metals, titanium (Ti) alloy is ideal for many of these applications because of the extraordinary strength/weight ratio and the high operating temperature [171, 172], which are not offered by the other light metals. Table 7.1 compares the strength/weight ratios and the maximum service temperatures of the light-weight metals [173, 174].

Despite these advantages, the cost and machinability issues are the main obstacles in adopting Ti alloys for a wide range of applications. This study will focus on improving the machinability of Ti alloys. The poor machinability of Ti alloys comes from their low thermal conductivities [175, 176], which causes the heat to be trapped, instead of dissipating away, near the cutting edge while machining. Even at a moderate cutting condition, the maximum temperature on the rake face of the tool can reach well over 1,000°C [177]. Such a high temperature on a cutting tool significantly reduces the mechanical strength of the cutting tool. Moreover, due to the high chemical affinity with all available tool materials, not only the friction between tool and work material is high but also the adhesion layers are typically formed on the cutting tools. As the adhesion layers are intermittently detached, the fragments of the tool body are detached as well. This phenomenon is

---

[†] This chapter was published at "Nguyen, D., Lee, P., Guo, Y., Park, K.H. and Kwon, P., 2019. Wear Performance Evaluation of Minimum Quantity Lubrication with Exfoliated Graphite Nanoplatelets in Turning Titanium Alloy. Journal of Manufacturing Science and Engineering, pp.1-27."

classified as attrition wear. Consequently, the machining cost of Ti alloys in general increases up to four times of that of ferrous alloys [178].

In machining of ferrous alloys, the machinability has significantly improved by applying the coatings on carbide inserts. However, in machining Ti alloys, these coatings do not significantly improve the machinability. With the high cutting temperature, flood cooling provides the reasonable means to extract the heat and is commonly applied on the machining processes of Ti alloy. The flood cooling also has the added benefit of improving the surface finish and tool life. However, due to the health/environmental concerns and the eventual disposal cost of cutting fluid [179-181], minimum quantity lubrication (MQL) was proposed as an ecologically viable machining solution. Despite of the inadequate cooling in machining Ti alloys, MQL provides the ample lubrication by applying the oil droplets generated by compressed air. This study explores MQL as an alternate enhancement technology and studies the capability and limitation of this technology in the turning process of Ti alloys.

MQL based machining uses the minute amounts of oil (5-500 cc/hr), which is transformed into micron-sized droplets by applying compressed air. These droplets are applied directly onto the tool/workpiece interface to enhance various machining processes. Heinemann et al. [182] carried out deep hole drilling experiments on AISI 1045 steels with three media such as synthetic ester, synthetic ester with 20% alcohol, and oil-free synthetic lubricant with water, while applying external MQL. The best results were obtained with the oil free synthetic with water due to the high cooling capacity and low viscosity. Yoshimura et al. [183] reported the device to generate the water droplets covered with oil film and carry out MQL experiments. The results showed that the combination of oil and water as MQL media provides improved cooling ability while reducing the cutting force.

More recently, MQL machining with nanofluid has been applied to enhances the lubrication and heat transfer. Shen et al. [184] carried out the MQL grinding experiment with the nanofluid mixed with MoS_2 nanoparticles and reported the considerable reduction in cutting force. Park et al. [185] reported the outstanding results on flank wear with vegetable oil mixed with exfoliated graphite nanoplatelets (xGnPs) with the milling process of AISI 1045. Spherical nanoparticles were used to enhance the ball/rolling bearing effects. Nano-diamond, nano-alumina, and fullerene (C_{60}) are the representative spherical nanoparticles. Lee et al. [186] observed the reduction in cutting forces and the improvement in the workpiece surface qualities during micro-grinding process using MQL with nano-diamond and alumina particles and found that the size and concentration of the nanoparticles are important parameters. They also investigated the thermal effects of nano-diamond during micro-grinding process using MQL [187]. With experimental and computational fluid dynamics (CFD) results, they reported on the tribological benefits and high heat transfer enhanced by the nano-diamond particles in reducing the temperature on the workpiece surface.

Table 7.1. Properties of light-weight metals [173]

Materials	Strength/weight ratio [kN·m/Kg]	Operating temperature [°C]
Ti-6Al-4V (Titanium alloy)	260	350-400
AZ63 (Magnesium alloy)	109	120 [174]
6061-T6 (Aluminum alloy)	115-130	130

The research works described above shows the enhancement of MQL when using nanofluid on drilling, milling and grinding. However, its effectiveness in turning process have not been

studied extensively. Even though the effectiveness of MQL may be very limited due to the uninterrupted engagement of the workpiece on cutting tool, limited numbers of research works on turning process with MQL with or without nanofluid were reported. Attanasio et al. [188] performed the turning experiment on normalized 100Cr6 steel with TiN/Al$_2$O$_3$/TiCN coated insert in MQL condition of ester oil with extreme pressure (EP) additives (COUPEX EP46). The results showed that the tool life was improved when the nozzle is applied on the flank face. Bruni et al. [189] conducted MQL turning experiments on AISI 1040 steel with vegetable oil at the cutting speed of 235 m/min and the results, however, shows no improvement in tool wear and surface quality compared to the dry condition. Dhar et al. [190] turned AISI-1040 steel with MQL of Mobil Cut -102 and both the cutting force and flank wear reduced compared to the dry condition. Khan et al. [191] reported the turning experiment on AISI 9310 alloy steel with vegetable-oil based MQL in the wide range of high cutting speed from 223 to 483 m/min and the result showed the reduction in cutting temperature and flank wear and the elimination of build-up-edge (BUE). Other various turning experiments were carried out on various work materials showing the reduction in cutting force, temperature and surface roughness with MQL [192-197]. Thus, the current literature does not always provide the conclusive evidence if MQL can provide the effective enhancement in turning process.

So far, very limited research works were reported on turning process of Ti alloy especially with MQL and MQL with nanofluid and many detailed parameters on MQL are not well established. Revankar et al. [198] conducted the MQL turning of Ti–6Al–4V (Ti64) alloy using polycrystalline diamond (PCD) tool and optimized speed, feed rate and lubricant flow rates for better surface finish. Raza et al. [199] performed turning experiments with Ti64 alloy under varying lubrication conditions including dry, MQL, minimum quantity cooled lubrication

(MQCL), cooled air, flood and cryogenic conditions. The results show that MQL and MQCL conditions turns out to be feasible alternatives at low feed and speed conditions. Liu et al. [200] also performed a series of turning experiments of the nanocomposite-AlCrN/amorphous-Si$_3$N$_4$ coated insert on Ti–6Al–4V alloy with a wide range of cutting conditions by applying vegetable-based MQL on flank side. The optimal cutting condition for minimizing surface roughness under MQL condition was found. Gupta et al. [201, 202] performed MQL turning process of Ti–6Al–4V alloy with few nanofluid (the 3 wt% concentration of nano-scale graphite, MoS$_2$ and Al$_2$O$_3$ in vegetable oil). The machining parameters was optimized to improve the surface finish and to minimize tool wear. The best results were found to be at low cutting speed, low feed rate, high approach angle and graphite based nano-fluids.

This study discusses our results from experimental turning process of Ti64 alloy in STA microstructure under dry, MQL and MQL with nanofluid conditions. Different from the nanofluid with various nanoparticles in Lee et al. [186, 187] and Gupta et al. [201, 202], we found that nanofluid made of xGnPs with certain high aspect ratio (diameter/thickness) was necessary to provide the significant advantages in MQL. Recently, Cartori et al. [203] carried out MQL experiments with varying concentrations of solid lubricants, graphite and Polytetrafluoroethylene (PTFE) particles in water and vegetable oil to improving Ti64 machinability in finish turning in one cutting condition (cutting speed of 80 m/min, feed rate of 0.2 m/rev and depth of cut is 0.2 mm). The nose wear results showed all MQL experiments reduced the wear to 35-50%. This study reports on our turning experiments to determine if MQL is effective in turning Ti alloys. The results will significantly vary depending on the orientation of the MQL nozzle. This is reasonable as, even for the flood condition, the orientation and pressure of the coolant applied dictates its effectiveness in improving tool life [204]. First, the optimal nozzle orientation must be defined for

the turning conditions employed and an additional series of MQL turning experiments is conducted to compare the performances of various nanofluid with varying concentration of xGnPs. The experimental results of cutting force, tool wear show the effectiveness of MQL and MQL with nanofluids in turning Ti alloy.

2. Turning experiments Materials
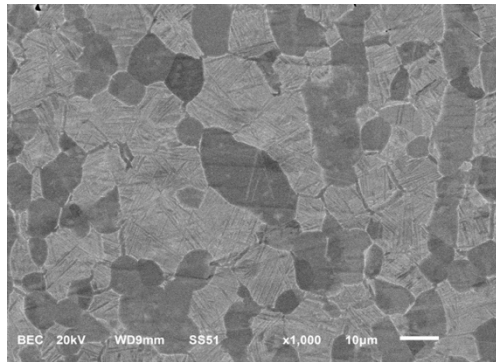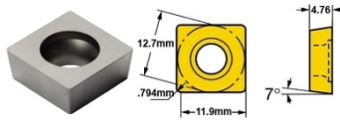
Figure 7.1. Microstructure of Ti64 in STA condition

In the experiments, a Ti-6Al-4V (Ti64) (Al 6 wt.%, V 4 wt.% and Ti 90 wt.% with Fe max 0.25 wt.% and O max 0.2 wt.%) round bar with the diameter of 127 mm and the length of 648 mm in the solution treated and aged (STA) condition [205] was used as a workpiece. The microstructure captured by scanning electron microscopy (SEM) in the backscattered electron imaging (BEI) mode is shown in Fig. 7.1, which consists of fully equiaxed alpha grains (dark color) and lamellar phase (light color) with alternating layers of alpha and beta phases [159]. The microstructures of Ti64s consist of various combinations of alpha and lamellar phases. The STA microstructure is a good representative microstructure of Ti64 with the similar contents of both alpha and lamellar phases.

Uncoated carbide inserts (SCMW 432-H13A, Sandvik Coromant, Hebron, KY) were chosen for the cutting insert with the rake and relief angles of 0° and 7°, respectively. The insert without any chip breaker was purposely chosen to eliminate the cutting temperature variations on the rake

face. The detailed specification of the insert, whose average size of the carbide grains is 1 μm, is given in Table 7.2.

Table 7.2. Specification of the uncoated carbide insert used

Grade	H13A
Substrate	WC + Co (6 wt. %)
Thermal conductivity	65 W/m·K
Dimension	[206]

The rapeseed-based oil (Coolube 2210 procured from Unist Inc., Grand Rapid, Michigan) with the flash temperature of 200°C was applied to generate MQL mist. The xGnPs are produced from graphite intercalated compounds by reaction with acids and exfoliation processed by their proprietary microware method to obtain the size reduction [207]. To obtain for our nanofluid, xGnPs manufactured by XG Science, Inc. (Lansing, Michigan) was mixed with the oil. The mixing was performed in magnetic stirrer 1120049SH (Fisher Scientific Inc.) at 700 rpm in 30 minutes, then sonicator CPX 15337427 (Fisher Scientific Inc.) in 1 hour to produce the stable nanofluid. The stabilities of the nanofluids with 0.1, 0.5, and 1.0 wt.% of xGnP were observed after 72 hours as shown in Fig. 7.3. The stability mixture was attained with 0.1 and 0.5 wt.% of xGnP. However, our previous ball milling experiment [207] indicated that 0.1wt.% of xGnP does not provide adequate lubrication. Based on the previous success on milling process [208], the xGnP M5 grade with the diameter of 5μm, the thickness of 6-8 nm and the surface area of 120-150 m^2/g was chosen and mixed with the oil to generate the nanofluid for MQL. SEM image of xGnP M5 grade is shown in Fig. 7.2.
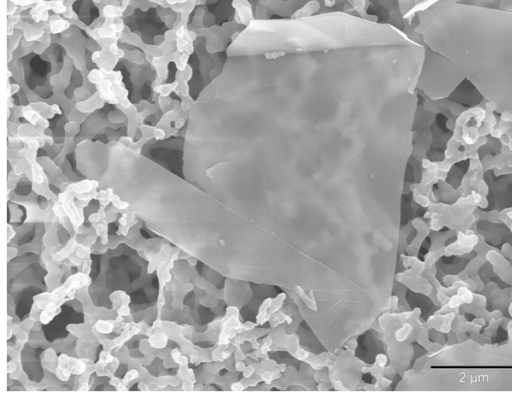
Figure 7.2. SEM micrograph of xGnP [209]
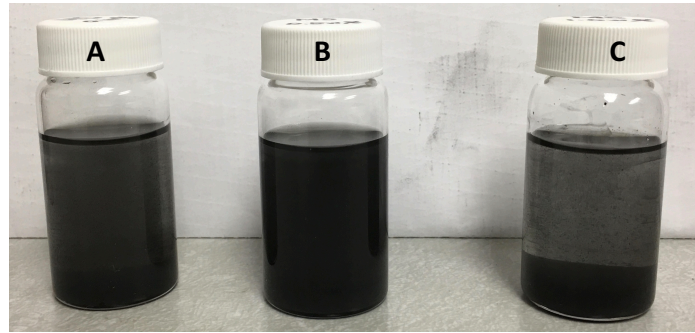
Figure 7.3. Mixture Stability of (a) 0.1, (b)0.5 and (c) 1.0 wt.% xGnP (M5 grade) (72 hours after mixing)

3. Experimental setup

The straight turning experiments were conducted on CNC Lathe (TL01, Haas Automation Inc., California, USA). The uncoated carbide inserts were mounted with the screw on the tool holder (SSBCR-2525M-12, Sandvik Coromant, Hebron, KY). The MQL dispensing system Uni-MAX (Unist Co., Grand Rapid, Michigan) was used to deliver the oil or nanofluid mist with the compressed air to the work-insert interface. The cutting forces in three directions were measured during the turning tests with Kistler stationary dynamometer (Kistler Instrument Corp., Amherst, NY). The cutting forces from the inserts mounted on Kistler tool holder type 9403 for the 25x25 shank cutting tool were measured by Kistler Piezo-Multicomponent Stationary Dynamometer type 9257B. The Kistler Multichannel Charge Amplifier type 5070A were used to amplify the input charges generated from the dynamometer. The channel sensitivities of the multichannel charge

amplifier were set for -7.854, -7.818 and -3.727 pC/N corresponding to the cutting forces in the x, y and z directions, respectively. The amplifier signal was obtained and converted using the Kistler acquisition system type 5697A and Kistler Dynoware type 2825A was used to store the force data in a computer. The force data acquisition was set at the rate of 100 sample/second. The experimental setup is shown in Fig. 7.4.
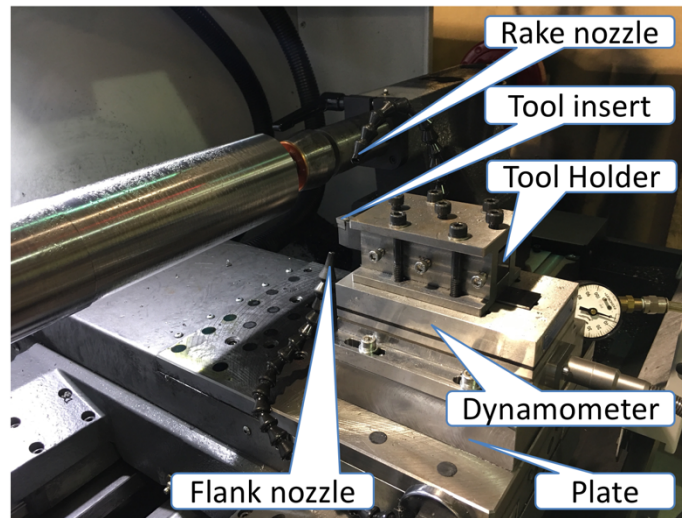
Figure 7.4. Experimental set up
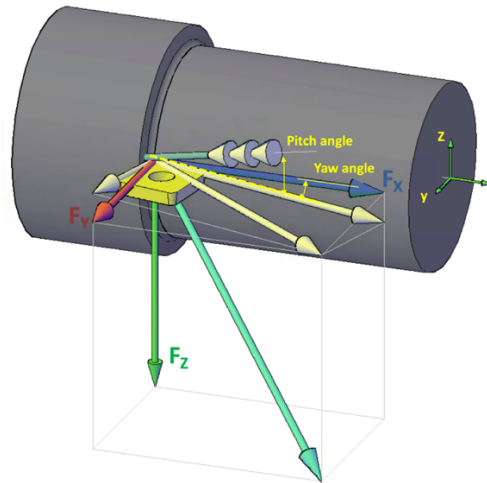
Figure 7.5. The cutting forces measured and the orientation of MQL nozzle in turning center

3.1. Experimental Design and Conditions

Table 7.3. Experimental design of MQL Experiments

Cases	Conditions	Pitch angle of nozzle	Yaw angle of nozzle
Dry	Dry	-	-
FNY15	MQL	-85° (Flank nozzle)	15°
RN15Y15	MQL	15° (Rake nozzle)	15°
RN15Y30	MQL	15° (Rake nozzle)	30°
RN15Y45	MQL	15° (Rake nozzle)	45°
RN45Y15	MQL	45° (Rake nozzle)	15°
RN75Y15	MQL	75° (Rake nozzle)	15°
RN15Y15 wt0.1	MQL with 0.1 wt% xGnP M5	15° (Rake nozzle)	15°
RN15Y15 wt0.5	MQL with 0.5 wt% xGnP M5	15° (Rake nozzle)	15°
RN15Y15 wt1.0	MQL with 1.0 wt% xGnP M5	15° (Rake nozzle)	15°
RN15Y15 wt2.0	MQL with 2.0 wt% xGnP M5	15° (Rake nozzle)	15°

Turning experiments of Ti-6Al-4V workpiece is conducted in three distinct conditions, dry, MQL, and MQL with nanoplatelets (0.1, 0.5, 1.0 and 2.0 wt. % of xGnP in M5 grade) to compare their performances. The advantage of the external MQL is that the location and orientation of the nozzle can be optimized. The nozzle distance is predetermined to be optimum at the distance of 5cm based on our previous work [209]. The nozzle orientation defined by pitch and yaw angles is illustrated in Fig. 7.5. The pitch angle is the angle between the feed rate direction (or x-direction in Fig. 7.5) and the projection of the nozzle direction onto XY plane. In this study, the yaw angle of the nozzle is set at three distinct angles, 15°, 30⁰ and 45° and denoted to be Y15, Y30 and Y45. Three distinct pitch angles of 15°, 45°, and 75° tested are denoted as RN15, RN45 and RN75 while the pitch angle of -85° is denoted as FN. The nozzle in FN sprays on the flank surface. Constrained by the space, only one condition of the pitch angle of -85° which represents the nozzle pointing at the flank surface was feasible. Because RN15Y15 provides the best performance in terms of tool

wear, further MQL experiment with various nanofluid was restricted to RN15Y15. Four distinct nanofluid with xGnPs (M5 grade) concentration of 0.1, 0.5, 1.0 and 2.0 wt.%, denoted RN15Y15wt0.1, RN15Y15wt0.5, RN15Y15wt1.0 and RN15Y15wt2.0, were used to determine the optimum concentration of xGnP (M5 grade) in nanofluid. The complete list of the MQL experiments are listed in Table 7.3.

The uncoated carbide insert was mounted by the screw on tool holder SSBCR-2525M (Sandvik Coromant, Hebron, KY) with the rake angle of 0°. As shown in Fig. 7.4, the large plate was added to support the dynamometer to level the tool tip with the center line of workpiece during the straight turning experiments. For each experimental condition, the surface cutting speed, depth of cut, and feed rate are fixed at 122 m/min, 1.2 mm, and 0.127 mm/rev, respectively. For the MQL, the flow rate and pressure of the MQL mist were 1.5 ml/min and 0.055 MPa (8 psi). The pressure of the compressed air is set at 0.055 MPa based on our previous work [185] which determined the optimum pressure to deposit most of the droplets onto the tribological surfaces of the insert. The distance between the MQL nozzle and workpiece was set to be 50 mm also based on our previous work [185]. The MQL conditions are summarized in Table 7.4.

Table 7.4. MQL spraying conditions

Lubricant	Dry, Vegetable oil (Coolube 2210), Lubricant enhanced by xGnP 0.5w%
Air pressure	8 psi
Flow rate	1.5 ml/min
Pitch angles of nozzle	15°, 45°, 75° (Rake) and 5° (Flank)
Nozzle distant	50-60 mm

3.2. Tool wear analysis

(c) 2D profile of flank wear

(d) 2D profile of crater wear

(a) HEI   (b) 3D Confocal Image
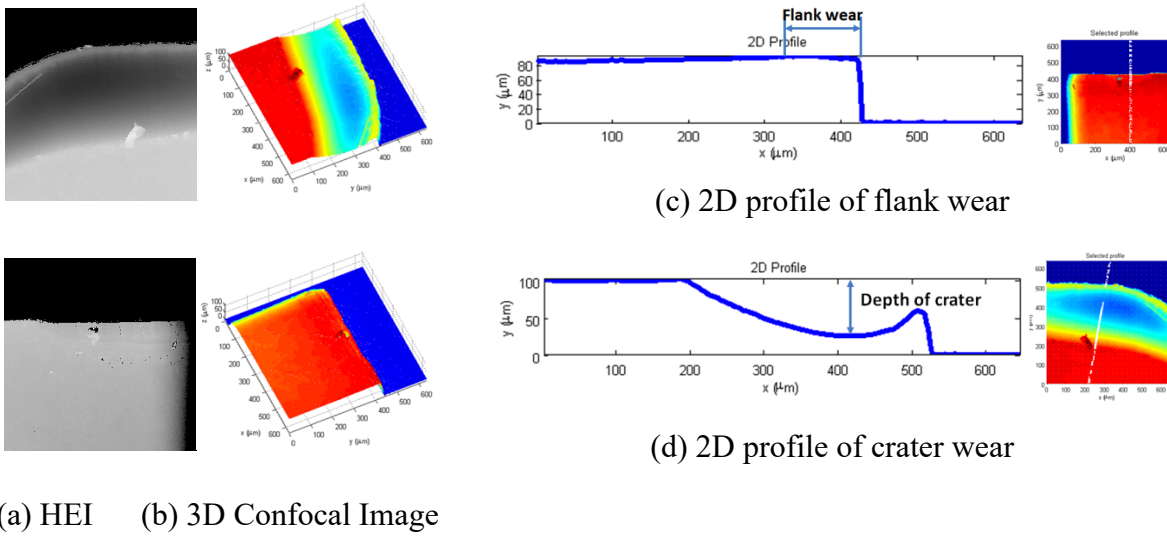
Figure 7.6. Tool wear analysis with 3D confocal images

After turning certain cutting lengths, the Ti-adhesion layers on the inserts are etched by hydrofluoric (HF) acid (52 wt.%) to capture the extent of both flank and crater wear with Olympus Fluoview FV1000 Confocal Laser Scanning Microscopy (CLSM) using reflect laser z-stack with the magnification of 20x, and the step size of 1 µm The CLSM data including conjugal focal plane images are overlapped to generate the height encoded images (HEI) (Fig. 7.6 (a)). The noise from the HEI images must be removed using the wavelet-based algorithm developed in MATLAB [210]. Three-dimensional images are constructed as shown in Fig. 7.6 (b). In Fig. 7.6 (c and d), the two-dimensional profiles in crater wear with 75° from x-axis (along the chip flow) were extracted while the profile representing flank wear was processed similarly with the vertical profiles.

4. Results and discussion

4.1. Cutting forces
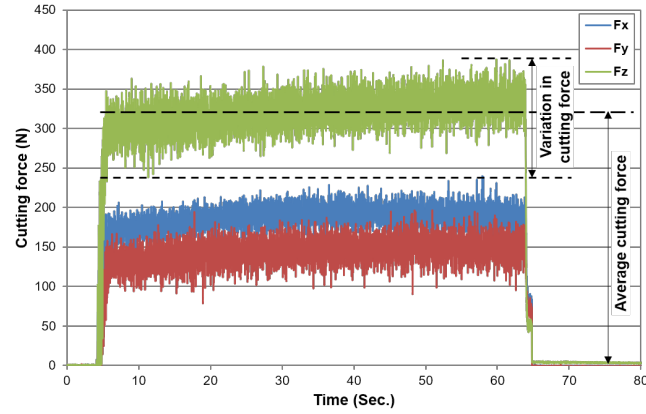
(a) Force signals from Dynamometer
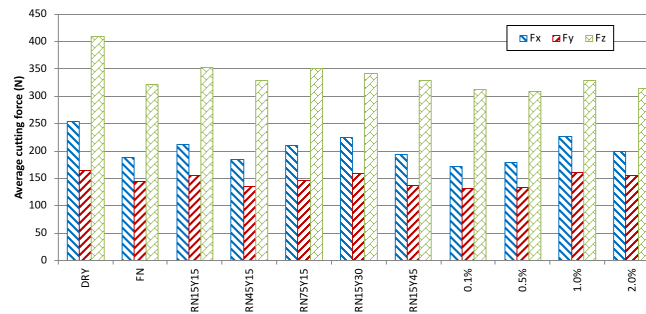
(b) Average cutting forces
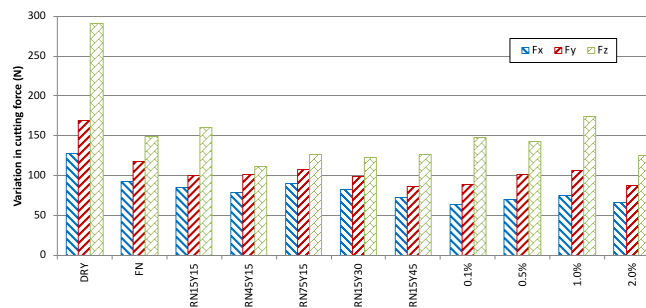
(c) Variation in cutting force

Figure 7.7. Cutting forces in x, y, z directions under various condition

A sample force signals in x (feed), y (radical), and z (tangential) directions were measured and presented in Fig. 7.7 (a). The results from our dry condition are similar to the force data

reported by Sun et al. [211]. The average of the measured force and the variation in the cutting forces in three direction are calculated and presented in Figs. 7.7(b) and 7.7(c), respectively.

The average cutting forces in the x, y, and z directions are 253 N, 165 N and 409 N, respectively, in the dry condition while the three average forces, which ranges between 184 and 225 N, 135 and 158 N, and 322 and 352 N, respectively, are consistently reduced in all MQL conditions. In terms of the pitch angle of the MQL nozzle, the average cutting forces in RN45Y15 shows slightly smaller than those of RN15Y15 and RN75Y15. Regarding the yaw angle, the cutting forces of RN15Y45 were reduced slightly compare to those of RN15Y15 and RN15Y30. Comparing between RN15Y15 and RN15Y15wt0.5, the forces in all three directions were decreased with the presence of xGnPs, and the forces in x, y, and z directions were reduced by 15.1, 9.7, and 7.7%, respectively.

Fig. 7.7(c) shows the variations in cutting forces. Clearly, the variations in the dry condition are substantially higher in all three directions than any MQL conditions. The variation in cutting forces in dry condition are 128N, 169N and 291 N, and those in MQL conditions ranges between 72 and 92 in x-direction, 87 and 117 in y-direction and 111 and 159 in z-direction. The variations in the cutting forces for any MQL condition were drastically reduced. Both the average and the variation in cutting forces in three directions in dry condition are significantly higher than those in MQL condition as the heat generation from cutting zone is partly dissipated by the air flow from MQL nozzle together with the lubrication provided by the oil droplets landed on the surfaces. These force data imply that the cutting time of any MQL condition lasted much longer than that dry condition. In addition, the MQL with nanofluid further reduce the cutting forces slightly.

4.2. Tool wear

To present the progress of tool wear, the average flank land (V_B) and maximum crater depth (K_t) as a function of cutting length under dry and various MQL conditions are presented on Figs. 7.8 (a, b, c and d). The characteristic progress of flank wear is that, after the initial wear, the steady state wear takes place followed by the abrupt acceleration in flank wear, which in this case caused by the attrition wear mentioned earlier while the crater wear depth steadily increases in each condition without any distinct difference among various conditions. Typically, the tool life criterion is defined when the average flank wear land reaches 300 μm [212, 200]. Thus, the turning experiments were continued until the flank wear land reaches 300 μm.

In dry condition, the flank wear of 300 μm reached when the cutting length reached 265 m. In term of the pitch angles in the MQL experiments, the flank wear in RN15Y15 last longer than those of FN, RN45Y15 and RN75Y15. The flank wear of RN15Y15 measured 380 m whereas those of FN, RN45Y15 and RN75Y15 are 310, 325 and 360 m, respectively. Comparing the yaw angles in the MQL experiments, RN15Y15 achieved a longer cutting length than those of RN15Y30 and RN15Y45 which measured 292 and 326 m, respectively. This study concludes that the nozzle orientation represented by the pitch angle of 15° and the yaw angle of 15° was optimal in term on flank wear. Clearly, in term of xGnP cases, both flank and crater wear in RN15Y15wt0.5 were significantly diminished compared to other conditions tested, attaining the cutting length of 520 m before reaching the tool life criterion. Thus, we can conclude that the attrition wear is substantially curtailed by the introduction of xGnPs. In FN condition, the flank wear is not as much curtailed despite of the oil mist spraying on flank face compared to other RN conditions. Conversely, the crater wear obtained from the FN condition is comparable to dry and other RN

conditions. The RN15Y15wt0.5 xGnP condition shows the most prominent improvement, being capable of reaching additional 255 m of cutting length.

The main flank mechanism was established to be the abrasion by the 'hard' orientation of the alpha clusters in our previous work [159] followed by attrition wear. With the presence of oil droplets in MQL experiments, the friction between tool and work material is expected to be reduced and, with the presence of additional xGnP, we expect to provide the lubrication even at high cutting temperature. This is evident by the fact that the tool life in RN15Y15wt0.5 xGnP lasted nearly twice longer than that of the dry condition.

For crater wear, the main wear mechanism is solubility/diffusivity [214, 215] due to the higher temperature at the rake face compared to that of the flank surface. With MQL, the rake temperature may be slightly reduced with the application of oil droplets and compressed air. However, at the cutting speed of 122 m/min, the cutting temperature at the rake face can reach over 1,000 °C [177]. At such temperature, the oil droplets can simply be vaporized as soon as they landed on the hot rake surface. As evident in Fig. 7.8(d), among four RN15Y15 with varying concentrations of xGnPs, 0.1, 0.5, 1.0 and 2.0w%, the best performance was also achieved with the xGnP concentration of 0.5w% while the inserts are fractured in the other three concentrations. Therefore, the presence of xGnPs with a certain threshold concentration is critical in reducing crater wear.
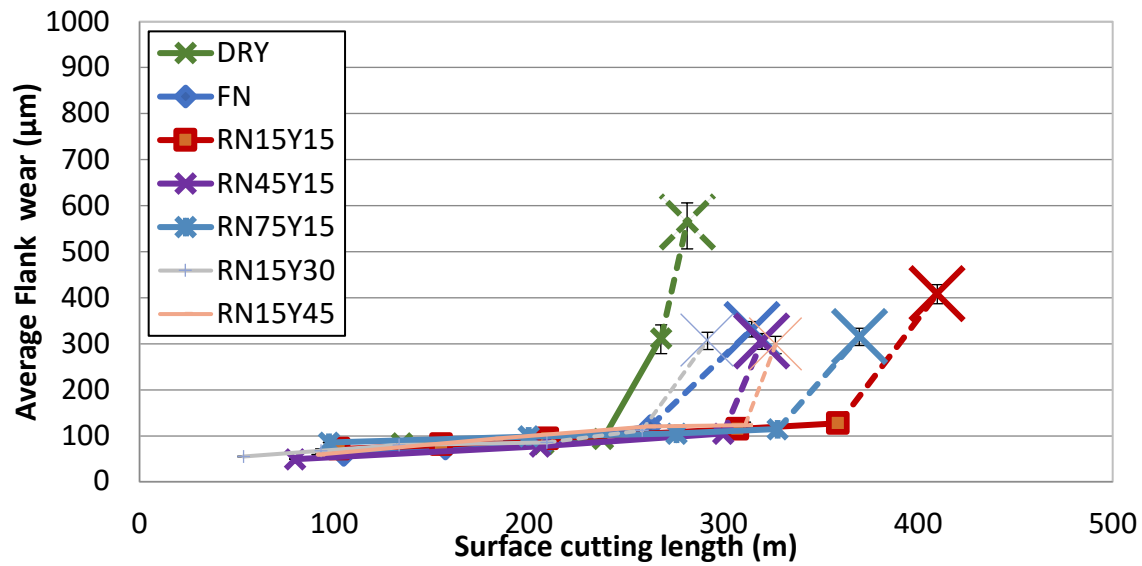
(a) Flank wear in various nozzle orientation
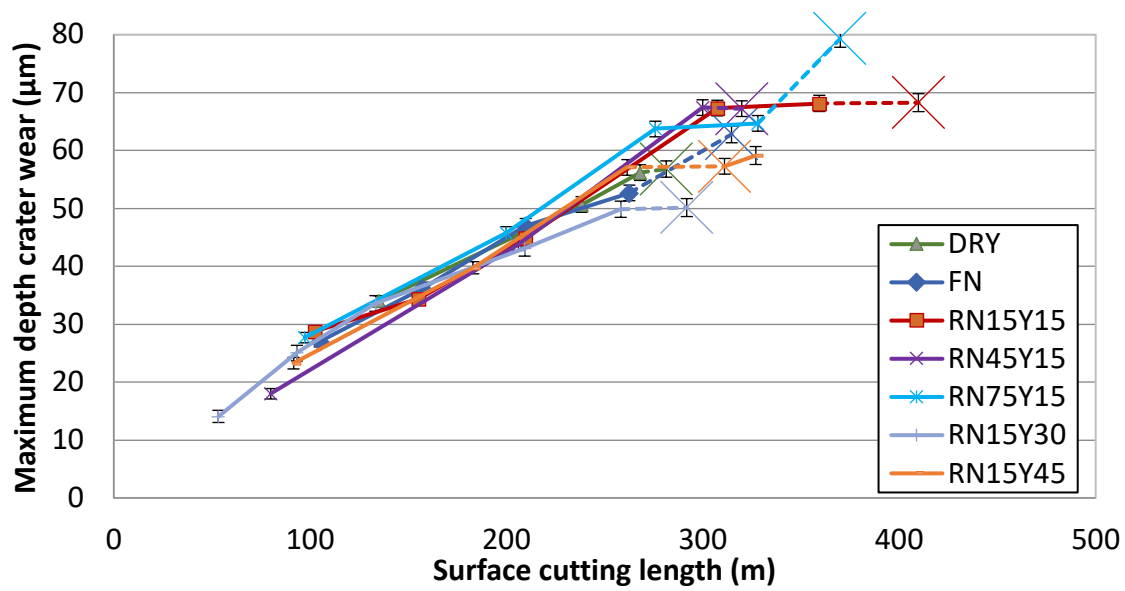
(b) Crater wear in various nozzle orientation

Figure 7.8. Tool wear under various conditions

Figure 7.8 (cont'd)
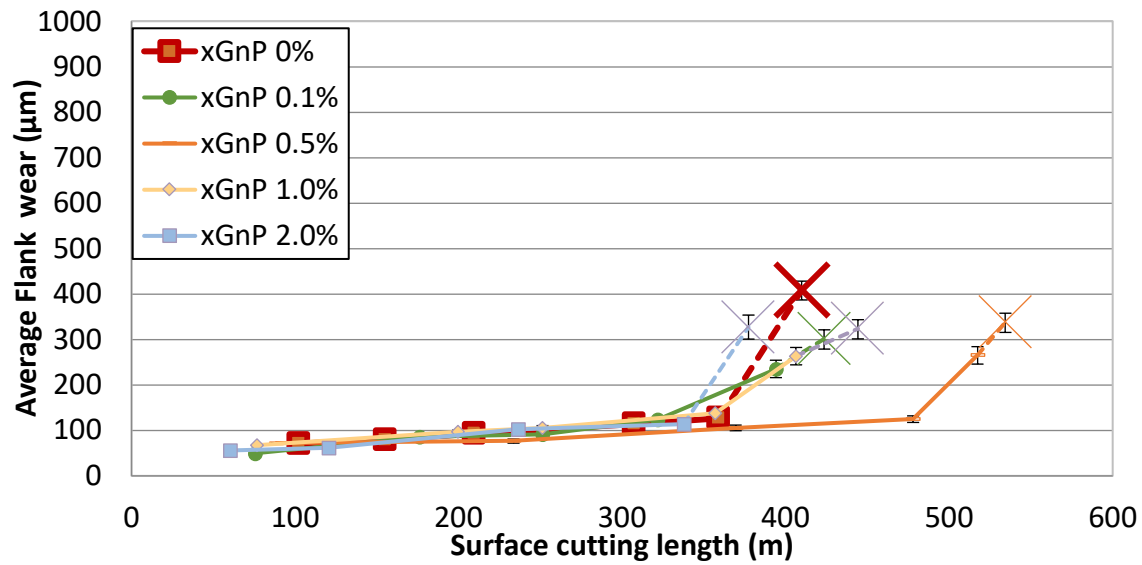
(c) Flank wear in four xGnP concentrations in nanofluid
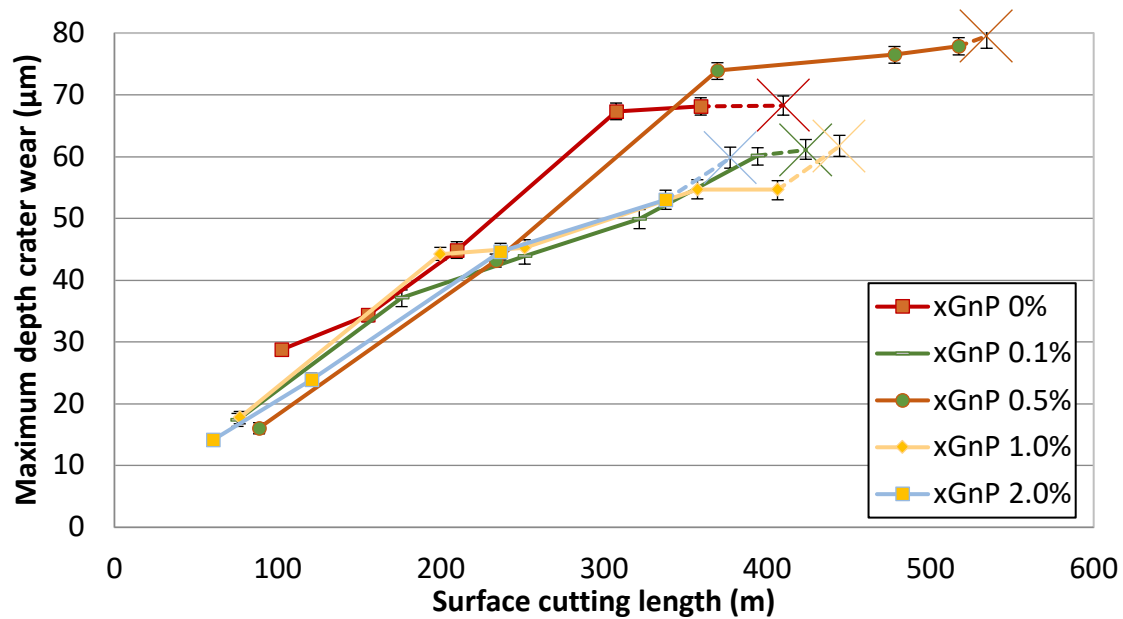
(d) Flank wear in in four xGnP concentrations in nanofluid

5. Conclusion

This study presented the preliminary study of turning Ti alloy in dry, MQL and MQL with nanofluid. In particular, many MQL conditions including nozzle orientation (various pitch angles:

FN, RN15, RN45, RN75 and various yaw angles: Y15, Y30, Y45) and lubrication conditions (dry, MQL, MQL with 0.1, 0.5, 1.0 and 2.0 wt.% of M5 grade of xGnP) were considered in the experiments. Based on the cutting forces and tool wear measured in this study, the following conclusions are drawn:

- The average cutting forces and the variations in cutting forces were considerably reduced in the case of MQL and further reduced with MQL with our nanofluid compared to dry condition.

- Flank wear was significantly reduced by applying MQL and MQL with xGnP compared to the dry condition. The maximum cutting length based on the standard flank wear was extended by approximately 75% in the MQL with 0.5wt.% of M5 xGnP. However, despite of the less distinguishable difference in crater depth among various MQL conditions (FN, RN 15, RN45 and RN75), the presence of xGnPs, which can survived at the high crater temperature, is important in reducing the crater wear.

- The orientation of nozzle MQL rake positions, the pitch angle of 15° and yaw angle of 15° were the most optimum orientation of the MQL nozzle in reducing flank wear.

REFERENCES

REFERENCES

[1] Leyens, C. and Peters, M., *Titanium and titanium alloys*. Wiley-VCH, Weinheim 2003.

[2] Yang, X. and R. C. Liu,. Machining Titanium and Its Alloys. *Machining Science and Technology*, *3*(1), (1999) 107–139.

[3] Donachie, M. J., A Primer on Titanium and Its Alloys. *Titanium: A Technical Guide*, second ed., ASM International, Mateials Park, 2000.

[4] Gogia, A.K., 2005. High-temperature titanium alloys. *Defense Science Journal*, *55*(2), (2005) 149 - 173.

[5] Elias, C. N., Lima, J. H. C., Valiev, R., & Meyers, M. a., Biomedical Applications of Titanium and its Alloys. *Journal of the Minerals, Metals, and Materials Society*, 60(3) (2008) 46–49.

[6] Ezugwu, E. O., & Wang, Z. M. Titanium alloys and their machinability. *Journal of Materials Processing Technology*, *68*(3), (1997) 262–274.

[7] Rack, H. J., & Qazi, J. I. Titanium alloys for biomedical applications. *Materials Science and Engineering C*, *26*(8) (2006) 1269–1277.

[8] Lütjering, G., & Williams, J. C. Titanium: Engineering Materials and Processes. Second edition, Springer, Leipzig, 2007.

[9] Veiga, C., Davim, J., & Loureiro, A. Properties and Applications of Titanium Alloys: A Brief Review. *Rev. Adv. Mater. Sci*, *32*, (2012) 133–148.

[10] Boyer, R., Welsch, G., & Collings, E. W. ASM Materials Properties Handbook: Titanium Alloys, ASM International, Material Park, 1994.

[11] Lütjering, G. Influence of processing on microstructure and mechanical properties of (α+β) titanium alloys. *Materials Science and Engineering: A*, *243*(1), (1998) 32–45.

[12] Nguyen, T., Kwon, P., Kang, D. and Bieler, T., 2016, 'The root Cause of Flank Wear in Turning Ti-6Al-4V with Carbides and PCD Inserts,' Journal of Manufacturing Science and Engineering, 136(4), 041018.

[13] Dearnley, P.A. and Grearson, A.N., Evaluation of principal wear mechanisms of cemented carbides and ceramics used for machining titanium alloy IMI 318. *Materials Science and Technology*, *2*(1), (1986) 47-58.

[14] Arrazola, P. J., Garay, A., Iriarte, L. M., Armendia, M., Marya, S., & Le Maître, F. Machinability of titanium alloys (Ti6Al4V and Ti555.3). *Journal of Materials Processing Technology*, *209*(5), (2009) 2223–2230.

[15] Khanna, N., Garay, A., Iriarte, L. M., Soler, D., Sangwan, K. S., & Arrazola, P. J., Effect of heat treatment conditions on the machinability of Ti64 and Ti54M alloys. *Procedia CIRP*, *1*(1), (2012) 477–482.

[16] Armendia, M., Garay, A., Iriarte, L. M., & Arrazola, P. J., Comparison of the machinabilities of Ti6Al4V and TIMETAL 54M using uncoated WC-Co tools. *Journal of Materials Processing Technology*, *210*(2), (2010) 197–203.

[17] Kosaka, Y., Fanning, J.C. and Fox, S.P., Development of low cost high strength alpha/beta alloy with superior machinability. In *Proceedings of the 10th World Conference on Titanium* (2004) 3028-3034.

[18] Attanasio, A., Gelfi, M., Pola, A., Ceretti, E., & Giardini, C. Influence of material microstructures in micromilling of Ti6Al4V alloy. *Materials*, *6*(9) (2013) 4268–4283.

[19] Gelfi, M., Attanasio, A., Ceretti, E., Garbellini, A. and Pola, A., Micromilling of Lamellar Ti6Al4V: Cutting Force Analysis. *Materials and Manufacturing Processes*, *31*(7), (2016) 919-925.

[20] Bermingham, M. J., Kirsch, J., Sun, S., Palanisamy, S., & Dargusch, M. S. New observations on tool life, cutting forces and chip morphology in cryogenic machining Ti-6Al-4V. *International Journal of Machine Tools and Manufacture*, *51*(6), (2011) 500–511.

[21] Narutaki, N., Murakoshi, A., Motonishi, S., & Takeyama, H., Study on Machining of Titanium Alloys. *CIRP Annals - Manufacturing Technology*, *32*(1), (1983) 65–69.

[22] Kitagawa, T., Kubo, A. and Maekawa, K., 1997. Temperature and wear of cutting tools in high-speed machining of Inconel 718 and Ti- 6Al- 6V- 2Sn. Wear, 202(2), pp.142-148.

[23] Zoya, Z. A., and Krishnamurthy, R., Performance of CBN tools in the machining of titanium alloys. *Journal of Materials Processing Technology*, *100*(1), (2000) 80–86.

[23] Dawson, S., 1999. Compacted graphite iron: mechanical and physical properties for engine design. Vdi Berichte, 1472, pp.85-106.

[24] Dawson, S., 2002. Process control for the production of compacted graphite iron. In 106th AFS Casting Congress, Kansas City (pp. 4-7).

[25] Tooptong, S., Park, K.H. and Kwon, P., 2018. A comparative investigation on flank wear when turning three cast irons. Tribology International, 120, pp.127-139.

[26] Souza, J.V.C., Nono, M.C.A., Ribeiro, M.V., Machado, J.P.B. and Silva, O.M.M., 2009. Cutting forces in turning of gray cast iron using silicon nitride based cutting tool. Materials & Design, 30(7), pp.2715-2720.

[27] Tasdelen, B., Escursell, M., Grenmyr, G. and Nyborg, L., 2007. Machining of gray cast irons and compacted graphite iron. In Swedish Production Symposium (pp. 1-6).

[28] Gastel, M., C. Konetschny, U. Reuter, C. Fasel, H. Schulz, R. Riedel, and H. M. Ortner. "Investigation of the wear mechanism of cubic boron nitride tools used for the machining of compacted graphite iron and grey cast iron." International Journal of Refractory metals and hard materials 18, 6 (2000): 287-296.

[29] Dawson, S., Hollinger, I., Robbins, M., Daeth, J., Reuter, U. and Schulz, H., 2001. The effect of metallurgical variables on the machinability of compacted graphite iron (No. 2001-01-0409). SAE Technical Paper.

[30] Da Silva, M.B., Naves, V.T.G., De Melo, J.D.B., De Andrade, C.L.F. and Guesser, W.L., 2011. Analysis of wear of cemented carbide cutting tools during milling operation of gray iron and compacted graphite iron. Wear, 271(9-10), pp.2426-2432.

[31] Abele E, Sahm A, Schulz H (2002) Wear mechanism when machining compacted graphite iron. CIRP Ann Manuf Technol 51(1): 53-56)

[32] Nayyar, V., Grenmyr, G., Kaminski, J. and Nyborg, L., 2013. Machinability of compacted graphite iron (CGI) and flake graphite iron (FGI) with coated carbide. International Journal of Machining and Machinability of Materials, 13(1), pp.67-90.

[33] Mocellin, F., Melleras, E., Guesser, W.L. and Boehs, L., 2004. Study of the machinability of compacted graphite iron for drilling process. Journal of the Brazilian Society of Mechanical Sciences and Engineering, 26(1), pp.22-27.

[34] Heck, M., Ortner, H.M., Flege, S., Reuter, U. and Ensinger, W., 2008. Analytical investigations concerning the wear behaviour of cutting tools used for the machining of compacted graphite iron and grey cast iron. International Journal of Refractory Metals and Hard Materials, 26(3), pp.197-206.

[35] Trent, E.M. and Wright, P.K., 2000. Metal cutting. Butterworth-Heinemann.

[36] Malakizadi, A., Sadik, I. and Nyborg, L., 2013. Wear mechanism of CBN inserts during machining of bimetal aluminum-grey cast iron engine block. Procedia CIRP, 8, pp.188-193.

[37] Fiorini, P. and Byrne, G., 2016. The influence of built-up layer formation on cutting performance of GG25 grey cast iron. CIRP Annals, 65(1), pp.93-96.

[38] Chen, M., Jiang, L., Guo, G. and An, Q., 2011. Experimental and FEM study of coated and uncoated tools used for dry milling of compacted graphite cast iron. Transactions of Tianjin University, 17(4), p.235.

[39] Ljustina, G., Larsson, R. and Fagerström, M., 2014. A FE based machining simulation methodology accounting for cast iron microstructure. Finite elements in analysis and design, 80, pp.1-10.

[40] Sima, M. and Özel, T., 2010. Modified material constitutive models for serrated chip formation simulations and experimental validation in machining of titanium alloy Ti–6Al–4V. International Journal of Machine Tools and Manufacture, 50(11), pp.943-960.

[41] Grzesik, W. and Zak, K., 2016. High Performance Machining of Nodular Cast Iron Using Coated Carbide and Ceramic Tools. Journal of Manufacturing Technologies, 41(3), pp.13-19.

[42] Nayyar, V., Kaminski, J., Kinnander, A. and Nyborg, L., 2012. An experimental investigation of machinability of graphitic cast iron grades; Flake, compacted and spheroidal graphite iron in continuous machining operations. Procedia CIRP, 1, pp.488-493.

[43] Calamaz, M., Coupard, D. and Girot, F., 2008. A new material model for 2D numerical simulation of serrated chip formation when machining titanium alloy Ti–6Al–4V. International Journal of Machine Tools and Manufacture, 48(3-4), pp.275-288.

[44] Sulaiman S., Roshan A., Borazjani S., 2013. Effect of Cutting Parameters on Cutting Temperature of TiAl6V4 Alloy. Applied Mechanics and Materials, Vol. 392, pp. 68-72

[45] Sumitomo Electric Carbide (2001) Sumitomo PCD and cBN Technical presentation, Sumitomo Electric Carbide, New York)

[46] Harris, T.K., Brookes, E.J. and Taylor, C.J., 2004. The effect of temperature on the hardness of polycrystalline cubic boron nitride cutting tool materials. International Journal of Refractory Metals and Hard Materials, 22(2-3), pp.105-110.

[47] Olortegui-Yume, J.A. and Kwon, P.Y., 2007. Crater wear evolution in multilayer coated carbides during machining using confocal microscopy. Journal of Manufacturing Processes, 9(1), pp.47-60.

[48] Wong, T., Kim, W. and Kwon, P., 2004. Experimental support for a model-based prediction of tool wear. Wear, 257(7-8), pp.790-798.

[49] Takatsu, S., Shimoda, H., Otani, K. (1983) Effect of CBN content on the cutting performance of polycrystalline CBN tools. Int J Refract Hard Mat 2(4):175–178.

[50] König W, Hochschule T, Komanduri R, Schenectady D, Tönshoff HK (1984) Machining of hard materials. Annal CIRP 33(2):417– 427)

[51] Hodgson T, Trendler PHH (1981) Turning hardened tool steels with cubic boron nitride inserts. Annals CIRP 30(1):63–66)

[52] Davies MA, Chou Y, Evans CJ (1996) On chip morphology, tool wear and cutting mechanics in finish hard turning. Annal CIRP 45 (1):77–82)

[53] Suh NP (1986) Tribophysics. Prentice-Hall, Englewood Cliffs, NJ

[54] Kramer BM (1986) A comprehensive tool wear model. Annal CIRP 35(1):67–70

[55] Bhaumik SK, Divakar C, Singh AK (1995) Machining Ti-6Al-4V alloy with a WBN-CBN composite tool. Mater Des 16(4):221–226)

[56] Liu, Y.C., Schissler, J.M. and Mathia, T.G., 1995. The influence of surface oxidation on the wear resistance of cast iron. Tribology international, 28(7), pp.433-438.

[57] Tennenhouse, G.J. and Runkle, F.D., 1987. The effects of oxygen on the wear of tungsten-carbide-based materials. Wear, 118(3), pp.365-375.

[58] Bushlya, V., Lenrick, F., Ståhl, J.E. and M'Saoubi, R., 2018. Influence of oxygen on the tool wear in machining. CIRP Annals, 67(1), pp.79-82.

[59] Rowe, G.W. and Smart, E.F., 1963. The importance of oxygen in dry machining of metal on a lathe. British Journal of Applied Physics, 14(12), p.924.

[60] Liu, J., Yamazaki, K., Ueda, H., Narutaki, N. and Yamane, Y., 2002. Machinability of pearlitic cast iron with cubic boron nitride (CBN) cutting tools. Journal of manufacturing science and engineering, 124(4), pp.820-832.

[61] Klimenko SA, Mukovoz YA, Lyashko VA, Ogorodnik VV, Vashchenko AN (1988) Wear on cubic boron nitride tools. Soviet J Superhard Mater 10(2):53-57

[61] H. Ho-Cheng and C. K. H. Dharan, "Delamination During Drilling in Composite Laminates," *J. Eng. Ind.*, vol. 112, no. 3, p. 236, Mar. 1990.

[62] W.-C. Chen, "Some experimental investigations in the drilling of carbon fiber-reinforced plastic (CFRP) composite laminates," *Int. J. Mach. Tools Manuf.*, vol. 37, no. 8, pp. 1097–1108, 1997.

[63] A. Koplev, A. Lystrup, and T. Vorm, "The cutting process, chips, and cutting forces in machining CFRP," *Composites*, vol. 14, no. 4, pp. 371–376, 1983.

[64] D. H. Wang, M. Ramulu, and D. Arola, "Orthogonal cutting mechanisms of graphite/epoxy composite. Part I: unidirectional laminate," *Int. J. Mach. Tools Manuf.*, vol. 35, no. 12, pp. 1623–1638, Apr. 1995.

[65] H. Y. Pwu and H. Hocheng, "Chip Formation Model of Cutting Fiber-Reinforced Plastics Perpendicular to Fiber Axis," *J. Manuf. Sci. Eng.*, vol. 120, no. 1, p. 192, Feb. 1998.

[66] L. C. Zhang, H. J. Zhang, and X. M. Wang, "A force prediction model for cutting unidirectional fibre-reinforced plastics," *Mach. Sci. Technol.*, vol. 5, no. 3, pp. 293–305, 2001.

[67] A. Faraz, D. Biermann, and K. Weinert, "Cutting edge rounding: An innovative tool wear criterion in drilling CFRP composite laminates," *Int. J. Mach. Tools Manuf.*, vol. 49, no. 15, pp. 1185–1196, 2009.

[68] S. Maegawa, Y. Morikawa, S. Hayakawa, F. Itoigawa, and T. Nakamura, "Effects of fiber orientation direction on tool-wear processes in down-milling of carbon fiber-reinforced plastic laminates," *Int. J. Autom. Technol.*, vol. 9, no. 4, pp. 356–364, 2015.

[69] M. Henerichs, R. Voß, F. Kuster, and K. Wegener, "Machining of carbon fiber reinforced plastics: Influence of tool geometry and fiber orientation on the machining forces," *CIRP J. Manuf. Sci. Technol.*, vol. 9, pp. 136–145, Feb. 2015.

[70] X. M. Wang and L. C. Zhang, "An experimental investigation into the orthogonal cutting of unidirectional fibre reinforced plastics," *Int. J. Mach. Tools Manuf.*, vol. 43, no. 10, pp. 1015–1022, Feb. 2003.

[71] M. K. Nor Khairusshima, C. H. Che Hassan, A. G. Jaharah, A. K. M. Amin, and A. N. Md Idriss, "Effect of chilled air on tool wear and workpiece quality during milling of carbon fibre-reinforced plastic," *Wear*, vol. 302, no. 1–2, pp. 1113–1123, Feb. 2013.

[72] M. K. N. Khairusshima and I. S. S. Sharifah, "Study on Tool Wear During Milling CFRP under Dry and Chilled Air Machining," *Adv. Mater. Process. Technol. Conf.*, vol. 184, pp. 78–89, 2017.

[73] N. K. Muhamad Khairussaleh, C. H. Che Haron, and J. A. Ghani, "Study on wear mechanism of solid carbide cutting tool in milling CFRP," *J. Mater. Res.*, vol. 31, no. 13, pp. 1893–1899, Feb. 2016.

[74] J. Sheikh-Ahmad and G. Sridhar, "Edge Trimming of CFRP Composites with Diamond Coated Tools: Edge Wear and Surface Characteristics," *SAE Tech. Pap. Ser.*, vol. 1, no. 2002, pp. 78–83, 2010.

[75] P. Janardhan, J. Sheikh-Ahmad, and H. Cheraghi, "Edge Trimming of CFRP with Diamond Interlocking Tools," in *Aerospace Manufacturing and Automated Fastening Conference and Exhibition*, 2006.

[76] S. C. Han, Y. Chen, J. H. Xu, and J. W. Zhou, "Experimental Study of Tool Wear in Milling Multidirectional CFRP Laminates," *Mater. Sci. Forum*, vol. 770, pp. 276–280, Feb. 2013.

[77] H. Buse and P. Feinle, "Model System Studies of Wear Mechanisms of Hard Metal Tools when Cutting CFRP," *Procedia Eng.*, vol. 149, pp. 24–32, Feb. 2016.

[78] T. Inoue, M. Hagino, D. U. Department of Mechanical Engineering 10-3 Takiharu-cho, Minami-ku, Nagoya 457-8530, Japan, and D. U. Department of Material and Environmental Engineering 10-3 Takiharu-cho, Minami-ku, Nagoya 457-8530, Japan, "Cutting Characteristics of CFRP Materials with Carbon Fiber Distribution," *Int. J. Autom. Technol.*, vol. 7, no. 3, pp. 285–291, Feb. 2013.

[79] M. Hagino, T. Inoue, D. U. Department of Material and Environmental Engineering 10-3 Takiharu-cho, Minami-ku, Nagoya 457-8530, Japan, and D. U. Department of Mechanical Engineering 10-3 Takiharu-cho, Minami-ku, Nagoya 457-8530, Japan, "Effect of Carbon Fiber Orientation and Helix Angle on CFRP Cutting Characteristics by End-Milling," *Int. J. Autom. Technol.*, vol. 7, no. 3, pp. 292–299, Feb. 2013.

[80] R. Prakash and V. Krishnaraj, "Experimental Study on Edge Trimming of Unidirectional CFRP Composites," *Adv. Mater. Res.*, vol. 984–985, pp. 207–213, Feb. 2014.

[81] A. Hosokawa, N. Hirose, T. Ueda, and T. Furumoto, "High-quality machining of CFRP with high helix end mill," *CIRP Ann.*, vol. 63, no. 1, pp. 89–92, Feb. 2014.

[82] R. Voss, L. Seeholzer, F. Kuster, and K. Wegener, "Analytical force model for orthogonal machining of unidirectional carbon fibre reinforced polymers (CFRP) as a function of the fibre orientation," *J. Mater. Process. Technol.*, vol. 263, pp. 440–469, Mar. 2019.

[83] R. Voss, L. Seeholzer, F. Kuster, and K. Wegener, "Influence of fibre orientation, tool geometry and process parameters on surface quality in milling of CFRP," *CIRP J. Manuf. Sci. Technol.*, vol. 18, pp. 75–91, Feb. 2017.

[84] Raveh, A., Zukerman, I., Shneck R., Avni, R., Fried, I. "Thermal stability of nanostructured superhard coatings: A Review," Surface and Coating Technology, 201(1), (2007): pp. 6136-6142. DOI: 10.1016/j.surfcoat.2006.08.131.

[85] Xu, J. and El Mansori, M., "Experimental study on drilling mechanisms and strategies of hybrid CFRP/Ti stacks," Composite Structures, 157, (2016): pp. 461–482.

[86] Isbilir, O. and Ghassemieh, E., Comparative Study of Tool Life and Hole Quality in Drilling of CFRP/Titanium Stack Using Coated Carbide Drill, Machining Science and Technology: An International Journal, 17:3, (2013): pp. 380-409, DOI: 10.1080/10910344.2013.806098

[87] Ghassemieh, E., 'Performance and wear of coated carbide drill in machining of carbon fibre reinforced composite/titanium stack', International Journal Materials and Product Technology, 43:1/2/3/4, (2012): pp.165–183.

[88] Wang, X., Kwon, P.Y., Sturtevant, C. and Lantrip, J. "Comparative tool wear study based on drilling experiments on CFRP/Ti stack and its individual layers." Wear 317:1-2 (2014) pp. 265-276. DOI: 10.1016/j.wear.2014.05.007.

[89] Ramulu, M., Branson, T. and Kim, D. "A Study on the Drilling of Graphite / Bismaleimide Composite and Titanium stacks." Composite Structures 54:1 (2001): pp. 67-77. DOI: 10.1016/S0263-8223(01)00071-X.

[90] Brinksmeier, E., and Janssen R. "Drilling of Multi-Layer Composite Materials consisting of Carbon Fiber Reinforced Plastics (CFRP), Titanium, and Aluminum Alloys." CIRP Annals-Manufacturing Technology 51:1 (2002): pp. 87-90. DOI: 10.1016/S0007-8506(07)61472-3.

[91] Kim, D., Ramulu, M. "Drilling process optimization for graphite/bismaleimide-titanium alloy stacks." Composite Structures 63:1 (2004): pp. 101–114. DOI: doi.org/10.1016/S0263-8223(03)00137-5.

[92] Kim, D., Ramulu, M. "Study on the drilling of Titanium/Graphite Hybrid Composites." ASME Transactions Journal of Engineering Materials and Technology 129:1 (2007): pp. 390-396. doi:10.1115/1.2744397.

[93] SenthilKumar, M., Prabukarthi, A. and Krishnaraj, V., "Study on tool wear and chip formation during drilling carbon fiber reinforced polymer (CFRP)/titanium alloy (Ti6Al4V) stacks." Procedia Eng., 64, (2013), pp. 582–92.

[94] Park, K., Kwon, P., Beal, A.., Kim, D., Lantrip, J. "Tool wear in drilling of composite/titanium stacks with carbide and polycrystalline diamond tools." Wear 271:11-12: (2011) pp. 2826-2835. DOI: 10.1016/j.wear.2011.05.038.

[95] Krishnaraj, V., R. Zitoune, F. Collombet "Comprehensive review on drilling of multimaterials stacks." Journal of Machining and Forming Technologies 2:3/4 (2010): pp. 171–200.

[96] Kuo, C. L., Soo, S. L., Aspinwall, D. K., Bradley, S., Thomas, W., M'Saoubi, R., Pearson, D. and Leahy, W., "Tool wear and hole quality when single-shot drilling of metallic-composite stacks with diamond-coated tools," Proc IMechE Part B: J Engineering Manufacture. 228:10 (2014); pp. 1314–1322.

[97] Larsi, L., Nouari, M., Mansori, El. "Modelling of chip separation in machining unidirectional FRP composites by stiffness degradation concept." Composite Science and Technology 69:5 (2007): pp. 684–692. DOI: 10.1016/j.compscitech.2009.01.004.

[98] Faraz, A., Biermann, D. and Weinert, K. "Cutting Edge Rounding: An Innovative Tool Wear Criterion in drilling CFRP Composite Laminates." International Journal of Machine Tools & Manufacture 49:15 (2009): pp. 1185-1196. doi:10.1016/j.ijmachtools.2009.08.002

[99] Wang, X., Kwon, P., Sturtvant, C., Kim, D., & Lantrip, J. "Tool wear of coated drills in drilling CFRP." Journal of Manufacturing Processes 15:1 (2013): pp. 127-135. DOI: 10.1016/j.jmapro.2012.09.019

[100] Kim, D., Beal, A., Park, K., Kwon, P., and Lantrip, J. "A Comparative Study of Carbide Tools in Drilling of CFRP and CFRP-Ti Stacks." ASME Transactions Journal of Manufacturing Science and Engineering 136:1 (2013): pp. 014501. DOI: 10.1115/1.4025008

[101] Kwon, P., Wang, X, Sturtevant, C., Kim, D., Lantrip, J. "Comparative tool wear study based on drilling experiments on CFRP/Ti stack and its individual layers." Wear, 317:1-2 (2014): pp. 265-276. DOI: 10.1016/j.wear.2014.05.007.

[102] Schrock, D., Kang, D., Bieler, T. R. and Kwon, P. "Phase Dependent Tool Wear in Turning Ti-6Al-4V Using Polycrystalline Diamond and Carbide Inserts." Journal of Manufacturing Science and Engineering, 136:4, (2014): pp. 041018. doi:10.1115/1.4027674.

[103] Sharif, S. and Rahim, E.A. "Performance of coated- and uncoated-carbide tools when drilling titanium alloy Ti-6Al-4V." Journal of Materials Processing Technology, 185:1-3 (2007): pp. 72-76. DOI: 10.1016/j.jmatprotec.2006.03.142

[104] Britton, T. B., Liang, H., Dunne, F. P. E. and Wilkinson, A. J. "The effect of crystal orientation on the indentation response of commercially pure titanium: experiments and simulations." Proceedings of Royal Society A: Mathematical, Physical and Engineering Sciences, 466: 2115 (2010): pp. 695–719. DOI: 10.1098/rspa.2009.0455.

[105] Kwon, J., Brandes, M. Phani, P.S., Pilchak, A. P., Gao, Y. F., George, E. P., Pharr, G. M. and Mills, M. J. "Characterization of deformation anisotropies in an α-Ti alloy by nanoindentation and electron microscopy." Acta Materialia, 61:13 (2013): pp. 4743–4756. DOI:10.1016/j.actamat.2013.05.005.

[106] Köef, A., Feistritzer, S., Udier, K. "Diamond coated cutting tools for machining non-ferrious metals and fibre reinforced polymers." International Journal of Refractory Metals and Hard Materials, 24: 5 (2006) pp. 354-359. DOI: 10.1016/j.ijrmhm.2005.11.013.

[107] Rawat, S., Attia, H. "Wear mechanisms and tool life management of WC–Co drills during dry high speed drilling of woven carbon fibre composites." Wear, 267:5–8 (2009): pp. 1022–1030. DOI:10.1016/j.wear.2009.01.031

[108] Lantrip J. "New Tools Needed, Cutting Tool Engineering." Cutting Tool Engineering 60:8 (2008): pp. 60-68. Url: http://www.ctemag.com/pdf/2008/0808-Holemaking.pdf

[109] Wolfgang, T. "Trends and market perspectives for diamond tools in the construction industry." International Journal of Refractory Metals and Hard Materials 18:6 (2000): pp. 301–306. DOI: 10.1016/S0263-4368(00)00034-2.

[110] Yang, X. and Liu, C.R., "Machining Titanium and Its Alloys." Machining Science and Technology 3:1 (1999): pp. 107-139. DOI: 10.1080/10940349908945686.

[111] Hartung, P. and Kramer, B. "Tool wear in titanium machining." CIRP Annals 31:1 (1982):pp. 75-80. DOI: 10.1016/S0007-8506(07)63272-7.

[112] Narutaki ,N. and Murakoshi, A. "Study on machining titanium alloys." CIRP Annals 32:1 (1983): pp. 65-69. DOI: 10.1016/S0007-8506(07)63362-9.

[113] Machado, A.R. and Wallbank, J. "Machining of titanium and its alloys- a review." Journal of Engineering Manufacture 204:1 (1990) pp. 53-60. DOI: 10.1243/PIME_PROC_1990_204_047_02.

[114] Zhang, P.F., Churi, N.J., Pei, Z.J., Treadwell, C. "Mechanical drilling processes for titanium alloys: a literature review." Machining Science and Technology 12, (2008): pp. 417–444. DOI: 10.1080/10910340802519379.

[115] Li, R., Hedge, P. and Shih, A.J. "High-throughput drilling of titanium alloys." International Journal of Machine Tools and Manufacture, 47:1 (2007): pp. 63-74. DOI: 10.1016/j.ijmachtools.2006.02.012.

[116] Okamura, K., Sasahara, H., Segawa, T., Tsutsumi, M. "Low-Frequency Vibration Drilling of Titanium Alloy." JSME International Journal Series C Mechanical Systems, Machine Elements and Manufacturing, 49:1 Special Issue on Advanced Manufacturing Technology [I] (2006): pp. 76-82. DOI: 10.1299/jsmec.49.76.

[117] Pecat, O. and Brinksmeier, E. "Tool Wear Analyses in Low Frequency Vibration Assisted Drilling of CFRP/Ti6Al4V Stack Material." Procedia CIRP, 14 (2014): pp. 142–147. 10.1016/j.procir.2014.03.050.

[118] Wong, T., Kwon, P., Kim, W., 2004, "A Predictive Model for Tool Wear on Coated Inserts," Wear, 257 (7-8), 790-798.

[119] Hartung, P. D. Tool Wear in Titanium Machining, S.M. Thesis, Department of Mechanical Engineering, M.I.T., June 1981.

[120] Sandvik Coromant Catalogue 2015.

[121] Britton, T. B., Liang, H., Dunne, F. P. E., & Wilkinson, A. J., The effect of crystal orientation on the indentation response of commercially pure titanium: experiments and simulations. Proceedings of the Royal Society of London A: Mathematical, Physical and Engineering Sciences, 466(2115) (2010) 695–719.

[122] Buades, A., Coll, B. and Morel, J.M., A review of image denoising algorithms, with a new one. Multiscale Modeling & Simulation, 4(2), (2005) 490-530.

[123] Kwon, P., Predictive models for flank wear on coated inserts. Journal of tribology, 122(1), (2000) 340-347.

[124] Ghosh, C., Basabe, V.V., Jonas, J.J., Kim, Y.M., Jung, I.H. and Yue, S., The dynamic transformation of deformed austenite at temperatures above the Ae 3. Acta Materialia, 61(7), (2013) 2348-2362.

[125] Zhang, Y., Outeiro, J. C., and Mabrouki, T., On the selection of Johnson-Cook constitutive model parameters for Ti-6Al-4V using three types of numerical models of orthogonal cutting. Procedia CIRP, 31, (2015) 112–117.

[126] Ulutan, D. and Özel, T., 2013. Determination of tool friction in presence of flank wear and stress distribution based validation using finite element simulations in machining of titanium and nickel based alloys. Journal of Materials Processing Technology, 213(12), pp.2217-2237.

[127] Lee, W.-S., & Lin, C.-F., High-temperature deformation behaviour of Ti6Al4V alloy evaluated by high strain-rate compression tests. Journal of Materials Processing Technology, 75(1), (1998) 127–136.

[128] Chen, G., Ren, C., Qin, X., & Li, J., Temperature dependent work hardening in Ti-6Al-4V alloy over large temperature and strain rate ranges: Experiments and constitutive modeling. Materials and Design, 83, (2015) 598–610.

[129] Kim, W. and Kwon, P., 2001. Understanding the mechanisms of crater wear. Transactions-North American Manufacturing Research Institution of SME, pp.383-390.

[130] Olortegui-Yume, J.A. and Kwon, P.Y., 2007. Crater wear evolution in multilayer coated carbides during machining using confocal microscopy. Journal of Manufacturing Processes, 9(1), pp.47-60.

[131] Hanlon, D.N., Todd, I., Peekstok, E., Rainforth, W.M. and Van der Zwaag, S., 2001. The application of laser scanning confocal microscopy to tribological research. Wear, 251(1-12), pp.1159-1168.

[132] R.C. Dawes, D.K. Aspinwall A review of ultra high speed milling of hardened steels Journal of Materials Processing Technology 69 (1997} 1-17

[133] Nakagnwa, T. lkeda, T. Matsuoka, High speed milling of steel and tool life, in: Proc, 8th Int, Conf. Tool, Die and Mold industry, International Special Tooting Association, Barcelona, Spain, 1993.

[134] Kramer, B.M. and Suh, N.P., 1980. Tool wear by solution: a quantitative understanding. Journal of Engineering for Industry, 102(4), pp.303-309.

[135] Kramer, B.M., 1979. An analytical approach to tool wear prediction (Doctoral dissertation, Massachusetts Institute of Technology).

[136] Shatynski, S. R. (1979). The thermochemistry of transition metal carbides. Oxidation of Metals, 13(2), 105-118

[137] Kwon, P. and Kim, W., 2002, Phase Transformation and Its Effect on Flank Wear, *Journal of Manufacturing Science and Engineering*, **124**, 3, pp. 659-666.

[138] https://www.americancarbidetool.com/technical-support/pcdcbn-materials/

[139] Ng, E.G., Aspinwall, D.K., Brazil, D. and Monaghan, J., 1999. Modelling of temperature and forces when orthogonally machining hardened steel. *International Journal of Machine Tools and Manufacture*, *39*(6), pp.885-903.

[140] Coelho, R.T., Ng, E.G. and Elbestawi, M.A., 2007. Tool wear when turning hardened AISI 4340 with coated PCBN tools using finishing cutting conditions. *International Journal of Machine Tools and Manufacture*, *47*(2), pp.263-272.

[141] Malakizadi, A., Sadik, I. and Nyborg, L., 2013, Wear Mechanism of CBN Inserts during Machining of Bimetal Aluminum-Grey Cast Iron Engine Block, Procedia CIRP, 8, pp. 188-193.

[142] Hellströrm, P. and Olander, K., Analysis and modeling of properties of Compacted Graphite Iron on a microstructural level, Master's thesis in Applied Mechanics, Chalmers University of Technology, 2012.

[143] Keski, J.R. and Cutler, I. B., 1968, Initial Sintering of Mn_xO-Al_2O_3, *Journal of the American Ceramic Society*, 51, 8, pp. 440-444.

[144] Cahoon, H. P. and Christensen, C. J., 1956, Sintering and Grain Growth of Alpha-Alumina, Journal of the American Ceramic Society, 39, 10, pp. 337-344.

[145] J. Sheikh-Ahmad, N. Urban, and H. Cheraghi, "Machining damage in edge trimming of CFRP," Mater. Manuf. Process., vol. 27, no. 7, pp. 802–808, 2012.

[146] L. S. Lasdon, A. D. Waren, A. Jain, and M. Ratner, "Design and Testing of a Generalized Reduced Gradient Code for Nonlinear Programming," ACM Trans. Math. Softw., vol. 4, no. 1, pp. 34–50, 1978.

[147] Bhatnagar, N.B.A.I.I.O.T., Ramakrishnan, N., Naik, N.K. and Komanduri, R.B.A.O.S.U., 1995. On the machining of fiber reinforced plastic (FRP) composite laminates. International Journal of Machine Tools and Manufacture, 35(5), pp.701-716.

[148] J. W. Weeton, D. M. Peters, and K. L. Thomas, Engineers' guide to composite materials. American Society for Metals, 1987.

[149] S. W. Tsai and H. T. Hahn, Introduction to composite materials. Technomic Pub, 1980.

[150] M. W. Hyer and S. R. White, "Stress Analysis of Fiber-reinforced Composite Materials," 1998.

[151] D. H. Wang, M. Ramulu, and D. Arola, "Orthogonal cutting mechanisms of graphite/epoxy composite. Part II: multi-directional laminate," Int. J. Mach. Tools Manuf., vol. 35, no. 12, pp. 1639–1648, Apr. 1995.

[152] M. Ramulu, D. Kim, and G. Choi, "Frequency analysis and characterization in orthogonal cutting of glass fiber reinforced composites," Compos. Part A Appl. Sci. Manuf., vol. 34, no. 10, pp. 949–962, 2003.

[153] J. Y. Sheikh-Ahmad and J. P. Davim, "Cutting and Machining of Polymer Composites," in Wiley Encyclopedia of Composites, Hoboken, NJ, USA: John Wiley & Sons, Inc., 2012, p. weoc061.

[154] E. Rabinowicz, Friction and wear of materials. New York: John Wiley and Sons, 1965.

[155] K. SAKUMA and M. SETO, "Tool Wear in Cutting Glass-fiber-reinforced Plastics : The Relation between Fiber Orientation and Tool Wear," Bull. JSME, vol. 26, no. 218, pp. 1420–1427, 1983.

[156] S. M. Sakuma Keizo Taniguchi Masaki, and Yokoo Yoshimichi, "Tool wear in cutting carbon fiber reinforced plastics- The effect f physical properties of tool material," Bull. JSME, vol. 28, no. 245, pp. 2781–2788, 1985.

[157] Swan S, Bin Abdullah M, Kim D, Nguyen D, Kwon P. "Tool Wear of Advanced Coated Tools in Drilling of CFRP." ASME. J. Manuf. Sci. Eng. Vol. 140 No. 11 (2018): pp.111018-111018-10. doi:10.1115/1.4040916.

[158] Nguyen D, Kwon P, Voznyuk V, Kim D. "Performance Evaluation of Superhard Coatings in Drilling of Ti-6Al-4V Alloy." International Manufacturing Science and Engineering Conference, Volume 4: Bio and Sustainable Manufacturing (2017):V004T05A028. doi:10.1115/MSEC2017-2879.

[159] Nguyen, D., Kang, D., Bieler, T., Park, K. and Kwon, P., 2017, 'Microstructural impact on flank wear during turning of various Ti-6Al-4V alloys.' Wear, 384-5, pp. 72-83. DOI:10.1016/j.wear.2017.05.002

[160] Paplham, W. P., Seferis, J. C. , BaltáCalleja, F. J. , and Zachmann, H. G. "Microhardness of Carbon Fiber Reinforced Epoxy and Thermoplastic Polyimide Composites." Polymer Composites, 16:5 (1995): pp. 424–428. DOI: 10.1002/pc.750160512.

[161] Howard, K. and Dana, M. ASM Handbook Volume 8: Mechanical Testing and Evaluation, ASM International, Materials Park, OH (2000): pp. 197–2

[162] Park, K.-H., Kwon, P., 2011, "Flank Wear of Multi-Layer Coated Tool," Wear, 270, 11-12, pp. 771-780. DOI: 10.1016/j.wear.2011.01.030

[163] Olortegui-Yume, J.A, Kwon, P.Y. "Crater wear patterns analysis on multi-layer coated carbides using the wavelet transform." Wear 268:3-4 (2010): pp. 493–504. DOI:10.1016/j.wear.2009.09.009.

[164] Sandvik Coromant catalog 2019, 2019.

[165] Park, K.H. and Kwon, P.Y., 2011. "Flank wear of multi-layer coated tool," Wear, 270(11-12), pp.771-780.

[166] Canter, N. (2009). BAM: Antiwear and friction-reducing coating. Tribology & Lubrication Technology, 65(3), 14-15.

[167] CRC Materials Science and Engineering Handbook, p.472

[168] Aihua, L., Jianxin, D., Haibing, C., Yangyang, C., & Jun, Z. (2012). Friction and wear properties of TiN, TiAlN, AlTiN and CrAlN PVD nitride coatings. International Journal of Refractory Metals and Hard Materials, 31, 82-88.

[169] https://acscoating.com/coating-specs/

[170] Liu, Z., An, Q., Xu, J., Chen, M., & Han, S. (2013). Wear performance of (nc-AlTiN)/(a-Si3N4) coating and (nc-AlCrN)/(a-Si3N4) coating in high-speed machining of titanium alloys under dry and minimum quantity lubrication (MQL) conditions. Wear, 305(1-2), 249-259.

[171] Boyer, R. R., 1996, "An overview on the use of titanium in the aerospace industry," Materials Science and Engineering, A 213(1-2), 103-114.

[172] Gogia, A. K., 2005, "High-Temperature Titanium Alloys," Defense Science Journal, 55(2), pp. 149–173.

[173] Matweb, 1996, http://www.matweb.com/

[174] Avedesian, M.M. and Baker, H. eds., 1999. ASM specialty handbook: magnesium and magnesium alloys. ASM international., pp. 95-97.

[175] Christoph, L. and Manfred, P., 2003. Titanium and titanium alloys: fundamentals and applications. WileyVCH, Köln.

[176] Ezugwu, E. O., and Wang, Z. M., 1997, "Titanium Alloys and Their Machinability—a Review," Journal of Materials Processing Technology, 68(3), pp. 262–274.

[177] Hartung, P.D., Kramer, B.M. and Von Turkovich, B.F., 1982. "Tool wear in titanium machining," CIRP Annals-Manufacturing Technology, 31(1), pp.75-80.

[178] Donachie, M.J., 2000. Titanium: a technical guide. ASM international.

[179] Klocke, F.A.E.G. and Eisenblätter, G., 1997. "Dry cutting," CIRP Annals, 46(2), pp.519-526.

[180] Kelly, J.F. and Cotterell, M.G., 2002. "Minimal lubrication machining of aluminium alloys," Journal of Materials Processing Technology, 120(1-3), pp.327-334.

[181] Sreejith, P.S. and Ngoi, B.K.A., 2000. "Dry machining: machining of the future," Journal of materials processing technology, 101(1-3), pp.287-291.

[182] Heinemann, R., Hinduja, S., Barrow, G. and Petuelli, G., 2006. "Effect of MQL on the tool life of small twist drills in deep-hole drilling," International Journal of Machine Tools and Manufacture, 46(1), pp.1-6.

[183] Yoshimura, H., Itoigawa, F., Nakamura, T. and Niwa, K., 2005. "Development of nozzle system for oil-on-water droplet metalworking fluid and its application to practical production line," JSME International Journal Series C Mechanical Systems, Machine Elements and Manufacturing, 48(4), pp.723-729.

[184] Shen, B., Malshe, A.P., Kalita, P. and Shih, A.J., 2008. "Performance of novel MoS2 nanoparticles based grinding fluids in minimum quantity lubrication grinding," Trans. NAMRI/SME, 36, pp.357-364.

[185] Park, K.H., Shantanu, J., Kwon, P., Drazl, L.T. and Do, I., 2010. "Minimum quantity lubrication (MQL) with nanographene-enhanced lubricates: Ballmilling experiment," Trans. NAMRI/SME, 38, pp.81-88.

[186] Lee, P.H., Nam, J.S., Li, C. and Lee, S.W., 2012. "An experimental study on micro-grinding process with nanofluid minimum quantity lubrication (MQL)," International Journal of Precision Engineering and Manufacturing, 13(3), pp.331-338.

[187] Lee, P.H., Lee, S.W., Lim, S.H., Lee, S.H., Ko, H.S. and Shin, S.W., 2015. "A study on thermal characteristics of micro-scale grinding process using nanofluid minimum quantity

lubrication (MQL)," International Journal of Precision Engineering and Manufacturing, 16(9), pp.1899-1909.

[188] Attanasio, A., Gelfi, M., Giardini, C. and Remino, C., 2006. "Minimal quantity lubrication in turning: Effect on tool wear," Wear, 260(3), pp.333-338.

[189] Bruni, C., Forcellese, A., Gabrielli, F. and Simoncini, M., 2006. "Effect of the lubrication-cooling technique, insert technology and machine bed material on the workpart surface finish and tool wear in finish turning of AISI 420B," International Journal of Machine Tools and Manufacture, 46(12-13), pp.1547-1554.

[190] Dhar, N.R., Ahmed, M.T. and Islam, S., 2007. "An experimental investigation on effect of minimum quantity lubrication in machining AISI 1040 steel," International Journal of Machine Tools and Manufacture, 47(5), pp.748-753.

[191] Khan, M.M.A., Mithu, M.A.H. and Dhar, N.R., 2009. "Effects of minimum quantity lubrication on turning AISI 9310 alloy steel using vegetable oil-based cutting fluid," Journal of materials processing Technology, 209(15-16), pp.5573-5583.

[192] Hwang, Y.K. and Lee, C.M., 2010. "Surface roughness and cutting force prediction in MQL and wet turning process of AISI 1045 using design of experiments," Journal of Mechanical Science and Technology, 24(8), pp.1669-1677.

[193] Leppert, T., 2011. "Effect of cooling and lubrication conditions on surface topography and turning process of C45 steel," International Journal of Machine Tools and Manufacture, 51(2), pp.120-126.

[194] Reddy, K.D. and Venkataramaiah, D.P., 2012. "Experimental investigation on responses in turning of aluminium with carbide tipped tool at different coolant conditions," International Journal of Mechanical Engineering & Technology (IJMET), 3(2), pp.189-199.

[195] Hadad, M. and Sadeghi, B., 2013. "Minimum quantity lubrication-MQL turning of AISI 4140 steel alloy," Journal of Cleaner Production, 54, pp.332-343.

[196] Lohar, D.V. and Nanavaty, C.R., 2013. "Performance evaluation of minimum quantity lubrication (MQL) Using CBN tool during hard turning of AISI 4340 and its comparison with dry and wet turning," Bonfring International Journal of Industrial Engineering and Management Science, 3(3), pp.102-106.

[197] Saini, A., Dhiman, S., Sharma, R. and Setia, S., 2014. "Experimental estimation and optimization of process parameters under minimum quantity lubrication and dry turning of AISI-4340 with different carbide inserts," Journal of mechanical science and Technology, 28(6), pp.2307-2318.

[198] Revankar, G.D., Shetty, R., Rao, S.S. and Gaitonde, V.N., 2013. "Response surface model for surface roughness during finish turning of titanium alloy under minimum quantity lubrication," International Conference on Emerging Trends in Engineering and Technology, Phuket, Thailand, December 7-8, pp.78-84.

[199] Raza, S.W., Pervaiz, S. and Deiab, I., 2014. "Tool wear patterns when turning of titanium alloy using sustainable lubrication strategies," International Journal of Precision Engineering and Manufacturing, 15(9), pp.1979-1985.

[200] Liu, Z., Xu, J., Han, S. and Chen, M., 2013. "A coupling method of response surfaces (CRSM) for cutting parameters optimization in machining titanium alloy under minimum quantity lubrication (MQL) condition," International Journal of Precision Engineering and Manufacturing, 14(5), pp.693-702.

[201] Gupta, M.K. and Sood, P.K., 2017. "Surface roughness measurements in NFMQL assisted turning of titanium alloys: An optimization approach," Friction, 5(2), pp.155-170.

[202] Gupta, M.K., Sood, P.K. and Sharma, V.S., 2016. "Optimization of machining parameters and cutting fluids during nano-fluid based minimum quantity lubrication turning of titanium alloy by using evolutionary techniques," Journal of Cleaner Production, 135, pp.1276-1288.

[203] Sartori, S., Ghiotti, A. and Bruschi, S., 2018. "Solid Lubricant-assisted Minimum Quantity Lubrication and Cooling strategies to improve Ti6Al4V machinability in finishing turning," Tribology International, 118, pp.287-294.

[204] da Silva, R.B., Machado, Á.R., Ezugwu, E.O., Bonney, J. and Sales, W.F., 2013. "Tool life and wear mechanisms in high speed machining of Ti–6Al–4V alloy with PCD tools under various coolant pressures," Journal of Materials Processing Technology, 213(8), pp.1459-1464.

[205] Lütjering, G., and Williams, J. C., 2007, Titanium, Springer-Verlag Berlin Heidelberg, New York, U.S.

[206] Sandvik Coromant catalog, 2018, https://www.sandvik.coromant.com/en-gb/products/pages/productdetails.aspx?c=SCMW%20432%20%20%20%20%20%20%20%20%20%20%20%20H13A

[207] Park, K.H., Ewald, B. and Kwon, P.Y., 2011. "Effect of nano-enhanced lubricant in minimum quantity lubrication balling milling," Journal of tribology, 133(3), p.031803.

[208] XG Science Inc., 2018, https://xgsciences.com/materials/graphene-nano-platelets/

[209] Nguyen, T., Nguyen, D., Howes, P., Kwon, P., and Park, K.-H., 2015, "Minimum Quantity Lubrication (MQL) Using Vegetable Oil with Nano-Platelet Solid Lubricant in Milling Titanium Alloy," ASME International Manufacturing Science and Engineering Conference, Charlotte, North Carolina, USA, June 8–12, p. V002T05A014.

[210] Park, K.H. and Kwon, P.Y., 2011. "Flank wear of multi-layer coated tool," Wear, 270(11-12), pp.771-780.

[211] Sun, S., Brandt, M. and Dargusch, M.S., 2009. "Characteristics of cutting forces and chip formation in machining of titanium alloys," International Journal of Machine Tools and Manufacture, 49(7-8), pp.561-568.

[212] Venkatesh, V.C. and Satchithanandam, M., 1980. "A discussion on tool life criteria and total failure causes," CIRP Annals-Manufacturing Technology, 29(1), pp.19-22.

[213] Boothroyd, G., 1988. Fundamentals of metal machining and machine tools (Vol. 28). CRC Press.

[214] Kramer, B. M., and Suh, N. P., 1980, "Tool wear by solution: a quantitative understanding." Journal of Engineering for Industry, 102(4), pp. 303-309.

[215] Nguyen, T., Park, K.-H., Wang, X., Olortegui-Yume, J., Wong, T., Schrock, D., Kim, W., Kwon, P., and Kramer, B., 2015, "The Genesis of Tool Wear in Machining," ASME 2015 International Mechanical Engineering Congress and Exposition, Volume 15: Advances in Multidisciplinary Engineering, Houston, Texas, USA, November 13–19, p. V015T19A01.